Electrokinetics and Vibrofluidics:
Driving Particle Motion with Unimodal and Multimodal Forces

By

TIMOTHY C. HUI
DISSERTATION

Submitted in partial satisfaction of the requirements for the degree of

DOCTOR OF PHILOSOPHY

in

CHEMICAL ENGINEERING

in the

OFFICE OF GRADUATE STUDIES

of the

UNIVERSITY OF CALIFORNIA

DAVIS

Approved:

_____
William D. Ristenpart, Chair

_____
Gregory H. Miller

_____
Jiandi Wan

Committee in Charge

2023

Contents

Abstract

Although alternating current (AC) unimodal electrokinetics are studied extensively in a variety of microfluidic and fabrication processes, linearized electrokinetic models fail to comprehensively capture the complex dependency on the electrolyte identity. Recent nonlinear numerical studies indicate the existence of nonzero time-average electric fields, called asymmetric rectified electric fields (AREFs), which arise from the ion mobility mismatch of the electrolyte. Further, the application of a multimodal field has been theorized to break the spatial symmetry of AREF, yielding net particle drift in the bulk fluid. While some experimental evidence implicates AREF-driven electrokinetics, the connection between AREFs and many experimentally observed phenomena remain untested. This dissertation presents a broad assessment of AREFs in particle aggregation and particle net drift in microfluidic channels under unimodal and multimodal polarization. Estimates of an AREF-induced steady flow coupled with previous AC electrokinetic theory provide a scaling explanation on the electrolyte-dependent aggregation or separation behavior near electrode surfaces. Further, observed particle distributions using a microchannel configuration agree with numerical AREF predictions predicated on electroosmotic flows arising on the particle and channel wall surfaces.

These results served as a motivation to investigate temporal symmetry breaking in vibrating systems with solid-solid friction to enable “vibrofluidic” manipulation of granular materials. Both experimental and theoretical results demonstrate that multimodal vibrations induce transport of dry granular media in a desired direction, while mixing and separation operations are achieved using various channel geometries or waveform properties. Both the electrokinetic and vibrofluidic results suggest that multimodal driving forces may pertain to a broad range of other useful applications.

Acknowledgements

Throughout my journey at UC Davis, I have had the unique pleasure to meet and work with many highly motivated and brilliant people. I extend my deepest gratitude to my academic advisor Professor William Ristenpart, for his wisdom and guidance throughout the years. I would also like to thank Professor Gregory Miller, who has been a candid source of knowledge, as well as Professor Jiandi Wan and his students for advice on the various microfluidic experiments that I have conducted.

I also thank the many graduate companions I had met along the way. Thank you Aref, whose numerical work formed the foundation for my colloidal journey, as well as Scott, Sima, and Eric for guiding me in the early years of my PhD. I was also fortunate to experience this journey with Esohe (senior member, of course), for correspondence on various struggles and victories along the path, as well as other members of our cohort including Nitin, Benji, Gustavo, Shiaki, and Nate. I am also grateful for the complex fluid team Fizza, Thomas, and Emirhan for keeping the office coffee and snack stash full. A special thanks to my co-author Xiaolin for great strides in our granular studies, as well as being an inquisitive mentee.

Beyond Davis, I would also like to thank my local tourists crew in San Francisco for our many adventures, and Illythelongcat for waking me up in the morning with flawless precision. Lastly, but most importantly, I would like to thank my family back home in New Jersey, to their constant support and love without which this would not be possible.

List of Figures and Tables

Chapter 1: Introduction

1.1 Unimodal electrokinetics

Manipulation of colloidal suspensions using electric fields provide high throughput and convenience as advantages for an active transport mechanism[1,2]. In contrast to the direct current (DC) counterpart, alternating current (AC) electric fields introduce rectified transport by frequency dependent parameters such as dielectric and conductivity properties[3]. The literature of AC fields can be divided into various regimes, such as high frequency (> 1 MHz) fields often employed in dielectrophoresis[4–6] or highly polarizable materials in induced charge electrokinetics (ICEK)[7,8]. AC fields are also used in conjunction with other active mechanisms, such as coupled AC-DC fields[9], thermal gradients[10], and concentration gradients[11,12]. These designs are typically engineered on the sub-millimeter length scale, towards lab-on-a-chip applications in biological cell manipulation, fabrication, and general microfluidic studies[1,4,6].

Despite decades of work implementing AC fields, several colloidal particle behaviors are still not well understood at the low frequency limit (< 1 MHz)[13]. In this limit, linearized models of the electric field, i.e. $E \sim E_0 e^{i\omega t}$ for an angular frequency ω at the characteristic electric field strength E_0, fail to fully describe experimentally observed particle levitation and aggregation phenomena near the vicinity of a polarized electrode.

Numerical studies conducted by Hashemi et al. evaluate the electric field distribution between two planar electrodes, allowing nonequal ion diffusivity. They found that, for nonequal ion mobilities, the time average electric field can be nonzero[14–16]. These time averaged multimodal contributions, called asymmetric rectified electric fields (AREFs), yield steady fields that have not been accounted for in many previous works. Recent work by Bukosky et al.

highlights the significance of AREF towards experimentally observed particle levitation from a polarized electrode[17], where the levitation height scales similarly to the AREF length scale $\mathcal{L}_D \sim \sqrt{\frac{\sqrt{D_+ D_-}}{f}}$. Rath et al. also recognized an electrochemically induced AREF using a para-benzoquinone (BQ) system that influenced particle aggregation[18]. Nonetheless, to date there is a lack of experimental data testing several hypotheses set forth regarding AREF.

1.2 Multimodal kinetics

Unimodal and DC electrokinetics, as previously covered, are commonly studied in various academic topics on the micro to millimeter scale. Less studied, however, are multimodal fields[19]. An important distinction here is that AREF is a multimodal field induced by an imposed unimodal polarization; here, the focus is on an imposed multimodal electric field of the form

$$E(t) = \mathrm{A}\sin(\omega \mathrm{t}) + B\sin(\gamma\omega t + \phi)\,. \tag{1.1}$$

Equation 1.1 describes a dual-mode waveform, composed of two sinusoidal waves of angular frequencies ω and $\gamma\omega$, at magnitudes A and B. Implications of a multimodal polarization are not well understood for colloidal systems; however, analogues are available to provide insight. Rectified motion has already been established in various works on optics and atomic-scale studies. For millimeter scale studies, Hashemi et al. showed that a single object placed inside a vibrating test tube could achieve net drift depending on the waveform[19]. Reznik and Canny also showed that the drift of a single coin scales linearly with the applied amplitude[20,21]. On the colloidal particle scale, Hashemi et al. also demonstrated that 2 μm diameter particles suspended in dilute NaOH can also achieve net drift; they attributed this to a symmetry breaking time-average electric field that forms upon dual-mode polarization. These findings indicate new methods to manipulate small-scale objects using multimodal kinetics.

1.3 Goals and outline of this dissertation

The overarching goal of this dissertation is to study nonlinear dynamics due to unimodal and multimodal forces. The primary goal of this dissertation is experimental work via suspended colloidal particles between parallel electrodes, which provide direct comparisons to theories related to AREF. A secondary goal focuses on an analogue system using friction-based forces powered by acoustic means. Details are as follows:

Chapter 2 studies colloidal particle aggregation or separation effects near a polarized electrode using confocal microscopy. Comparisons of classical electrohydrodynamic (EHD) forces to AREF-induced forces yield predictions that indicate an electrolyte dependency stemming from AREF that accord with measured aggregation rates.

Theoretical predictions for AREF indicate long-range steady fields in the bulk. Chapter 3 details bulk colloidal particle behavior under unimodal oscillatory polarization between parallel electrodes using a novel microchannel design. An AREF-induced electroosmotic background flow yield streamlines that influence bulk particle motion, depending on the zeta potentials of the particle and the wall.

Chapter 4 details colloidal particle behavior under multimodal polarizations. Under these conditions, particles can exhibit symmetry-breaking drift, the direction of which depends on whether the electrode is polarized or grounded. Other waveform parameters are considered as well.

Interpretation of a multimodal applied electric field can be challenging to interpret for electrokinetic systems. Chapter 5 introduces an analogue system to study multimodal kinetics by

using friction-based vibrations. Dry granular powders were successfully pumped, mixed, or separated, as a function of waveform parameters and channel geometries.

Chapter 6 provides future direction comments, including future theoretical work on the model presented in Chapter 2, and future fabrication work that will be useful towards interpreting the studies detailed in Chapter 3-5.

1.4 References

1. Liljeström, V., Chen, C., Dommersnes, P., Fossum, J. O. & Gröschel, A. H. Active structuring of colloids through field-driven self-assembly. *Curr. Opin. Colloid Interface Sci.* **40**, 25–41 (2019).
2. Edwards, T. D. & Bevan, M. A. Controlling colloidal particles with electric fields. *Langmuir* **30**, 10793–10803 (2014).
3. Russel, W. B., Saville, D. A. & Schowalter, W. R. *Colloidal Dispersions*. (Cambridge University Press, 1989).
4. Çetin, B. & Li, D. Dielectrophoresis in microfluidics technology. *Electrophoresis* **32**, 2410–2427 (2011).
5. Gascoyne, P. R. C. & Vykoukal, J. Particle separation by dielectrophoresis. *Electrophoresis* **23**, 1973–1983 (2002).
6. Ramirez-Murillo, C. J., de los Santos-Ramirez, J. M. & Perez-Gonzalez, V. H. Toward low-voltage dielectrophoresis-based microfluidic systems: a review. *Electrophoresis* **42**, 565–587 (2021).
7. Bazant, M. Z. & Squires, T. M. Induced-charge electrokinetic phenomena. *Curr. Opin. Colloid Interface Sci.* **15**, 203–213 (2010).
8. Feng, H., Chang, H., Zhong, X. & Wong, T. N. Recent advancement in induced-charge electrokinetic phenomena and their micro- and nano-fluidic applications. *Adv. Colloid Interface Sci.* **280**, 102159 (2020).
9. Zhao, C. & Yang, C. Continuous-flow trapping and localized enrichment of micro- and nano-particles using induced-charge electrokinetics. *Soft Matter* **14**, 1056–1066 (2018).

10. Zhao, C., Ge, Z., Song, Y. & Yang, C. Electrokinetically driven continuous-flow enrichment of colloidal particles by Joule heating induced temperature gradient focusing in a convergent-divergent microfluidic structure. *Sci. Rep.* **7**, 10803 (2017).
11. Shin, S. *et al.* Size-dependent control of colloid transport via solute gradients in dead-end channels. *Proc. Natl. Acad. Sci.* **113**, 257–261 (2016).
12. Keh, H. J. Diffusiophoresis of charged particles and diffusioosmosis of electrolyte solutions. *Curr. Opin. Colloid Interface Sci.* **24**, 13–22 (2016).
13. Prieve, D. C., Sides, P. J. & Wirth, C. L. 2-D assembly of colloidal particles on a planar electrode. *Curr. Opin. Colloid Interface Sci.* **15**, 160–174 (2010).
14. Hashemi, A., Bukosky, S. C., Rader, S. P., Ristenpart, W. D. & Miller, G. H. Oscillating electric fields in liquids create a long-range steady field. *Phys. Rev. Lett.* **121**, 185504 (2018).
15. Hashemi, A., Miller, G. H. & Ristenpart, W. D. Asymmetric rectified electric fields between parallel electrodes: numerical and scaling analyses. *Phys. Rev. E* **99**, 062603 (2019).
16. Hashemi, A., Miller, G. H., Bishop, K. J. M. & Ristenpart, W. D. A perturbation solution to the full Poisson–Nernst–Planck equations yields an asymmetric rectified electric field. *Soft Matter* **16**, 7052–7062 (2020).
17. Bukosky, S. C. *et al.* Extreme levitation of colloidal particles in response to oscillatory electric fields. *Langmuir* **35**, 6971–6980 (2019).
18. Rath, M., Weaver, J., Wang, M. & Woehl, T. pH-Mediated aggregation-to-separation transition for colloids near electrodes in oscillatory electric fields. *Langmuir* **37**, 9346–9355 (2021).

19. Hashemi, A., Tahernia, M., Hui, T. C., Ristenpart, W. D. & Miller, G. H. Net motion induced by nonantiperiodic vibratory or electrophoretic excitations with zero time average. *Phys. Rev. E* **105**, 065001 (2022).
20. Reznik, D. & Canny, J. The Coulomb pump: a novel parts feeding method using a horizontally-vibrating surface. in *Proceedings. 1998 IEEE International Conference on Robotics and Automation (Cat. No.98CH36146)* vol. 1 869–874 vol.1 (1998).
21. Reznik, D. & Canny, J. A flat rigid plate is a universal planar manipulator. in *Proceedings. 1998 IEEE International Conference on Robotics and Automation (Cat. No.98CH36146)* vol. 2 1471–1477 vol.2 (1998).

Chapter 2: Influence of asymmetric rectified electric fields on colloidal particle behavior near electrodes

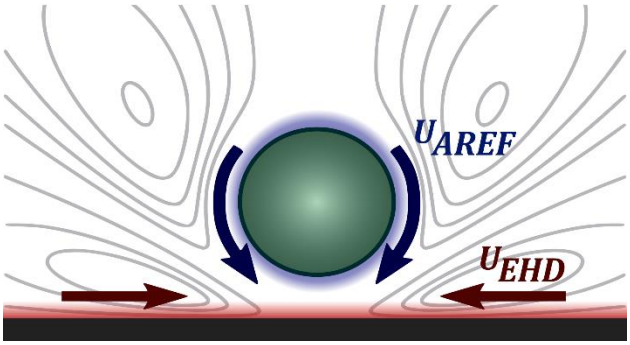

Micron-scale colloidal particles suspended in electrolyte solutions near an electrode are observed to either aggregate, separate laterally, or levitate to discrete heights in response to an applied AC electric field. Although various models have been proposed to elucidate this behavior, to date none have explained the observed dependence on the type of electrolyte present. Recent theoretical and experimental work has established the previously unsuspected existence of a long-range steady field, denoted as an asymmetric rectified electric field (AREF), that forms when an electrolyte with unequal ionic mobilities undergoes oscillatory polarization. Here, we assess the impact of AREFs on the behavior of colloids near the electrode. The rates of colloidal aggregation or separation were measured for particles in seven different electrolytes at different applied frequencies and voltages. We present scaling arguments indicating that the observations are consistent with a competition between two different electrically induced flows: an AREF-induced electroosmotic flow generated on the particle surface that typically favors separation, and an electrohydrodynamic (EHD) flow generated along the electrode that favors aggregation. The results suggest that the long-observed electrolyte dependence stems directly from AREFs induced by the ionic mobility mismatch.

2.1 Introduction

Colloidal particles near a planar electrode are known to aggregate or separate in response to an applied DC or AC field[1–5]. Solomentsev et al. analyzed the DC field case by considering the electroosmotic slip condition on an isolated particle close to the electrode, demonstrating that the resulting equilibrium-charge electroosmosis (ECEO) creates a toroidal flow pattern around the particle that entrains nearby particles and causes them to aggregate[6]. Although there is general agreement on the ECEO mechanism for DC field induced aggregation, the counterpart AC field case has been significantly more challenging to resolve. Kim et al. first reported an electrolyte dependence on the interparticle spacing, noting that particles suspended in NaOH were found to separate in response to the applied field, whereas particles suspended in NaCl and $NaHCO_3$ aggregated[7,8]. Vertical particle height experiments using total internal reflection microscopy (TIRM) by Fagan et al. also revealed an electrolyte dependency at odds with expectations from electrokinetic theories at the time[9]. The observations led to the notion of "aggregating electrolytes" and "separating electrolytes," but the underlying mechanism for why certain electrolytes fell into either group remained obscure.

Two major theoretical advances, as reviewed in detail by Prieve et al., dominated the current theoretical understanding of particle behavior in AC fields[10]. The first stems from foundational work by Trau et al. regarding an electrohydrodynamic (EHD) fluid flow, also called the induced charge electroosmosis (ICEO)[2,3]. The presence of the polarizable particle disrupts the otherwise spatially uniform electric field near the electrode, inducing a dipolar electric field to develop underneath the particle with a tangential component parallel to the electrode. These tangential components interact with the polarization layer induced near the electrode surface by the oscillatory applied potential, generating an entraining fluid flow that causes particles to aggregate.

A scaling analysis by Ristenpart et al. for the EHD model based on point dipoles yielded a squared dependence on the electric field and an inverse dependence on frequency, predictions that were corroborated experimentally for KCl solutions[11,12]. Several subsequent works utilize this model to estimate EHD flow behavior across various applied frequencies, electrolytes, and electrolyte concentrations[13–17].

A key weakness of the EHD model, however, is that it failed to explain the observed electrolyte dependence. An alternative set of theories set forth by Prieve, Sides, and co-workers initially focused on possible types of symmetry breaking in the ECEO[7–9,18–20]. Fagan et al. consider various models accounting for colloidal forces, wall-enhanced drag, and Faradaic-coupled electroosmosis (FCEO) at low frequencies[21]. Importantly, they observed a distinct phase angle between the particle height oscillation and the electric current, which appear correlated to aggregation or separation behavior. Hoggard et al. performed TIRM experiments for various electrolytes-electrode combinations detailing this phase angle behavior[22,23]. Much of the phase angle theory culminated to the numerical model proposed by Wirth et al., which correlated particle aggregation or separation propensity by phase angle predictions[24,25].

While both lines of work provided key mechanistic insights, none of the theories yielded predictive models that allowed one to assess whether a given electrolyte would cause aggregation or separation. An extensive review of 26 different electrolyte-particle combinations by Woehl et al. reported a particle zeta potential correlation at odds with predictions provided by the point-dipole EHD model[14]. Several predictions from Wirth et al. also do not accord with previous experimental observations; subsequent experimental reports revealed a phase transition from separation to aggregation at sufficiently low frequencies for hydroxides, counter to the theoretical predictions from the model[15].

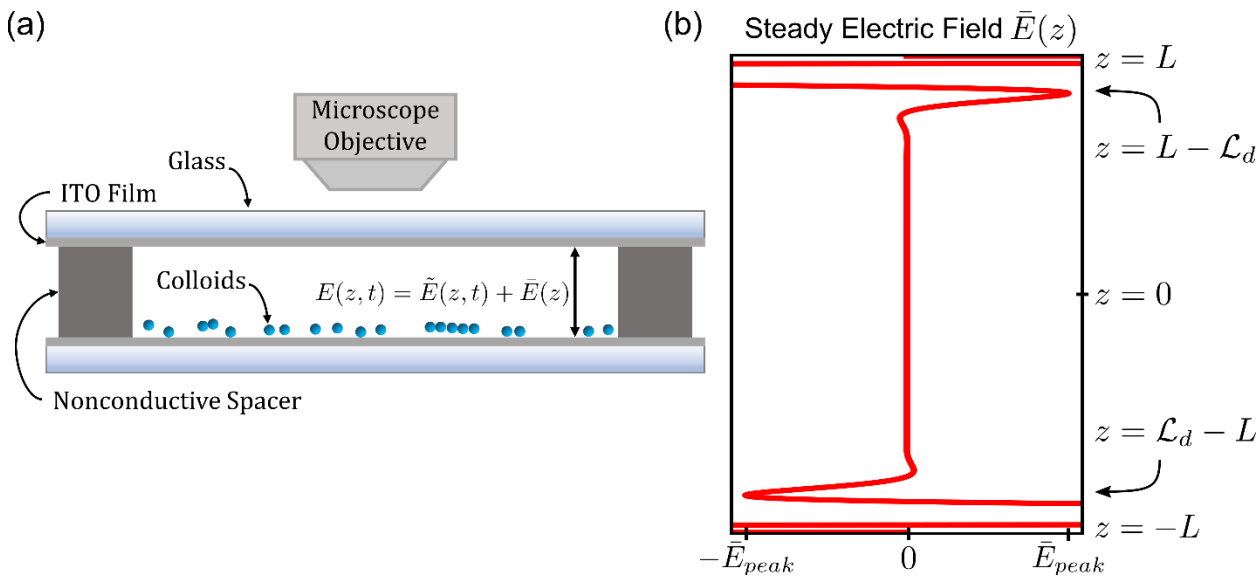

Figure 2.1. *(a) Schematic of the experimental setup for a colloidal suspension between parallel electrodes, with an oscillatory electric field $E(z,t)$ applied vertically across the suspension. (b) Representative calculation of the steady AREF component $\bar{E}(z)$ between two electrodes separated by a distance 2L. Here $\bar{E}_{peak}$ denotes the maximum field strength magnitude assessed at a distance from the electrode given by the AREF length scale $\mathcal{L}_d = \sqrt{\frac{\sqrt{D_+ D_-}}{f}}$.*

Further complicating matters, recent work has revealed a third type of behavior: colloids that undergo separation can also levitate very far up off the electrode. Woehl et al. reported particle heights at low applied frequencies ranging several microns over the electrode. [14] Subsequent work showed that sufficiently low frequencies (< 25 Hz) could cause 1-micron particles in NaOH to levitate up to 30 microns away from the electrode – a length scale inexplicable from EHD or ECEO induced forces alone[15,17,26,27]. Thus, a generalized theory that accurately accounts for the electrolyte dependent behavior of this system has remained elusive.

Notably, all of the above theoretical work used simplified versions of the standard electrokinetic model, i.e., the coupled Poisson Nernst Planck equations (PNP), by assuming that the ion diffusivities are equal[28]. Recent work by Hashemi et al. proposed that accounting for the ion mobility mismatch could introduce further nonlinear electric field effects[29]. Their asymptotic

analyses and numerical calculations revealed that application of an oscillatory field to a liquid containing ions with a mobility mismatch will induce a steady electric field within the liquid. These steady fields, denoted as asymmetric rectified electric fields (AREFs), have a complicated spatial dependence and vary inversely with the square root of the applied frequency (cf. Fig. 2.1) [29,30]. Hashemi et al. hypothesized that an AREF-induced electroosmosis can produce flow either against or in concert with EHD flows, and subsequent experimental work illustrated the relevance of AREF on the observed levitation. Bukosky et al. interpreted the observed colloidal particle levitation to a force balance between AREF-induced electrophoresis and gravity[27]. Using particles of various sizes in KOH and NaOH solutions, they found that the levitation height varied as the inverse square root of the applied frequency, matching the characteristic length scale for AREF. More recent work by Rath et al. explored the implications of AREF on a pH-mediated aggregation-to-separation transition of colloids using a para-benzoquinone (BQ) solution[31]. By superimposing a steady field to the oscillatory field, the local pH near the electrode can be controlled as a function of the steady current when BQ reduces to hydroquinone. They showed that the change from aggregation to separation behavior can be attributed to an AREF-induced electroosmosis on the particle surface as a function of the steady current, using numerical fitting predictions of the peak AREF magnitude. Importantly, the authors note that the large mobility mismatch between the dissolved potassium ions and the controlled concentration of hydroxyl ions from the electroreduction process drives the AREF.

Although these studies corroborated the importance of AREFs on colloids near the electrodes, to date it remains unclear whether the long-standing observations of electrolyte dependent aggregation or separation are explicable in terms of AREFs. The main goal of this paper is to quantitatively compare the predicted EHD and AREF-induced fluid flow contributions around an

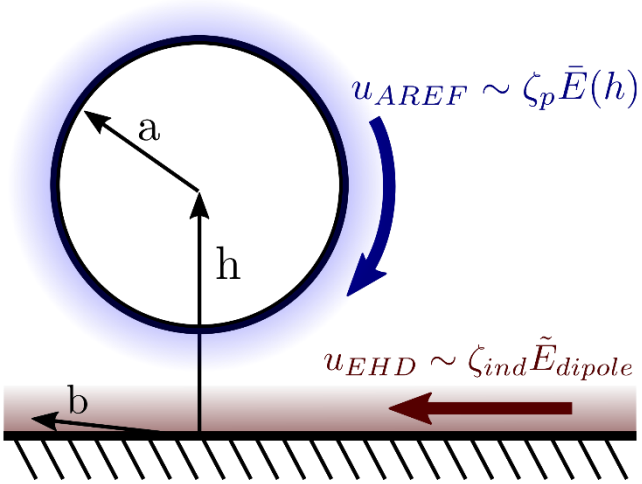

Figure 2.2. *Cartoon schematic of the u_{EHD} and u_{AREF} electrokinetic flows along the electrode and particle surface respectively based on different electrostatic potentials and electric field driving forces. The particle center is at height h with a radius of a. The vector b denotes a location near the electrode surface (cf. Equation 2.12).*

individual particle in different electrolytes and to assess whether the predicted flows are consistent with the experimentally observed aggregation behavior. We first introduce scaling arguments to estimate the relative magnitudes of the EHD and AREF induced drag forces on the particle using leading order solutions to the electric field derived by Hashemi et al. in the limit of low potentials and by Balu and Khair in the limit of thin double layers[32,33]. We then present experimental data for seven different univalent binary electrolytes of varying ion diffusivities, each tested at three different applied potentials and three different applied frequencies, yielding observations over a wide range of parametric space. The results presented here provide the first systematic test of the impact of AREFs on colloidal aggregation or separation near electrodes.

2.2 Theory

The overarching hypothesis is that particle aggregation or separation is governed by the relative magnitudes of an electroosmotic slip generated on the particle surface or an electrohydrodynamic slip generated on the electrode surface (cf. Fig. 2.2). Accordingly, the main goal of this section is to derive scaling predictions for the relative magnitudes of these hydrodynamic forces.

For the case of EHD flow generated on the electrode surface, the induced oscillatory dipole of the particle interacts with the charge polarization layer above the electrode, creating lateral flows along the surface of the electrodes (denoted by the red arrow in Fig. 2.2). Note that these EHD flows occur regardless if the ions have a mobility mismatch; prior research assumed that the ionic mobilities were equal. The direction of EHD flow along the electrode surface depends on the sign of the particle dipole coefficient (which itself depends on the particle zeta potential), but since most colloids in aqueous systems have negative dipole coefficients, we focus here on that situation. Thus, the EHD flow is typically directed radially inward toward the particle and exerts an attractive entraining flow between adjacent particles.

For the case of electroosmosis (EOS) generated on the particle surface, in contrast, the AREF generated by the ionic mobility mismatch explicitly provides the driving force. Accordingly, the properties of the AREF and the particle zeta potential will dictate whether the AREF flow assists or hinders EHD flow. For the experiments performed in this paper, particle surfaces were negatively charged.

2.2.1 1-D electric field distribution

Consider an applied potential $\pm\phi_0 \sin(\omega t)$ at the electrode positions $z = \mp L$, where z is the spatial coordinate between the two electrodes, $2L$ is the electrode spacing, t is time, and $\omega = 2\pi f$ for frequency f (cf. Fig. 2.1). To facilitate scaling derivations, expressions for the 1-D electric

field assume the absence of the particles and apply in the limit of small potentials such that $\phi_0 \ll \frac{k_B T}{e}$, where k_B is the Boltzmann constant, T is the absolute temperature, and e is the elementary charge. Hashemi et al. showed that the 1-D electric field $E(z,t)$ solution in this limit takes the form

$$E(z,t) \sim \tilde{E}(z)e^{i\omega t} + \bar{E}(z). \tag{2.1}$$

The first term $\tilde{E}(z)$ represents the magnitude of the linear oscillatory solution for the electric field, while the second term $\bar{E}(z)$ is a time-averaged solution that describes the steady AREF.

For cation and anion diffusivities D_+ and D_- respectively, the following terms are defined as

$$\beta = \frac{D_+ - D_-}{D_+ + D_-}, \qquad D = \frac{2D_+D_-}{D_+ + D_-}, \qquad \Omega^2 = \frac{\omega \mathrm{i}}{\kappa^2 D}, \qquad \gamma^2 = 1 + \Omega^2.$$

The Debye parameter κ for a univalent binary electrolyte solution is also defined here as

$$\kappa = \sqrt{\frac{2e^2 n_0}{\varepsilon \varepsilon_0 k_B T}}.$$

Using these terms, the electric field magnitude $\tilde{E}(z)$ can be simplified from Hashemi et al.[32] using the spatial derivative of their Equation 34 and restricting attention to systems with thin double layers ($\kappa L \gg 1$) and sufficiently low frequencies such that the condition $\left(\frac{\beta\omega}{\kappa^2 D}\right)^2 \ll 1$ is satisfied. These assumptions yield the magnitude of the oscillatory component,

$$\tilde{E}(z) = \frac{\phi_0}{L}\left[1 + A\left(\Omega\kappa L e^{-\Omega\kappa(z+L)} - 1\right) + B\left(\gamma\kappa L e^{-\gamma\kappa(z+L)} - 1\right)\right], \tag{2.2}$$

where

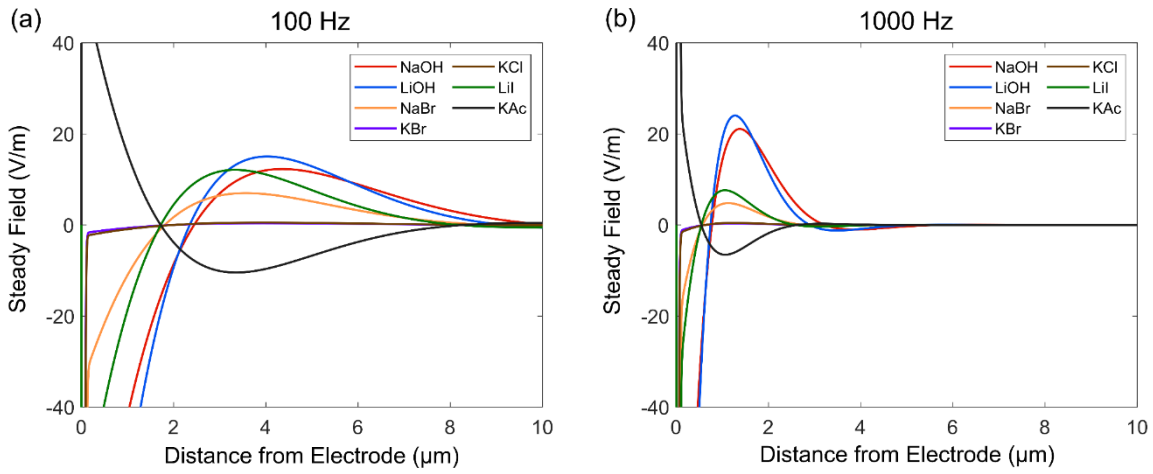

Figure 2.3. *Theoretical steady electric fields for various electrolytes calculated using the AREF solution Equation 2.7 for an applied 4 V_{pp} electric potential at (a) 100 Hz and (b) 1000 Hz.*

$$A = \frac{\beta^2 \Omega}{1 + \Omega^2 \kappa L (1 - \beta^2)}, \qquad B = \frac{2\beta\Omega^2 + 1}{1 + \Omega^2 \kappa L (1 - \beta^2)}. \tag{2.3, 2.4}$$

Equation 2.2 pertains to systems with monovalent ions and when and focuses explicitly on the lower half domain between $z = [-L, 0]$. These conditions are typically satisfied experimentally. To leading order, the electric field at the electrode surface $z = -L$ is the real part of

$$\tilde{E}_L = \frac{\phi_0}{L}\left[\frac{\kappa L}{1 + \Omega^2 \kappa L (1 - \beta^2)}\right] e^{i\omega t}. \tag{2.5}$$

Outside the double layer, the electric field rapidly decays to the bulk field strength $\frac{\phi_0}{L}$. Thus to leading order the oscillatory field strength far away from the electrode is the real part of

$$\tilde{E}_\infty = \frac{\phi_0}{L}\left[\frac{\Omega^2 \kappa L (1 - \beta^2)}{1 + \Omega^2 \kappa L (1 - \beta^2)}\right] e^{i\omega t}. \tag{2.6}$$

Turning attention to the steady AREF field $\bar{E}(z)$, we use the derivation provided by Balu and Khair[33] in the thin double layer and small potential limit. Expanding upon the complex conjugate terms (cf. their Equation 62) and again noting that $\kappa L \gg 1$ yields

$$\bar{E} = \frac{\kappa \Omega'^3 \phi_0^2}{\phi_T} \left[\frac{(\beta^3 - \beta)\left(\sin\left(\Omega' \kappa (z+L)\right) - \cos\left(\Omega' \kappa (z+L)\right)\right)}{e^{\Omega' \kappa (z+L)}} + \frac{\beta^3}{e^{2\Omega' \kappa (z+L)}} \right], \qquad (2.7)$$

where $\phi_T = \frac{k_B T}{e}$ is the thermal voltage and $\Omega' = \sqrt{\omega / 2\kappa^2 D}$.

Representative AREF distributions are shown in Fig. 2.3 for experimentally relevant conditions considered here. For electrolytes with $\beta \approx 0$, such as KCl or KBr, the magnitude of AREF far from the electrode is small in comparison to AREF due to electrolytes such as NaOH or LiI. Note that the sign of the AREF changes from negative to positive over a length scale of microns, commensurate with a typical particle size. Uniquely for potassium acetate (KAc), $\beta > 0$, resulting in an AREF with sign opposite to that of the other electrolytes.

As noted by Balu and Khair, Equation 2.7 is valid for positions well outside the double layer. Importantly, it predicts the same ϕ_0^2 scaling observed by Hashemi et al. in their low applied potential perturbation. In this form, the AREF scales with odd powers of β and $\omega^{\frac{3}{2}}$, which follows numerical scaling predictions at low potentials[29]. Note the significant difference in how the magnitudes of the oscillatory component and the steady AREF vary with position: the oscillatory component decays exponentially with position and characteristic length scale $(\Omega\kappa)^{-1}$, while to leading order the steady AREF component is a strongly damped oscillation that both oscillates and decays with characteristic length scale $(\Omega'\kappa)^{-1}$. The key implication is that the balance of forces depends sensitively on the applied frequency as well as the specific particle position with respect to the electrode.

2.2.2 Electrokinetic force scalings

Next, we examine how the electric fields described above cause fluid motion near a colloid, starting with the EHD flow due to the oscillatory dipole field. For the purpose of scaling analyses, we use the Helmholtz-Smoluchowski equation[28] for the electrically induced slip velocity u as

$$u = -\frac{\varepsilon\varepsilon_0\zeta_e E}{\mu}, \tag{2.8}$$

where ε is the fluid dielectric constant, ε_0 is the permittivity of free space, ζ is the electrostatic potential at the interface (induced by the applied field), and E is the electric field tangent to the surface. By neglecting the 2nd order correction in Faxen's law, the consequent hydrodynamic drag force on a nearby particle of radius a reduces to Stoke's law as

$$F_{drag} = 6\pi\mu a u. \tag{2.9}$$

The nature of the electrostatic potential and driving field differs significantly between the EHD and AREF-induced flows. Here we implement the scaling approximation proposed by Ristenpart et al.[11] for EHD flow. To estimate the surface charge q in the Debye layer, a balance between viscous and electric stresses on the double layer length scale yields

$$\mu\frac{u_{EHD}}{\kappa^{-1}} = -\frac{\varepsilon\varepsilon_0\zeta_e\tilde{E}_{dipole}}{\kappa^{-1}} = q\tilde{E}_{dipole}. \tag{2.10}$$

From Equation 2.10, the polarization charge q can be obtained using Gauss' law such that

$$q = -\varepsilon\varepsilon_0\tilde{E}_L = -\frac{\varepsilon\varepsilon_0\phi_0}{L}\left[\frac{\kappa L}{1+\Omega^2\kappa L(1-\beta^2)}\right]e^{i\omega t}. \tag{2.11}$$

In treating the particle as a point dipole, the magnitude of the dipole field $\tilde{E}_{dipole}$ tangent to the electrode can be approximated as the real part of

$$\tilde{E}_{dipole} = -\frac{\phi_0}{L}\frac{3C_0 bha^3}{(h^2+b^2)^{\frac{5}{2}}}\left[\frac{\Omega^2\kappa L(1-\beta^2)}{1+\Omega^2\kappa L(1-\beta^2)}\right]e^{i\omega t}, \tag{2.12}$$

where b is the distance between the particle center and the point where the electric field is evaluated (cf. Fig. 2.2). For the scaling analysis, we assume $b = a$. An asymptotic analytic solution for low frequencies from Hinch et al.[34] provides estimates for the complex dipole coefficient C_0. Note that the presence of AREF indicates a multimodal dipole coefficient based upon each mode; however, for scaling purposes we limit ourselves to the primary mode from the applied frequency on the boundaries. Taking the product of Equations 2.11 and 2.12, and then taking the real components and retaining only rectified terms, the characteristic steady EHD flow velocity is predicted to scale as

$$u_{EHD} \sim \frac{3\varepsilon\varepsilon_0 ha^4\phi_0^2}{2\mu L(h^2+a^2)^{\frac{5}{2}}}\left[\frac{C_0' + C_0''\left(\frac{\omega L}{\kappa D}\right)^2(1-\beta^2)^2}{1+\left(\frac{\omega L}{\kappa D}\right)^2(1-\beta^2)^2}\right], \tag{2.13}$$

where C_0' and C_0'' are the real and imaginary components of the dipole coefficient, respectively. As discussed by Woehl et al.[14] (cf. their Fig. S2), C_0' is roughly $O(10^{-1})$ and C_0'' is $O(10^{-5})$. For experimental frequencies of 100 to 1000 Hz and in the thin double layer limit, C_0'' is at least two orders of magnitude smaller than C_0'. Thus, approximating $C_0 \sim -\frac{1}{2}$, the EHD force is

$$F_{EHD} \sim \frac{-9\pi\varepsilon\varepsilon_0 ha^5\phi_0^2}{2L(h^2+a^2)^{\frac{5}{2}}}\left[\frac{1}{1+\left(\frac{\omega L}{\kappa D}\right)^2(1-\beta^2)^2}\right]. \tag{2.14}$$

The resulting EHD force generally scales with the square of the applied voltage and the inverse squared frequency. Note that this scaling result differs from the inverse frequency dependence originally proposed by Ristenpart et al.[11,12], which focused on larger frequencies in the kilohertz

range. Note also that the EHD flow is only weakly affected by the mobility mismatch via the $(1-\beta^2)^2$ term, yielding a small effect for β values typically encountered experimentally. We emphasize that F_{EHD} is always negative (at least in the limits described above), indicating a radially inward flow and corresponding attractive force on nearby particles. It is therefore not possible to use EHD flow by itself to account for the experimentally observed particle separation in some systems.

Now we turn our attention to the electroosmotic flow u_{AREF} induced on the particle surface via the steady AREF. Substitution of Equation 2.7 into Equations 2.8 and 2.9 yields the AREF hydrodynamic force scale,

$$F_{AREF} \sim 6\pi\varepsilon\varepsilon_0 a\zeta_p \bar{E}_h. \tag{2.15}$$

Here $\bar{E}_h$ is the steady AREF evaluated at the location of the particle center (Equation 2.7 with $z = h - L$), and ζ_p is the particle zeta potential. Note that $\bar{E}_h$, and the corresponding F_{AREF}, can be either positive or negative depending on the sign of β (i.e., on whether the positive or negative ions have a larger mobility). Here a negative (positive) F_{AREF} indicates an attractive (repulsive) force, such that the induced EOS flow attracts (repels) nearby particles.

Our overarching objective is to compare the magnitudes of the flows engendered by the steady AREF and the dipolar EHD flow to determine whether particles will aggregate or separate, but this comparison is complicated in certain limits where the applied fields are weak and thermal forces dominate the observed motion of the particles. In particular, for vanishingly small mobility mismatches as β approaches zero, the steady AREF component vanishes and the EHD flow would be predicted to dominate, leading to aggregation. For sufficiently small applied voltages, however, the particles are observed to diffuse apart by Brownian motion. Accordingly, we define a

comparison that also includes the confounding influence of thermal energy. The Brownian force scale is assumed to scale simply as

$$F_B \sim \frac{k_B T}{a}, \tag{2.16}$$

neglecting the influence of the nearby electrode or other particles. We thus have three significant forces acting on the particles: a Brownian force that always acts to scatter the particle, an EHD flow that always exerts an attractive force on the particles, and an electroosmotic AREF force that can exert either an attractive or a repulsive force depending on the mobility mismatch, the frequency, and the particle position. To capture all of these possibilities, we define a scaling parameter χ as the ratio between repulsive forces to attractive forces, generally written as

$$\chi = \frac{F_{repulsive}}{F_{attractive}}.$$

If $\chi > 1$, the particles are predicted to actively separate; if $\chi < 1$, the particles are predicated to aggregate. For particles near the electrode, the sign of AREF can be predicted simply by the sign of β, since Equation 2.7 scales as odd powers of β. Therefore, χ can be written as

$$\chi = \begin{pmatrix} \dfrac{F_B}{|F_{AREF}| + |F_{EHD}|}, & if\ \beta \geq 0 \\ \\ \dfrac{|F_{AREF}| + F_B}{|F_{EHD}|}, & if\ \beta < 0 \end{pmatrix} \tag{2.17}$$

Equation 2.17 provides the most general form of χ but remains difficult to interpret. For the specific case $\beta < 0$, and for sufficiently strong applied fields such that $|F_{AREF}| \gg F_B$ to $O(\beta^2)$ Equation 2.17 reduces to,

$$\chi \sim \left| \frac{\beta \zeta_p}{\phi_T} \frac{L^3}{\kappa^4} \left(\frac{\omega}{D}\right)^{\frac{7}{2}} \left[\frac{\sin(\Omega' \kappa h) - \cos(\Omega' \kappa h)}{e^{\Omega' \kappa h}} \right] \right|. \quad (2.18)$$

Equation 2.18 provides various useful predictions. First, the electric potential dependency disappears since both AREF and EHD scale as the squared potential. This result suggests that particles will not change their tendency to aggregate or separate simply by increasing the applied potential, in accord with experimental observations[14]. The force balance is predicted to also depend strongly on the particle zeta potential, since the AREF electroosmotic slip directly depends on the particle surface properties. Particles with higher zeta potentials will thus have a stronger tendency to separate. Furthermore, the magnitude of χ depends strongly on ω, since AREF scales as $\omega^{\frac{3}{2}}$ and EHD scales as ω^{-2}; their ratio thus depends as $\omega^{\frac{7}{2}}$. Consequently, higher frequencies suggest a stronger repulsive interaction, but the frequency dependence is confounded by the complicated frequency dependent spatial oscillations in the magnitude of the AREF (as captured by the sinusoidal terms in Equation 2.18).

2.3 Experimental methods

Our main experimental goal is to test whether Equation 2.17 captures the observed tendency for particles to aggregate or separate. The experimental apparatus (cf. Fig. 2.1) is similar to that employed in previous work[14,15,26]. The setup uses two parallel glass slides coated with tin-doped indium oxide (ITO, 5-15 Ω sheet resistance) separated by a nonconductive 500 μm thick silicon spacer (Electron Microscopy Sciences). Prior to each experiment, the electrodes were washed with RBS 35 detergent, then ultrasonicated in detergent, acetone, and deionized (DI) water for 10 min each, and finally dried with filtered compressed air. Aqueous solutions for seven different univalent binary electrolytes, NaOH, LiOH, NaBr, KBr, KCl, potassium acetate (KAc), and LiI were prepared at 1.0 mM using Millipore-grade DI water (18.2 MΩ cm). Colloidal suspensions

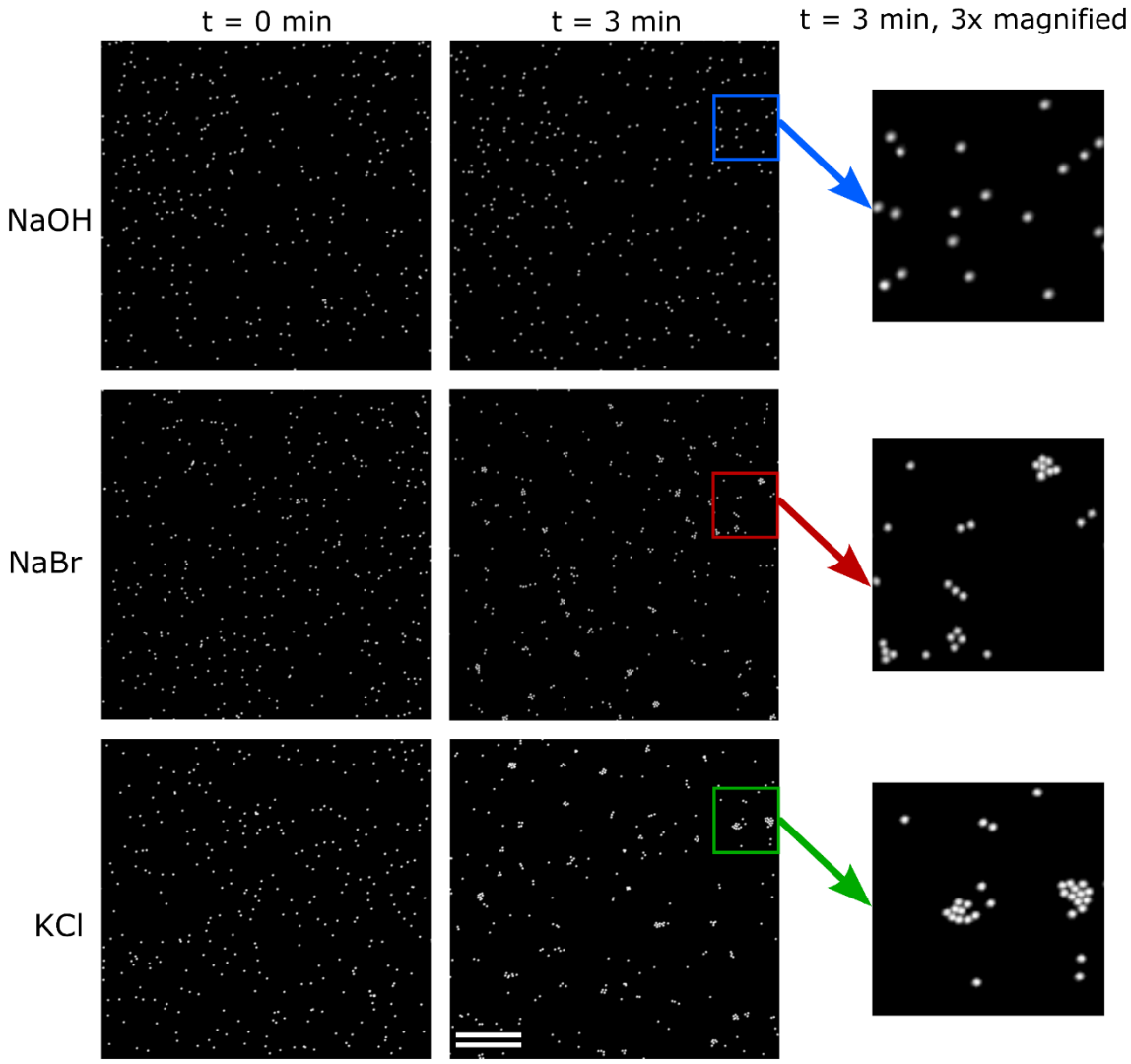

Figure 2.4. *Time-lapse planar confocal images of 2-µm diameter fluorescent particles in 1 mM solutions of NaOH, NaBr, or KCl. At t = 0 (left column) the colloids are randomly positioned. After three minutes of an 8 V_{pp}, 100 Hz electric field (right column), the particles have either separated or aggregated (magnifications at right).. The scale bar length is 100 µm.*

were then prepared by adding 2-µm diameter fluorescent sulfonated particles (Invitrogen) to each electrolyte solution at a 2×10^{-5} volume fraction. Zeta potentials of the suspended particles in each electrolyte were measured using a Malvern Zetasizer.

Prior to experimentation, 50 µL of a colloidal suspension with DI water was placed in each fluid well and allowed to dry overnight. This procedure left behind stuck particles for identifying the electrode surface location for subsequent confocal microscopy. Then, each electrolyte colloidal suspension was placed in a fluid well and allowed to sediment by gravity to the bottom electrode for 2 hours. An Agilent function generator was set at either a 4, 6, or 8 V_{pp} AC field at either 100, 500 or 1000 Hz, for a total of 3×3=9 different electric field conditions. Confocal laser scanning microscopy (Zeiss LSM 700) was then used to track both particle behavior on the electrode surface and particle height position via fluorescent emissions. Time lapsed images of the particles at a focal plane near the electrode were recorded for two minutes upon application of the field. Immediately after, a confocal height scan of 80 µm at 0.2 µm intervals was performed to capture the particle fluorescent intensities over the electrode. In between trials, the field was removed, and particles were allowed to disperse for 15 min before conducting another experiment. These experiments were repeated three times for each AC field and electrolyte type, yielding 27 sets of aggregation/separation rate data and corresponding height information.

To quantify particle aggregation rates from time-lapsed images, we adopt the particle tracking methodology from Ristenpart et al. by measuring the total number of non-aggregated, isolated particles n_1 (singlets) in the field of view[11]. By assuming that the change in singlet count is dominated by aggregation events of two singlets forming a pair, the aggregation behavior can then be characterized by second-order reaction kinetics,

$$\frac{n_1^0}{n_1} = 1 + k_e n_1^0 t, \tag{19}$$

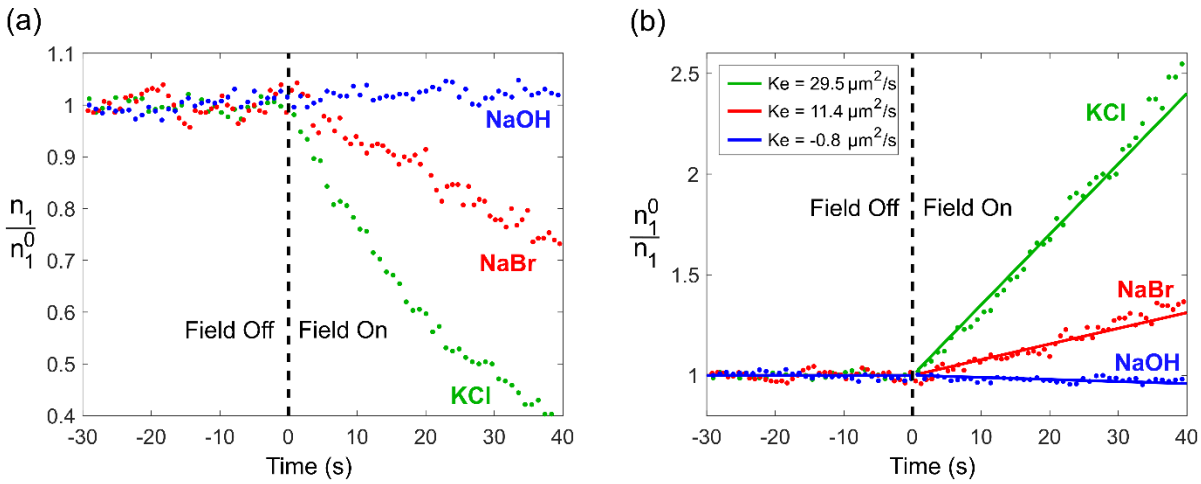

Figure 2.5. *(a) Representative unaggregated singlet particle count vs time for three different electrolytes at 8 V_{pp}, 100 Hz applied field, normalized by the initial average singlet count prior to field application. (b) Normalized inverse singlet count vs time for the same electrolytes and field conditions.*

where n_1^0 is the averaged initial singlet concentration prioWr to field application, t is time, and k_e is the characteristic aggregation rate constant that depends on the applied electric field and the colloidal suspension properties. Particle height information for each particle was extracted from the confocal image stack, with the peak fluorescence intensity corresponding to the particle center location. These individual intensities were then recorded for 60-300 particles across trials, depending on the number of identifiable aggregates and singlets.

2.4 Results and discussion

Representative top-view, time-lapse images of the colloids, acquired at the focal plane near the electrode surface, are shown in Fig. 2.4 for three different electrolyte types responding to application of an 8 Vpp, 100 Hz applied potential. Three qualitatively different types of behavior are observed. The particles suspended in NaOH (top row) exhibited strong separation; the particles suspended in NaBr exhibited a 'weak' aggregation; and the particles in KCl exhibited a strong aggregation. Qualitatively this behavior is consistent with prior observations[14]. To quantify this behavior, Fig. 2.5a shows representative singlet particle counts, normalized by the initial singlet

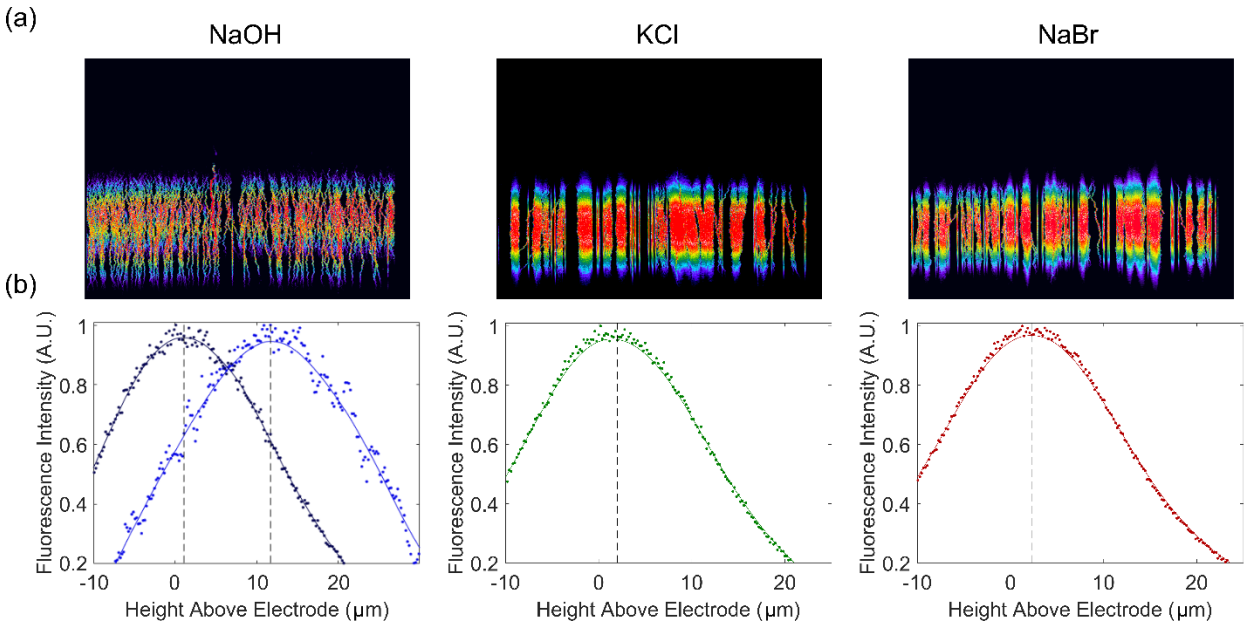

Figure 2.6. *(a) Representative false-colored confocal cross section of the image stack for particle fluorescence in a NaOH, KCl, or NaBr solution. Image width is 500 μm, height of 80 μm, taken at 0.2 μm intervals. (b) Particle fluorescence intensity profiles relative to electrode surface for two representative isolated particles for NaOH, and one representative particle for both KCl and NaBr.*

count, as a function of time for three different electrolytes. When the field is applied, the singlet count decays at different rates for NaBr and KCl suspensions, while singlet count slightly increases for NaOH suspensions. The inverse singlet count, shown in Fig. 2.5b, reveals a linear trend for $t < 15$ s for KCl and NaBr, and a negative trend for NaOH. Following Equation 2.19, representative aggregation rate constants k_e are obtained for each trial. The negative k_e value indicates that the singlet count in the field of view increases; particles that initially happened to be in close proximity at $t = 0$ move apart in response to the applied field, causing the singlet count to increase. Although the magnitude of negative k_e will thus depend on the initial number of aggregates, the presence of negative or near zero k_e values identify conditions with negligible aggregation behavior. Experiments with other electrolytes showed that LiOH also caused strong

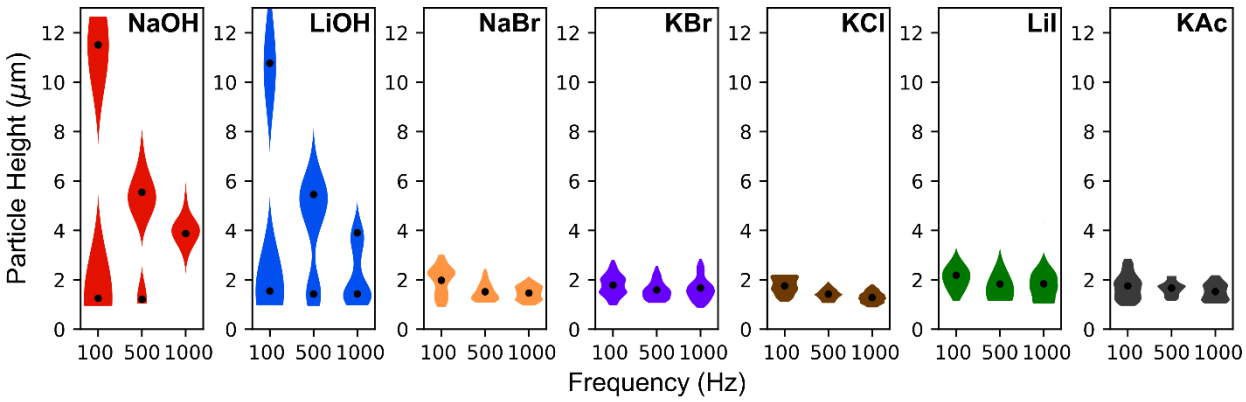

Figure 2.7. *Violin plots of particle height distributions for various electrolytes at 100, 500, and 1000 Hz for an 8 V_{pp} applied potential. Heights are measured from the electrode surface to particle center, with particle radius of 1 micron for all cases. These heights were collected from the individual fluorescence intensities of each particle found across three separate trials, yielding N = 60 to 300 samples. The black dots indicate the average particle height for each condition; bifurcated populations for NaOH and LiOH were separated into two subgroups and were averaged independently.*

separation, while LiI induced weak aggregation and KAc and KBr induced strong aggregation (representative raw data not shown).

The preceding data provided insight on overall aggregation or separation behavior, but the confocal microscope is also able to provide sensitive measures of the average particle height over the electrode. Fig. 2.6 shows representative cross sections of the false-colored confocal image stacks of the particle fluorescence for three different electrolytes, while Fig. 2.7 shows violin plots indicating the observed particle height distributions for all seven electrolytes. In the case of NaOH and LiOH, height bifurcation was observed, similar to the levitation previously reported with KOH and NaOH[26,27]. For all other electrolyte cases, particles were found within one to two particle radii away from the surface, with no discernable bifurcation. Particles in general were observed to occupy higher positions of approximately one particle diameter from the electrode at 100 Hz and recede closer to the electrode surface at 500 and 1000 Hz, consistent with observations noted by Dutcher et al. for KCl aggregate experiments[13].

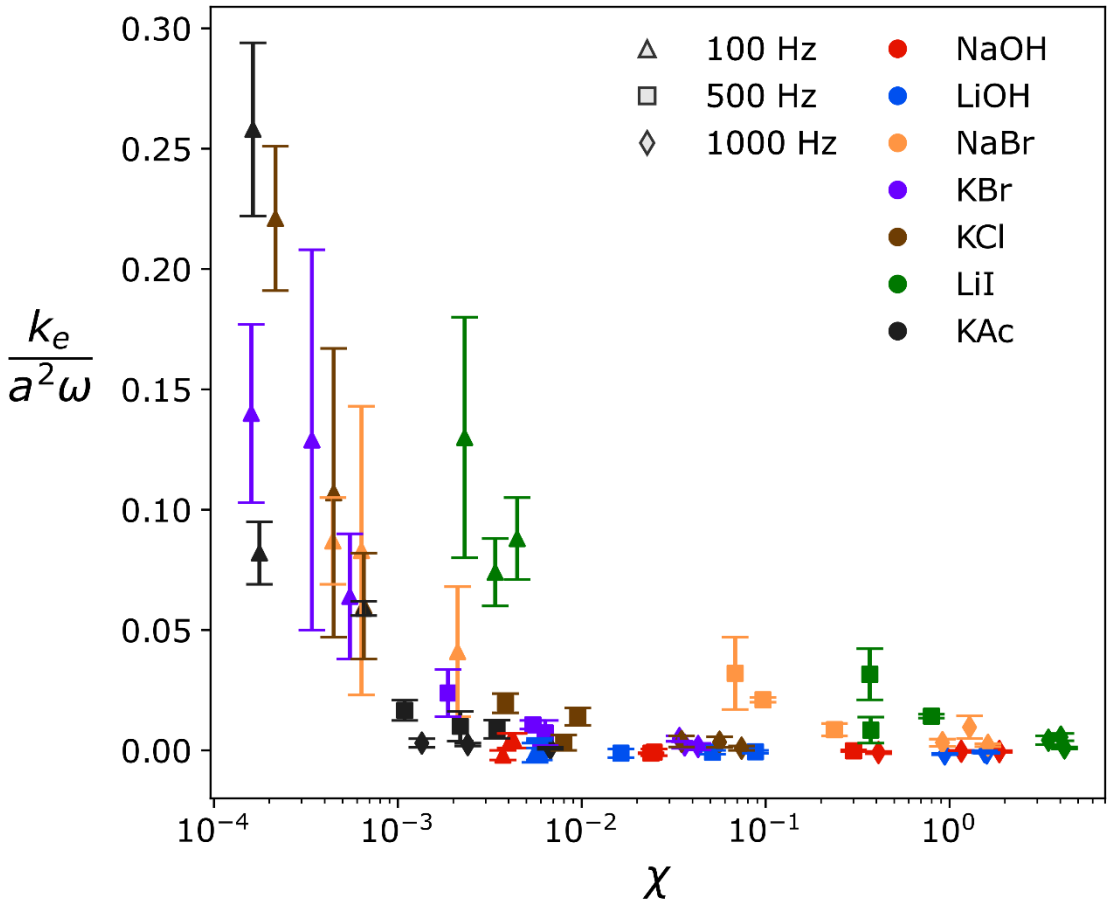

Figure 2.8. *Semi-log plot of aggregation rate constant k_e vs. the dimensionless force balance χ for applied potentials of 4, 6, and 8 V_{pp}. The marker shape denotes frequency; the marker color denotes the electrolyte type. Error bars represent ±1 standard deviation over three trials.*

With quantitative measures of the aggregation rate (cf. Fig. 2.5) and quantitative measures of the average particle height (Fig. 2.7), we now have everything necessary to estimate χ and test the hypothesis that the aggregation versus separation behavior is based on the competition between the two types of electrically induced fluid flow. Fig. 2.8 shows the experimentally determined aggregation rates k_e, normalized on $a^2\omega$, as a function of our theoretical χ using Equation 2.17. In the cases where height bifurcation was observed, the particle heights were evaluated using the particle population closer to the electrode, a choice motivated by prior observations that aggregation is observed for NaOH and KOH at applied frequencies below 25 Hz[15]. Aggregation

rate data are shown for the three different voltages and three frequencies applied across seven different electrolyte solutions for a total of 63 different experimental conditions, revealing an overall negative correlation between the observed aggregation behavior and χ. When χ was roughly $O(10^{-2})$ or larger, the dimensionless aggregation rate was either small or weakly negative. At smaller values of χ, the corresponding aggregation rate strongly increased. These results strongly suggest the combination of F_{AREF}, F_B, and F_{EHD} scaling approximations subsumed within χ provide predictions that accord with the observed trends. Looking at the electrolyte dependence, our results indicate that for NaOH and LiOH solutions, which have the highest ionic mobility mismatches and consequently large $\langle E_{AREF} \rangle$, generally yielded the larger χ values across the different field settings tested. Conversely, KCl and KBr with the lowest ionic mobility mismatches generally yielded smaller χ values and stronger aggregation behavior.

An important point is that in the experimental conditions examined here, all measured particles zeta potentials were negative, since positively charged particles tend to stick irreversibly to the electrode surface. Thus, we were unable to directly test the influence of the sign of the particle zeta potential. Instead, we note that all tested electrolytes except KAc had a diffusivity mismatch greater than one ($\beta > 0$). In the unique case of KAc, which has $\beta < 0$, we expect the F_{AREF} to apply in the reverse direction, i.e., the AREF assists the EHD flow rather than hinders it, since the sign of AREF depends on the sign of β (cf. Fig. 2.3, black curve). Importantly, the colloidal particles suspended in KAc yielded the largest aggregation rates of all those observed experimentally (cf. black triangles in Fig. 2.8). Taken together, the results indicate that a balance of electroosmotic slip flow induced by the AREF on the particle surface indeed provides a sufficiently strong flow to counter the EHD flow generated on the particle surface and cause separation.

Several caveats are worth emphasizing. We stress that the electrolyte dependency for χ is inherently complex; changing the identity of the electrolyte affects the magnitude and sign of both ζ_p and $\langle E_{AREF} \rangle$. An applied field with a large $\langle E_{AREF} \rangle$ at the particle position may be rendered ineffective if the ζ_p is sufficiently small. Likewise, changing the applied field frequency affects the dynamics of both EHD and AREF-induced forces. Equation 2.18 only pertains to a narrow range of frequencies, outside of which the aggregation behavior is challenging to predict. The particle height also plays an important role in this model. The EHD flow strength roughly decays as h^{-4}; however, AREF induced forces can persist several microns into the bulk, as predicted by the AREF length scale $\mathcal{L}_D = \sqrt{\frac{\sqrt{D_+ D_-}}{f}}$. AREF induced forces will also increase in magnitude in the limit towards the electrode surface due to the large gradients in AREF near the electrode. A fully predictive model would need to calculate *a priori* the particle height resulting from a balance of upward hydrodynamic forces and downward gravitational force.

Although the scaling arguments yield a correlation consistent with the hypothesized impact of the electrokinetic flows, the detailed streamlines associated with the superimposed flows remain to be established. The spatial oscillations in the magnitude of the AREF vary with a length scale that is comparable to the micron-scale colloid size, meaning that both the magnitude and the direction of the AREF may appreciably change from one side of the particle to the other. Due to the large gradient in AREF near the electrode surface, one can expect significantly larger slip velocities near the bottom of a particle. The point dipole approximation also neglects the interactions between the particle finite volume and the local AREF, which would further convolute the electrokinetic behavior in the vicinity.

Another important caveat is that our estimate for the relative magnitudes of AREF induced electroosmotic flow and EHD induced flow pertains strictly to low applied potentials, so there is no voltage dependence in our χ parameter (when the flow dominates over thermal forces). There are reasons to believe, however, that the AREF induced flow scales in a more complicated fashion with the applied potential. For example, Rath et al. use a numerical correlation to predict the AREF-induced peak fluid flow strength, reporting comparable fluid flows that surpass faradaic contributions from the applied direct current[31]. For applied potentials exceeding 5 V_{pp}, the resulting scale for AREF becomes unclear. Current theoretical data on AREF have not yet captured the magnitude of AREF at these high applied voltages. Based upon the numerical correlations provided by Hashemi et al., the consequent predicted magnitudes are likely underestimated at the intermediate voltages below 5 V_{pp}, and overestimated beyond 5 V_{pp}[30]. Nonetheless, our scaling model at the low potential limit provides key quantitative insights regarding AREF induced electrokinetic effects on particle aggregation that accords with experimental data across several different applied fields and electrolyte identities.

2.5 Summary

In conclusion, we present a theoretical parameter χ that compares the magnitude of the EHD hydrodynamic drag force to that of an AREF-induced drag force and thermal forces. Our results clearly demonstrate a negative correlation between χ and the experimentally observed aggregation rate k_e across seven different electrolytes at several different applied fields. Appreciable aggregations rates are only observed for $\chi \ll 1$, i.e., for when EHD induced flow on the electrode is predicted to dominate over AREF-induced electroosmotic slip on the particle surface. This model thus serves as a starting point for understanding the role of AREF in colloidal aggregation systems, especially at the micron length scale.

Our results suggest several new possibilities that have not yet been explored. Given the high mobility of hydrogen ions, acidic solutions can potentially exhibit unique aggregation behavior, provided that the particle zeta potential is appreciable. These electrolyte solutions are normally avoided due to potential etching of the ITO surface but could potentially be investigated with other materials. Our model also suggests a linear correlation between χ and particle zeta potential; surface modifications on the colloidal particle for a particular electrolyte solution could be performed to verify this scaling behavior. Experimental data is also lacking for the general class of electrolytes with ternary systems or multivalent electrolytes. Further research into these categories may broaden the potential application of AREF-assisted colloid manipulation for particle assembly and sorting.

2.6 References

1. Richetti, P., Prost, J. & Barois, P. Two-dimensional aggregation and crystallization of a colloidal suspension of latex spheres. *J. Phys. Lett.* **45**, 1137–1143 (1984).
2. Trau, M., Seville, D. A. & Aksay, I. A. Field-induced layering of colloidal crystals. *Science* **272**, 706–709 (1996).
3. Trau, M., Saville, D. A. & Aksay, I. A. Assembly of colloidal crystals at electrode interfaces. *Langmuir* **13**, 6375–6381 (1997).
4. Böhmer, M. In situ observation of 2-dimensional clustering during electrophoretic deposition. *Langmuir* **12**, 5747–5750 (1996).
5. Giersig, M. & Mulvaney, P. Preparation of ordered colloid monolayers by electrophoretic deposition. *Langmuir* **9**, 3408–3413 (1993).
6. Solomentsev, Y., Böhmer, M. & Anderson, J. L. Particle clustering and pattern formation during electrophoretic deposition: a hydrodynamic model. *Langmuir* **13**, 6058–6061 (1997).
7. Kim, J., Guelcher, S. A., Garoff, S. & Anderson, J. L. Two-particle dynamics on an electrode in ac electric fields. *Adv. Colloid Interface Sci.* **96**, 131–142 (2002).
8. Kim, J., Anderson, J. L., Garoff, S. & Sides, P. J. Effects of zeta potential and electrolyte on particle interactions on an electrode under ac polarization. *Langmuir* **18**, 5387–5391 (2002).
9. Fagan, J. A., Sides, P. J. & Prieve, D. C. Vertical oscillatory motion of a single colloidal particle adjacent to an electrode in an ac electric field. *Langmuir* **18**, 7810–7820 (2002).
10. Prieve, D. C., Sides, P. J. & Wirth, C. L. 2-D assembly of colloidal particles on a planar electrode. *Curr. Opin. Colloid Interface Sci.* **15**, 160–174 (2010).

11. Ristenpart, W. D., Aksay, I. A. & Saville, D. A. Assembly of colloidal aggregates by electrohydrodynamic flow: kinetic experiments and scaling analysis. *Phys. Rev. E - Stat. Nonlinear Soft Matter Phys.* **69**, 1–8 (2004).
12. Ristenpart, W. D., Aksay, I. A. & Saville, D. A. Electrohydrodynamic flow around a colloidal particle near an electrode with an oscillating potential. *J. Fluid Mech.* **575**, 83–109 (2007).
13. Dutcher, C. S., Woehl, T. J., Talken, N. H. & Ristenpart, W. D. Hexatic-to-disorder transition in colloidal crystals near electrodes: rapid annealing of polycrystalline domains. *Phys. Rev. Lett.* **111**, 1–5 (2013).
14. Woehl, T. J., Heatley, K. L., Dutcher, C. S., Talken, N. H. & Ristenpart, W. D. Electrolyte-dependent aggregation of colloidal particles near electrodes in oscillatory electric fields. *Langmuir* **30**, 4887–4894 (2014).
15. Bukosky, S. C. & Ristenpart, W. D. Simultaneous aggregation and height bifurcation of colloidal particles near electrodes in oscillatory electric fields. *Langmuir* **31**, 9742–9747 (2015).
16. Saini, S., Bukosky, S. C. & Ristenpart, W. D. Influence of electrolyte concentration on the aggregation of colloidal particles near electrodes in oscillatory fields. *Langmuir* **32**, 4210–4216 (2016).
17. Ruud, E. D. & Dutcher, C. S. Electrohydrodynamic aggregation with vertically inverted systems. *Phys. Rev. E* **97**, 1–6 (2018).
18. Fagan, J. A., Sides, P. J. & Prieve, D. C. Calculation of ac electric field effects on the average height of a charged colloid: effects of electrophoretic and Brownian motions. *Langmuir* **19**, 6627–6632 (2003).

19. Fagan, J. A., Sides, P. J. & Prieve, D. C. Vertical motion of a charged colloidal particle near an AC polarized electrode with a nonuniform potential distribution: theory and experimental evidence. *Langmuir* **20**, 4823–4834 (2004).
20. Fagan, J. A., Sides, P. J. & Prieve, D. C. Evidence of multiple electrohydrodynamic forces acting on a colloidal particle near an electrode due to an alternating current electric field. *Langmuir* **21**, 1784–1794 (2005).
21. Fagan, J. A., Sides, P. J. & Prieve, D. C. Mechanism of rectified lateral motion of particles near electrodes in alternating electric fields below 1 kHz. *Langmuir* **22**, 9846–9852 (2006).
22. Hoggard, J. D., Sides, P. J. & Prieve, D. C. Electrolyte-dependent pairwise particle motion near electrodes at frequencies below 1 kHz. *Langmuir* **23**, 6983–6990 (2007).
23. Hoggard, J. D., Sides, P. J. & Prieve, D. C. Electrolyte-dependent multiparticle motion near electrodes in oscillating electric fields. *Langmuir* **24**, 2977–2982 (2008).
24. Wirth, C. L., Rock, R. M., Sides, P. J. & Prieve, D. C. Single and pairwise motion of particles near an ideally polarizable electrode. *Langmuir* **27**, 9781–9791 (2011).
25. Wirth, C. L., Sides, P. J. & Prieve, D. C. Electrolyte dependence of particle motion near an electrode during ac polarization. *Phys. Rev. E - Stat. Nonlinear Soft Matter Phys.* **87**, 032302 (2013).
26. Woehl, T. J., Chen, B. J., Heatley, K. L., Talken, N. H., Bukosky, S. C., Dutcher, C. S. & Ristenpart, W. D. Bifurcation in the steady-state height of colloidal particles near an electrode in oscillatory electric fields: evidence for a tertiary potential minimum. *Phys. Rev. X* **5**, 011023 (2015).

27. Bukosky, S. C., Hashemi, A., Rader, S. P., Mora, J., Miller, G. H. & Ristenpart, W. D. Extreme levitation of colloidal particles in response to oscillatory electric fields. *Langmuir* **35**, 6971–6980 (2019).
28. Russel, W. B., Saville, D. A. & Schowalter, W. R. *Colloidal Dispersions*. (Cambridge University Press, 1989).
29. Hashemi, A., S. M. H., Bukosky, S. C., Rader, S. P., Ristenpart, W. D. & Miller, G. H. Oscillating electric fields in liquids create a long-range steady field. *Phys. Rev. Lett.* **121**, 185504 (2018).
30. Hashemi, A., S. M. H., Miller, G. H. & Ristenpart, W. D. Asymmetric rectified electric fields between parallel electrodes: numerical and scaling analyses. *Phys. Rev. E* **99**, 062603 (2019).
31. Rath, M., Weaver, J., Wang, M. & Woehl, T. pH-mediated aggregation-to-separation transition for colloids near electrodes in oscillatory electric fields. *Langmuir* **37**, 9346–9355 (2021).
32. Hashemi, A., S. M. H., Miller, G. H., Bishop, K. J. M. & Ristenpart, W. D. A perturbation solution to the full Poisson-Nernst-Planck equations yields an asymmetric rectified electric field. *Soft Matter* **16**, 7052–7062 (2020).
33. Balu, B. & Khair, A. S. A thin double layer analysis of asymmetric rectified electric fields (AREFs). *J. Eng. Math.* **129**, (2021).
34. Hinch, E. J., Sherwood, J. D., Chew, W. C. & Sen, P. N. Dielectric response of a dilute suspension of spheres with thin double layers in an asymmetric electrolyte. *J. Chem. Soc. Faraday Trans. 2 Mol. Chem. Phys.* **80**, 535–551 (1984).

Chapter 3: Particle motion in microchannels with unimodal electric fields

Asymmetric rectified electric fields (AREFs) have recently been established to induce a steady electric field in liquids in response to an applied oscillatory electric field, provided the ions present have unequal mobilities. Here we examine the influence of AREFs on the motion of colloidal particles suspended in a thin flat microchannel between parallel electrodes. For unimodal fields, we demonstrate that the pseudo-steady particle distribution is consistent with the AREF inducing both electrophoretic drift of the particles and electroosmotic flows generated on the channel surfaces. Theoretical calculations of the 2-D fluid flow field inside the channel with an electroosmotic slip boundary condition induced by the AREF provide predictions for the net drag forces acting upon the particles that accord with the experimentally observed particle distributions. These findings point to application of oscillatory fields for tunable particle manipulation and micron-scale assembly processes.

3.1 Introduction

Colloidal particles suspended in an aqueous electrolytic solution under AC polarization can exhibit aggregation or separation lateral to a nearby electrode surface. Further, in some cases colloidal particles will "levitate" away from an electrode; simultaneous aggregation and particle levitation behavior were first observed by Bukosky and Ristenpart at low frequencies below 25 Hz for particles suspended in hydroxide solutions[1]. Surprisingly, the particles levitate at heights inconsistent with a force balance predicated on the gravitational force, short range (i.e. nanometer) colloidal forces, and electrohydrodynamic drag force predictions[1–5]. Instead, the aggregation and levitation behavior under AC polarization can be qualitatively explained by asymmetric electric fields (AREFs), which exist when the ionic diffusivities of a binary electrolyte are not equal[6,7]. Rath et al. show that colloidal particle aggregation to separation transition can be induced using a para-benzoquinone solution and accord with predictions based upon an AREF-induced electroosmosis (EOS) on the particle surface[8]. Bukosky et al. also showed that particle height levitation in hydroxide solutions scales as the AREF length scale $\mathcal{L}_D = \sqrt{\sqrt{D_+ D_-}/f}$ for applied frequency f and cation and anion diffusivities D_+ and D_- respectively, via a balance between an AREF electrophoretic force and a gravitation force[9].

While a vast literature exists on particle aggregation, particle levitation has been more difficult to observe, especially for electrolytes other than hydroxides. A traditional method to investigate dielectric particle behavior under AC fields is to confine the colloidal suspension between two indium tin oxide (ITO) glass slides[10–12] held flat (perpendicular to gravity). The optical transparency is amenable to standard microscopy techniques for observing particle motion lateral to the electrode surface. Detailed particle height information, however, becomes more challenging to observe in this configuration. Fluorescent confocal microscopy, which can

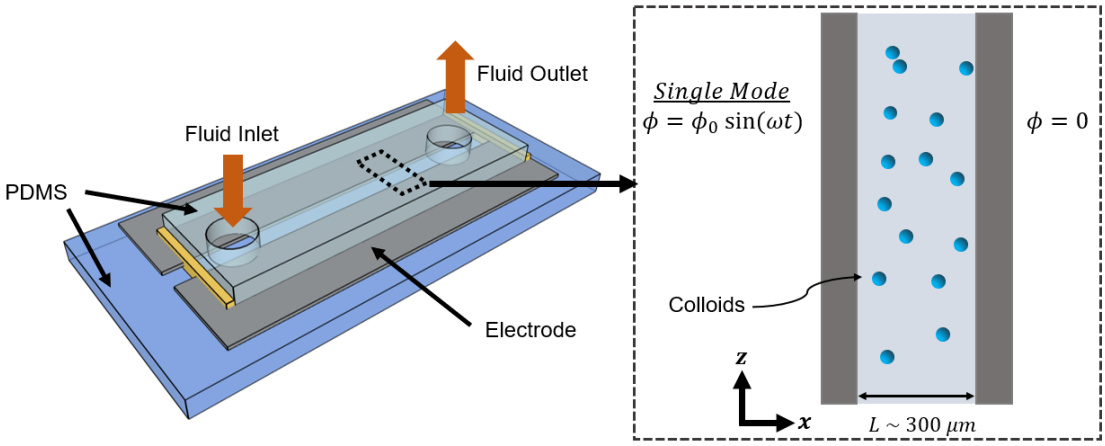

***Figure* 3.1.** *Schematic of the experimental set up. A microchannel with a width of 300 µm, height of 15 µm, and length of 1 cm is formed using two planar sheets of stainless steel and PDMS. An oscillatory potential is applied on one side and grounded on the other. Colloidal suspension is injected and observed using optical microscopy.*

provide such particle height information, typically yields low frame rates that obscure the time-dependent motion of particles[1,3,9]. Other methods, such as total internal reflection microscopy, can record particle oscillatory motions but are confined to a narrow submicron range[5,13]. In all cases, gravity plays an active role in the particle position, where an AREF-induced electrophoresis could be too weak to overcome the gravitational force.

An alternative approach is to employ a microchannel geometry, where the applied field is orthogonal to gravity. Electrodes are typically inserted at the inlet and outlet reservoirs, with various modifications along the channel to produce various mixing, pumping, and particle sorting techniques[14–17]. Such systems have an electrode spacing L typically several millimeters wide and is significantly larger than the channel width W or thickness H.

Here we are interested in conditions where L is on the order of hundred of microns or less and where the dielectric particle response parallel to the applied field is not fully understood. In this chapter, we provide comparisons between experimentally observed particle positions to

AREF-induced force predictions using a modified microchannel approach. As shown in Fig. 3.1, two planar electrodes serve as the vertical walls of the microchannel, confined by two slabs of polydimethylsiloxane (PDMS) above and below. This set up yields a long channel where the relevant electrokinetics occur in the cross-section area of the channel, and in which the channel can be modeled as infinitely long to neglect end effects. Under such confinement, an electroosmotic flow (EOF) is expected to occur in the bulk due to an EOS condition along the channel walls. In contrast to the classic model of EOS flow engendered in a capillary[18], the AREF is spatially nonuniform so a complicated fluid pattern is generated. Thus, we also provide a mathematical model with a prediction of the 2-D EOF distribution for quantitative comparisons to experimental results. Consideration of EOF and AREF-induced electrophoresis (EP) provides predictions consistent with the observed particle distributions.

3.2 Theory

3.2.1 Mathematical model of the AREF-induced EOF

Consider two planar conducting walls separated by distance L and confined by two dielectric walls of height H. Here we define our coordinate system x as the lateral position along L and vertical position y along H. For a channel length significantly longer than either L or H, the model can be treated as a 2-D problem bounded by the channel cross-sectional area. In capillary or micro electrophoresis, application of a DC field of magnitude E yields the well-known lateral flow profile u as

$$u = -\frac{\varepsilon\varepsilon_0\zeta_w E}{\mu}\left[1 + 6\left(\frac{y^2}{H^2} - \frac{y}{H}\right)\right], \tag{3.1}$$

where the u is the lateral fluid velocity between the electrodes, ε is the absolute permittivity, and ε_0 is the fluid relative permittivity[18]. This flow profile, valid for regions far from the electrodes,

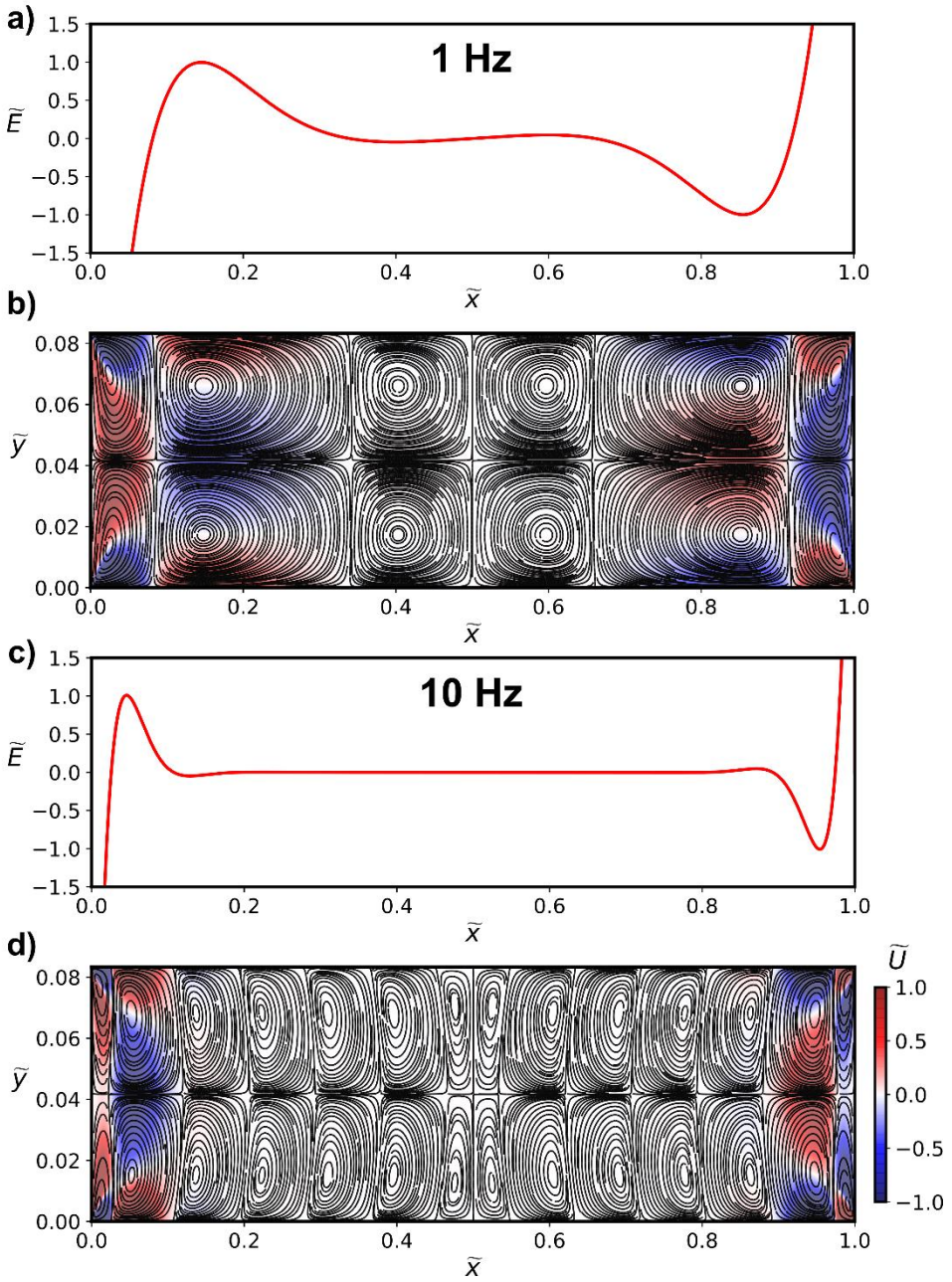

Figure 3.2. *a,b) Representative AREF spatial distribution for 1 Hz waveform with accompanying streamline predictions due to an AREF slip condition (axes not to scale). c,d) AREF distribution for 10 Hz waveform with accompanying streamline predictions. Colorbar indicates lateral fluid flow strength in the $\tilde{x}$ direction, scaled by the peak flow U_{pk}.*

occurs as a result of an EOS along the channel wall with a zeta potential ζ_w and is balanced by a parabolic pressure backflow for a closed system. In the case of an AC field, however, predictions for AREF indicate a complex spatial dependency on x, which complicates the induced EOF

distribution. The AREF spatial distribution can be readily resolved using a low potential, thin double layer asymptotic result provided by Balu and Khair[19] (cf. their Eq. 62), with exemplary distributions provided in Figure 3.2a and 3.2c for 1 and 10 Hz cases respectively.

Our approach follows the steady Stokes flow derivation from Meleshko for a rectangular geometry, where we solve the EOF distribution driven by an AREF-slip condition along the charged PDMS walls[20]. Neglecting electromigration terms, the governing streamfunction equation can be expressed by the biharmonic equation

$$\Delta\Delta\psi = 0, \tag{3.2}$$

subject to the conditions

$$\psi = 0 \text{ along the boundaries}, \tag{3.3}$$

$$\psi_x = v = 0 \; at \; x = 0, \text{and} \; \; x = L, \tag{3.4}$$

$$\psi_y = u = \frac{\varepsilon\varepsilon_0\zeta_w E_{AREF}(x)}{\mu} \; at \; y = 0, H, \tag{3.5}$$

where E_{AREF} is the 1-D spatial distribution of AREF. To scale the system, we use the electrode spacing L for the spatial scale $\tilde{x} = x/L$. Note that u and v refer to "lateral" flow along the x axis and "vertical" flow along the y axis. Fluid velocities is scaled by the maximum induced slip $u_{pk} = \left|\frac{\varepsilon\varepsilon_0\zeta_w E_{pk}}{\mu}\right|$ at the AREF peak E_{pk} such that $\tilde{u} = u/u_{pk}$ and $\tilde{v} = v/u_{pk}$. This peak value occurs on the AREF length scale $\mathcal{L}_d$ for applied frequency f and cation and anion diffusivities D_+ and D_- respectively. The dimensionless equations are therefore

$$\tilde{\psi} = 0 \text{ along the boundaries}, \tag{3.6}$$

$$\tilde{v} = 0 \text{ at } \tilde{x} = 0 \text{ and } \; \tilde{x} = 1, \tag{3.7}$$

$$\tilde{u} = \frac{-E_{AREF}(\tilde{x})}{E_{pk}} \text{ at } \tilde{y} = 0, \widetilde{H}. \tag{3.8}$$

AREF is antisymmetric, and we assume a constant, negative ζ_w on the top and bottom walls. Given the symmetry of the domain, the solution to the streamfunction is therefore odd around $\tilde{x}$ and even along $\tilde{y}$. Thus, a sin series expansion is applied

$$\tilde{\psi} = \sum_n a_n(\tilde{y}) \sin(\alpha_n \tilde{x}) + \sum_m b_m(\tilde{x}) \sin(\beta_m \tilde{y}) \tag{3.9}$$

with coefficients of the form

$$a_n = A_n \sinh(\alpha_n \tilde{y}) + B_n \cosh(\alpha_n \tilde{y}) + C_n \tilde{y} \sinh(\alpha_n \tilde{y}) + D_n \tilde{y} \cosh(\alpha_n \tilde{y}), \tag{3.10}$$

$$b_m = Q_m \sinh(\beta_m \tilde{x}) + R_m \cosh(\beta_m \tilde{x}) + S_m \tilde{x} \sinh(\beta_m \tilde{x}) + T_m \tilde{x} \cosh(\beta_m \tilde{x}). \tag{3.11}$$

Here the expressions for α_n and β_m are

$$\alpha_n = 2\pi n, \qquad \beta_m = \frac{2\pi m}{\widetilde{H}}. \tag{3.12, 3.13}$$

Details are as follows for resolving a_n. Given that $\tilde{\psi} = 0$ along $\tilde{y} = 0$ and $\tilde{y} = \widetilde{H}$, it follows that

$$B_n = 0, \text{and}$$

$$0 = A_n \sinh\left(\alpha_n \widetilde{H}\right) + C_n \widetilde{H} \sinh\left(\alpha_n \widetilde{H}\right) + D_n \widetilde{H} \cosh\left(\alpha_n \widetilde{H}\right).$$

Solving for A_n yields

$$A_n = \frac{-C_n \widetilde{H} \sinh\left(\alpha_n \widetilde{H}\right) - D_n \widetilde{H} \cosh\left(\alpha_n \widetilde{H}\right)}{\sinh\left(\alpha_n \widetilde{H}\right)}.$$

Rearranging terms into Eq. 10 yields

$$a_n = \frac{A(\tilde{y} - \widetilde{H})[\sinh(\alpha_n \tilde{y}) \sinh(\alpha_n \widetilde{H})] + [\tilde{y} \sinh(\alpha_n(\widetilde{H} - \tilde{y}))]}{\sinh(\alpha_n \widetilde{H})} . \quad (3.14)$$

A similar derivation from Eq. 12 is performed to find β_m. Altogether, the streamfunction of the most general form for the given symmetry is

$$\tilde{\psi} = \sum_n A_n \frac{(\tilde{y} - \widetilde{H})[\sinh(\alpha_n \tilde{y}) \sinh(\alpha_n \widetilde{H})] + [\tilde{y} \sinh(\alpha_n(\widetilde{H} - \tilde{y}))]}{\sinh(\alpha_n \widetilde{H})} \sin(\alpha_n \tilde{x})$$

$$+ \sum_m B_m \frac{(\tilde{x} - 1)[\sinh(\beta_m \tilde{x}) \sinh(\beta_m)] + [\tilde{x} \sinh(\beta_m(1 - \tilde{x}))]}{\sinh(\beta_m)} \sin(\beta_m \tilde{y}). \quad (3.15)$$

Boundary conditions are used to determine coefficients A_n and B_m. To simplify, one can define the boundary EOS slip condition $\tilde{u}_{AREF}$ as

$$\tilde{u}_{AREF} = \sum_n C_n \sin(\alpha_n \tilde{x}). \quad (3.16)$$

Solving for the flow profiles $\tilde{u}$ and $\tilde{v}$ and using Eq. 3.16 results in a linear system

$$B_m \frac{\sinh(\beta_m) - \beta_m}{\sinh(\beta_m)} = -\sum_n A_n \frac{8\alpha_n^2 \beta_m(\cosh(\alpha_n \widetilde{H}) - 1)}{\widetilde{H} \sinh(\alpha_n \widetilde{H})(\alpha_n^2 + \beta_m^2)^2} , \quad (3.17)$$

and

$$C_n = A_n \frac{\sinh(\alpha_n \widetilde{H}) - \alpha_n \widetilde{H}}{\sinh(\alpha_n \widetilde{H})} + \sum_m B_m \frac{8\alpha_n \beta_m^2 (\cosh(\beta_m) - 1)}{\sinh(\beta_m)(\alpha_n^2 + \beta_m^2)^2}. \quad (3.18)$$

Solving the linear system of Eq. 3.17 and 3.18 provides the necessary coefficients for the flow profile. Explicitly, A_n coefficients were first determined using the coefficients obtained from a discrete fast sine series of $\tilde{u}_{AREF}$. In resolving the $\tilde{u}_{AREF}$ coefficients we apply the analytic

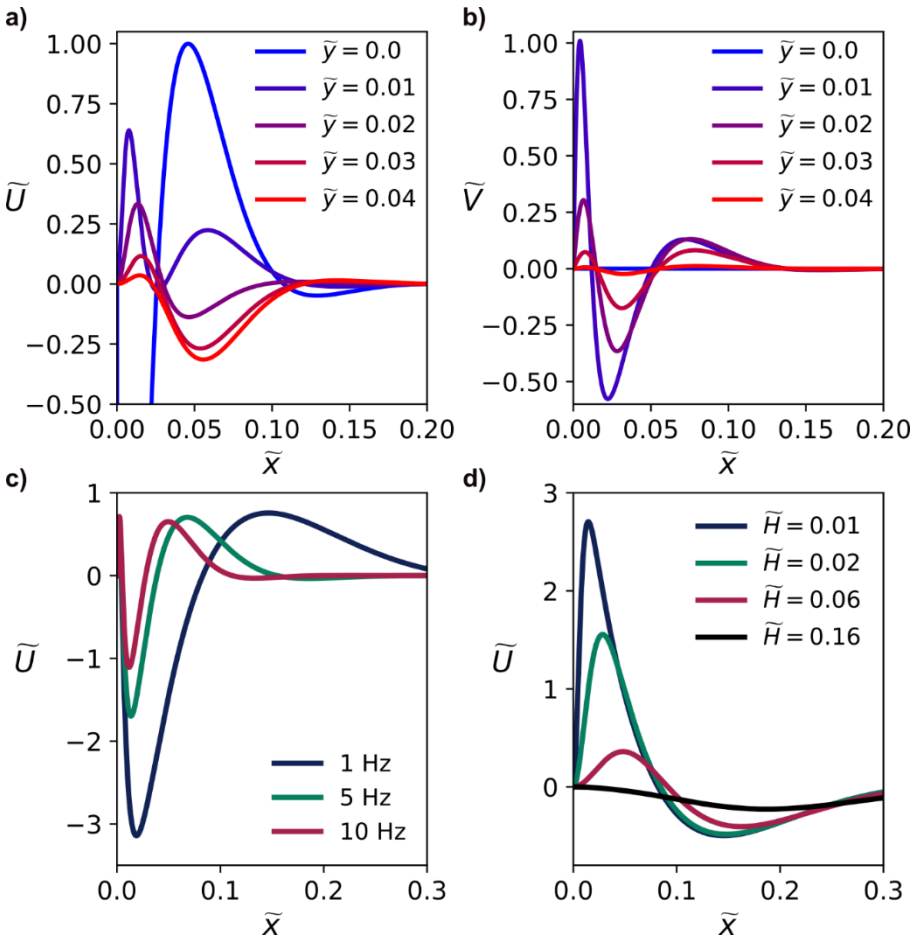

Figure 3.3. *a) Lateral flow and b) vertical flow profiles for $\tilde{H}$ = 0.08 at various heights $\tilde{y}$. c) Lateral flow profiles at various frequencies and d) varying aspect ratio $\tilde{H}$. Representative results shown here apply for a 1 mM NaOH electrolyte solution with 4 V_{pp} applied potential.*

expression for E_{AREF} from Balu and Khair in the limit of thin double layers and small applied potentials. We also enforce that the AREF is exactly zero at $\tilde{x} = 0, 1$. Then, a $M + N$ square matrix and a $M + N$ size vector consisting of each coefficient expression in Eq. 3.17 and 3.18 were constructed and solved using a standard linear matrix solver. The 2-D fluid velocity profile was then determined by resolving the appropriate partial derivative terms of Eq. 3.15.

3.2.2 Numerical predictions of bulk EOS

A systematic numerical study was conducted at integer frequencies from 1 to 20 Hz for each electrolyte to determine the EOF profile in the microchannel system. An exemplary subset

of these results is shown in Fig. 3.2 for 1 mM NaOH. The aspect ratio $\widetilde{H}$ was 0.08, to match experimental conditions. Unlike capillary electrophoresis, the spatial complexity of AREF yields flow cells across the microchannel domain, where the edge of each cell corresponds to the roots of AREF. As the frequency increases, the number of roots increase, yielding more cells. To indicate regions of appreciable flow strengths, a color bar for the lateral flow $\tilde{u}$ was superimposed on the streamlines. The flow direction follows the odd-symmetry imposed by AREF. Further, the flow quickly diminishes past the first two cells on either side of the electrode.

Further details of the flow characteristics are shown in Fig. 3.3a and 3.3b for both $\tilde{u}$ and $\tilde{v}$. Since the flow is circulatory within a cell, maximum flow reversal occurs in the middle of the channel. As noted before, the flow comparable to the peak flow induced on the PDMS wall occurs in the first two cells, which correspond to regions near $\tilde{\mathcal{L}}_d$. The flow magnitude depends greatly on the aspect ratio as well; Fig. 3.3c and Fig 3.3d indicate diminished flow strengths that largely vanish at $\widetilde{H} \sim 0.4$. Due to the sharp field near the electrode, the predicted flow increases towards the electrode surface; however, the corner effects of the microchannel between the PDMS and electrode surface is not well defined and is limited to the double layer region. At this length scale, the electric field is poorly modeled by the Eq. 3.16 with the equation used by Balu and Khair; for our purposes, the bulk fluid flow far from the double layer length remains consistent.

The presence of a background EOS indicates at least two mechanisms for net particle motion. First, AREF will induce an electroosmotic flow U_{EO} directly on the particle charged surface. Second, the bulk fluid flow U_{Drag} from the PDMS charged slip condition creates a drag flow on the particle surface. The competition between EOS flows between the particle and the

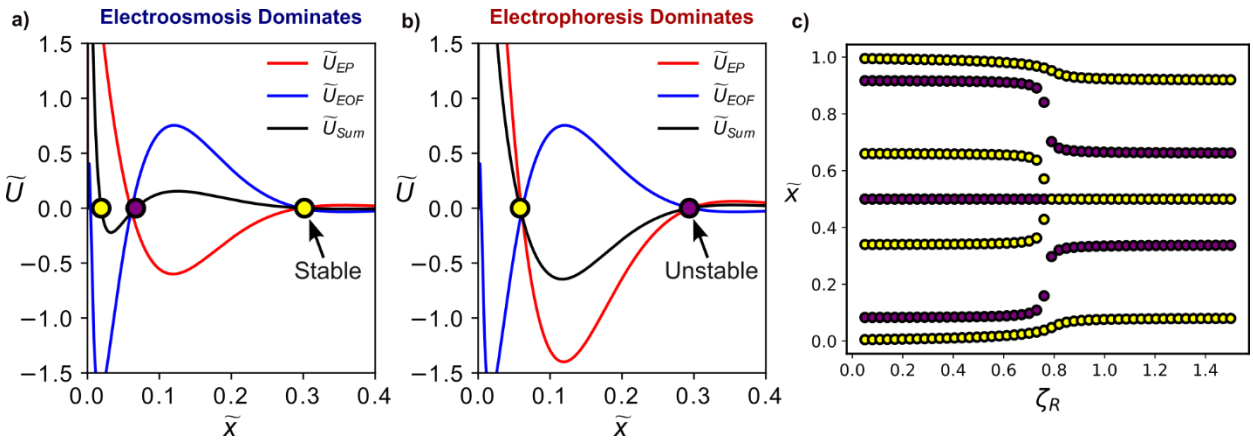

Figure 3.4. *Fluid flows vs $\tilde{x}$ for a) $\zeta_R = 0.6$ and b) $\zeta_R = 1.4$, evaluated at a height of $\tilde{y} = 0.003$ from the PDMS surface with $\tilde{H} = 0.08$ and $\tilde{L}_d = 0.13$. Sum velocity $\widetilde{U}_{Sum}$ depends on the background fluid flow $\widetilde{U}_{EOF}$ and the electrophoretic velocity $\widetilde{U}_{EP}$, resulting in different stable (yellow) or unstable (purple) roots. c) Predicted depletion zone $\Delta\tilde{x}$ for various zeta potential ratios ζ_R between the particle and wall for $\tilde{L}_d = 0.17$.*

channel surfaces is typical in DC-field cases; thus we expect it to affect the AC setting as well. Fig. 3.4a and 3.4b illustrates exemplary fluid flow strengths between the two flows. Since both flows depend on AREF, the net fluid flow U_{Total} is zero near the roots of the imposed AREF. The stability of these roots can change, however. Here Fig. 3.4a-b shows stable roots, i.e. particle trapping, in yellow and unstable roots as purple. If U_{Drag} dominates, these stable roots flip to unstable and vice versa, causing a change in particle dynamics.

Implicit in the analysis is the impact of zeta potential of the wall and particle, which will proportionally affect the EOS flow strengths. Figure 3.4c shows predictions for location of stable (yellow) and unstable (purple) roots versus various ratios of the zeta potential on the particle ζ_p and the zeta potential on the wall ζ_w at one micron from the PDMS surface, where $\zeta_R = \zeta_p/\zeta_w$. The results indicate a narrow regime of zeta potential ratios where the depletion zone length depend on ζ_R. The observed asymptotic values are consequently dependent on whether electrophoretic or background EOS dominates. In the case of low ζ_R, i.e. larger particle zeta

potentials, electrophoresis dominates and the particle position is found by the stable root of the AREF. At higher ζ_R, such that U_{Drag} becomes sufficiently large, the stable roots flip to unstable. In summary, numerical studies indicate a competition between EOS induced on the particle surface and that engendered on the channel wall for sufficiently thin microchannels, and that ζ_R may be an important indicator for determining the stable position of a particle ensemble.

3.3 Experimental methods

The experimental setup shown in Fig. 3.1. is similar to that employed by Hashemi et al. in their electrokinetic studies[21]. The microchannel consists of a sheet of polydimethylsiloxane (PDMS) placed over a glass substrate. Two stainless steel sheets of 16 μm thickness were placed ~300 μm apart over the PDMS. Two 1 mm diameter holes were punched 15 mm apart on a second PDMS sheet that was then placed over the steel sheets. The microchannel was then sealed using epoxy around the edges and clamped down. Two polyethylene tubes of 0.58 mm inner diameter were inserted into the top PDMS layer to introduce and remove fluid from the channel. Copper tape was attached to the two steel sheets to provide the oscillatory voltage and ground.

Electrolytic solutions composed of 1 mM NaOH, KCl, and NaBr were prepared using DI water (18.2 MΩ.cm), and 2 μm diameter sulfonated colloidal particles were added to these electrolyte solutions at volume fractions of 1 x 10^4. These colloidal suspensions were then introduced into the microchannel using a syringe pump (PHD 2000, Harvard apparatus). After the net fluid flow ceased following pump deactivation, a 4 V_{pp} (volts peak-to-peak) potential was applied across the channel. A digital camera mounted onto an optical microscope recorded particle behavior at a 15 fps (frames per second). After one minute, the field was turned off and the pump was used to flush new solution into the channel for 5 minutes before proceeding to the next experiment.

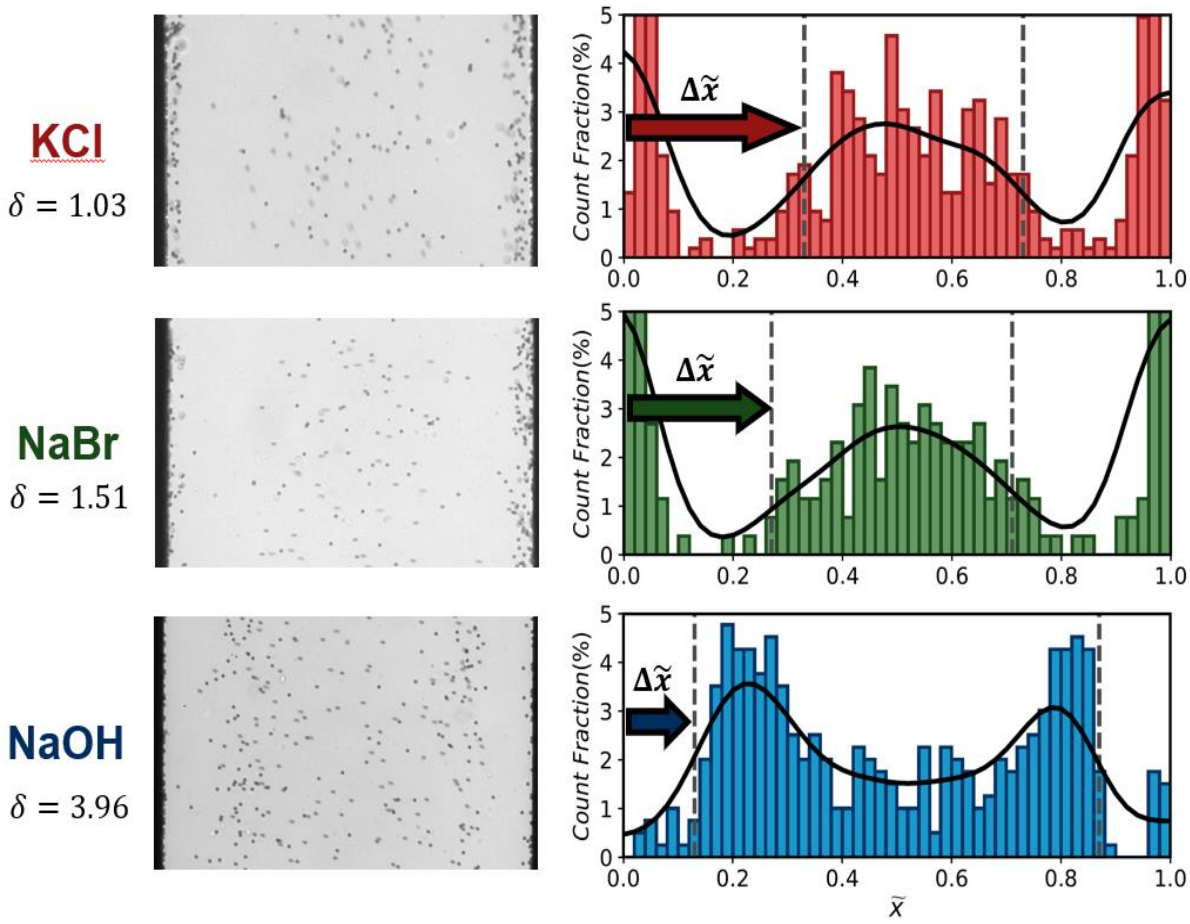

Figure 3.5. *Colloidal particle spatial distribution at 1 Hz applied frequency for various electrolytes under 4 V_{pp} oscillatory polarization after 1 min. Particle positions were obtained using image analysis based on the centroid locations for each detected object. A curve (shown in black) represents the filtered particle distribution. Depletion length $\Delta\tilde{x}$ was estimated using the maximum slope from each side, shown with the grey dotted lines.*

Image analysis using background subtraction and thresholding allows for individual identification of each particle in the focal plane. Number count histograms were then constructed using the centroid position of each particle, providing a histogram of particle spatial distribution. Quantitative values for $\Delta\tilde{x}$ were then determined using a smoothing filter on the histogram, and identifying when the fit reaches the first inflection point of the left and right side. These points require a transition from positive to negative concavity on the left side and vice versa on the right side.

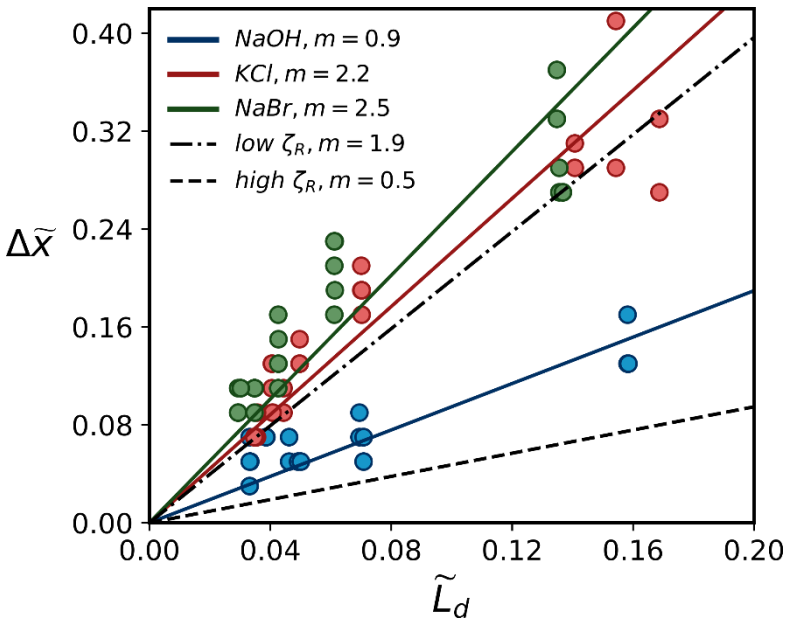

Figure 3.6. *Scatter of measured $\Delta\tilde{x}$ against $\tilde{L}_d$ for 1 mM NaOH, KCl, and NaBr. Frequencies ranged from 1-20Hz. Solid lines represent linear regression fit to the data with slope of m, while dotdashed and dashed lines show asymptotic predictions for low and high ζ_R respectively.*

3.4 Results and discussion

Particle distributions suspended in various electrolytic solutions are shown in Fig. 3.5 after 1 minute of applying a 4 V_{pp}, 1 Hz field. The key experimental observation is the formation of a depletion zone away from either electrode, the magnitude of which we define as $\Delta\tilde{x}$. Notably, even though KCl has a mobility mismatch $\delta = D_-/D_+ = 1.03$, which is extremely close to unity, a significant depletion zone was observed of approximately $\Delta\tilde{x} \sim 0.3$ for a 1 Hz applied frequency. Conversely, a NaOH colloidal suspension exhibited a shorter $\Delta\tilde{x} \sim 0.12$ under the same nominal conditions. A first assumption is that this difference in $\Delta\tilde{x}$, in the context of AREF, is due to a difference in the electrolyte mobility mismatch. Calculations of the AREF length scale $\mathcal{L}_d$ for KCl and NaOH at 1 Hz, however, yield scaled $\tilde{\mathcal{L}}_d = 0.15$ and 0.17, respectively, which suggests that $\tilde{\mathcal{L}}_d$ by itself is a poor indicator of the depletion effect. This serves as our motivation to consider the impact of EOF on the ostensible particle behavior.

With experimental measurements of $\Delta\tilde{x}$, a comparison can be performed between the observed $\Delta\tilde{x}$ and predicted stable points discussed in Section 3.3. Figure 3.6 maps these predictions to experimental data. Here, colloidal suspensions for KCl, NaOH, and NaBr over frequencies of 1-20 Hz were analyzed. For experiments conducted with KCl and NaBr, $\Delta\tilde{x}$ is predicted very well by the low ζ_R limit. For NaOH, however, it is common to find larger particle zeta potentials[1,22]. The results cause a flip in the stable roots, corresponding to a receding depletion zone across the frequencies tested. Consequently, $\Delta\tilde{x}$ observed for NaOH experiments accord with the high ζ_R limit predictions instead. The results suggest that the stark difference in $\Delta\tilde{x}$ comparing NaOH to KCl and NaBr experiments stem from different dominating EOFs. In other words, electrophoretic effects dictate the overall particle distributions for sufficiently large ζ_R, while the bulk EOS flow dictate the particle distributions for sufficiently small ζ_R. Typical ζ_p for sulfonated particles in NaOH are ~ -120 mV, while particles suspended in NaBr or KCl have zeta potentials of ~ -50 mV. Using literature values for ζ_w for PDMS for common electrolytes yield estimated ζ_R ~ 0.5 for KCl and NaBr, and $\zeta_R \sim 1.3$ for NaOH[23]. These predictions accord with the asymptotic predictions and the accompanying stable root positions. Thus, the results here indicate the plausibility of background EOS and its impact on particle net motion in the confined channel.

3.5 Conclusion

The study here is the first to provide an AREF-induced EOF prediction under a confined microchannel setting. Numerically determined stable point positions accord with experimentally observed depletion lengths, where ζ_R parameter indicates the relative strengths of the electrophoretic and bulk EOS velocities. Beyond particle manipulation, it may be possible to utilize AREF models for fluid mixing in thin channel settings, with flow strengths and patterns

tuned by an appropriate frequency. The frequencies tested here are well within the Faradaic limit, where electrochemical reactions are expected to occur. These effects were ignored in the analysis but may play a role towards other particle manipulation. Balu and Khair predicted that AREF-induced diffusiophoresis may also play a role in the net particle behavior, where the concentration gradient created by AREF drives the diffusiosmosis. We defer these concepts to future work. The numerical methodology here can be extended to other boundary conditions beyond EOS slip. For example, varying zeta potentials along the PDMS or other asymmetries will induce flow patterns as well. The only condition required is that the flow boundary condition retains symmetry along the center. These findings suggest further work towards AREF-driven particle sorting and assembly processes in thin microchannel settings.

3.6 References

1. Bukosky, S. C. & Ristenpart, W. D. Simultaneous aggregation and height bifurcation of colloidal particles near electrodes in oscillatory electric fields. *Langmuir* **31**, 9742–9747 (2015).
2. Dutcher, C. S., Woehl, T. J., Talken, N. H. & Ristenpart, W. D. Hexatic-to-disorder transition in colloidal crystals near electrodes: rapid annealing of polycrystalline domains. *Phys. Rev. Lett.* **111**, 128302 (2013).
3. Woehl, T. J., Chen, B. J., Heatley, K. L., Talken, N. H., Bukosky, S. C., Dutcher, C. S. & Ristenpart, W. D. Bifurcation in the Steady-State Height of Colloidal Particles near an Electrode in Oscillatory Electric Fields: evidence for a Tertiary Potential Minimum. *Phys. Rev. X* **5**, 011023 (2015).
4. Saini, S., Bukosky, S. C. & Ristenpart, W. D. Influence of electrolyte concentration on the aggregation of colloidal particles near electrodes in oscillatory fields. *Langmuir* **32**, 4210–4216 (2016).
5. Hoggard, J. D., Sides, P. J. & Prieve, D. C. Electrolyte-dependent pairwise particle motion near electrodes at frequencies below 1 kHz. *Langmuir* **23**, 6983–6990 (2007).
6. Hashemi, A., Bukosky, S. C., Rader, S. P., Ristenpart, W. D. & Miller, G. H. Oscillating electric fields in liquids create a long-range steady field. *Phys. Rev. Lett.* **121**, 185504 (2018).
7. Hashemi, A., Miller, G. H. & Ristenpart, W. D. Asymmetric rectified electric fields between parallel electrodes: numerical and scaling analyses. *Phys. Rev. E* **99**, 062603 (2019).
8. Rath, M., Weaver, J., Wang, M. & Woehl, T. pH-mediated aggregation-to-separation transition for colloids near electrodes in oscillatory electric fields. *Langmuir* **37**, 9346–9355 (2021).

9. Bukosky, S. C., Hashemi, A., Rader, S. P., Mora, J., Miller, G. H. & Ristenpart, W. D. Extreme levitation of colloidal particles in response to oscillatory electric fields. *Langmuir* **35**, 6971–6980 (2019).
10. Trau, M., Saville, D. A. & Aksay, I. A. Assembly of colloidal crystals at electrode interfaces. *Langmuir* **13**, 6375–6381 (1997).
11. Ristenpart, W. D., Aksay, I. A. & Saville, D. A. Assembly of colloidal aggregates by electrohydrodynamic flow: kinetic experiments and scaling analysis. *Phys. Rev. E* **69**, 021405 (2004).
12. Solomentsev, Y., Böhmer, M. & Anderson, J. L. Particle clustering and pattern formation during electrophoretic deposition: a hydrodynamic model. *Langmuir* **13**, 6058–6068 (1997).
13. Hoggard, J. D., Sides, P. J. & Prieve, D. C. Electrolyte-dependent multiparticle motion near electrodes in oscillating electric fields. *Langmuir* **24**, 2977–2982 (2008).
14. Liang, L., Ai, Y., Zhu, J., Qian, S. & Xuan, X. Wall-induced lateral migration in particle electrophoresis through a rectangular microchannel. *Journal of Colloid and Interface Science* **347**, 142–146 (2010).
15. Zhu, J., Tzeng, T.-R. J., Hu, G. & Xuan, X. DC dielectrophoretic focusing of particles in a serpentine microchannel. *Microfluid Nanofluid* **7**, 751 (2009).
16. Oh, J., Hart, R., Capurro, J. & Hongseok (Moses), N. Comprehensive analysis of particle motion under non-uniform AC electric fields in a microchannel. *Lab on a Chip* **9**, 62–78 (2009).
17. Yang, H., Jiang, H., Ramos, A. & García-Sánchez, P. AC electrokinetic pumping on symmetric electrode arrays. *Microfluid Nanofluid* **7**, 767 (2009).

18. Russel, W. B., Saville, D. A. & Schowalter, W. R. *Colloidal Dispersions*. (Cambridge University Press, 1989).
19. Balu, B. & Khair, A. S. A thin double layer analysis of asymmetric rectified electric fields (AREFs). *J Eng Math* **129**, 4 (2021).
20. Meleshko, V. V. Steady stokes flow in a rectangular cavity. *Proceedings: Mathematical, Physical and Engineering Sciences* **452**, 1999–2022 (1996).
21. Hashemi, A., Tahernia, M., Hui, T. C., Ristenpart, W. D. & Miller, G. H. Net motion induced by nonantiperiodic vibratory or electrophoretic excitations with zero time average. *Phys. Rev. E* **105**, 065001 (2022).
22. Woehl, T. J., Heatley, K. L., Dutcher, C. S., Talken, N. H. & Ristenpart, W. D. Electrolyte-dependent aggregation of colloidal particles near electrodes in oscillatory electric fields. *Langmuir* **30**, 4887–4894 (2014).
23. Kirby, B. J. & Hasselbrink Jr., E. F. Zeta potential of microfluidic substrates: 2. Data for polymers. *Electrophoresis* **25**, 203–213 (2004).

Chapter 4: Particle motion in microchannels in multimodal electric fields

Suspended colloidal particles, when subjected to a dual-mode polarization between two planar electrodes, can yield net drift, even though the imposed time-average electric field is zero. Here we show that the magnitude and direction of the drift can also be tuned by altering the phase lag between the two frequency modes. In NaOH solutions, particles form a band at a distance consistent to the AREF length scale. Similar results were found for pH neutral solution of NaBr. Increasing the applied voltage also intensifies the observed drift, but at the cost of enhanced sticking. These findings indicate new methods to manipulate colloidal particles in spatially uniform systems via multimodal waveforms.

4.1 Introduction

The ability to induce a deterministic ratchet on various micron-scale objects, such as colloids, cells, and polymers is key to many sorting and manipulation studies[1,2]. A time-averaged zero waveform, i.e. a sine wave, can yield rectified, deterministic motion by breaking various spatiotemporal symmetries[3]. An example is an on-off or flashing Brownian ratchet potential, where an asymmetric potential such as a sawtooth waveform is applied cyclically to induce a net current[4,5]. Optical traps can be used to produce such fields via a asymmetric optical tweezing[6], or by an array of asymmetric plasmonic patterns[7]. Another method is dielectrophoresis, where sharp gradients in the electric field, created by spatially non-uniform electrodes, can also yield net motion, provided that the dielectric constant of the medium and particle are different[8]. While effective, such methods typically lack generality, such that the ratchet effect will only occur with well-defined spatial patterning. Further, for Brownian-based ratchets, the strength of the rectified current strongly depends on the field, where a limited range of field properties exist to tune net motion.

An alternative, therefore, is to break the temporal symmetry of the applied field. The concept of temporal asymmetry-driven transport by applying a multimodal electric field in a colloidal suspension was first mentioned in western literature by Dukhin et al., which they called aperiodic electrophoresis[9]. In a spatially uniform channel, rectified motion could be achieved by using a temporally asymmetric electric field, which they claim that the particle response need only to contain nonlinear terms to induce net motion. Experimental evidence and theoretical predictions, however, were scarce. Shibata et al. produced controllable net motion of gold colloidal particles in deionized water by an asymmetric sawtooth electric field in various

geometries containing insulated electrodes[10], but the tunability of the system beyond the direction was not discussed.

Work by Hashemi et al. show that for unimodal AC fields, a time-averaged nonzero electric field called AREF can occur due to ion mobility mismatches[11,12]. Such fields have since been used to explain various electrokinetic phenomena, where linear electrokinetics models contradicted experimental observations in particle levitation and height bifurcation above an electrode[13] and lateral aggregation near an electrode surface[14]. More recently, Hashemi et al. showed that, for a dual mode function, the waveform required to induce net motion in the center of the channel must be non-antiperiodic[15]. Such a waveform, by definition, lacks a temporal symmetry such that no time shift τ maps one half of the waveform to the negative of the other half. More rigorously, an antiperiodic function $f(t)$ must satisfy

$$f(t+\tau) = -f(t). \tag{4.1}$$

A non-antiperiodic function therefore is any function that fails to have this symmetry. Hashemi et al. further exemplify the deterministic direction of the ratchet effect using a 2 μm diameter spherical colloidal suspension suspended in a dilute, 0.01mM NaOH solution. Using a 2 Hz and 4 Hz dual-mode sinusoidal electric potential, they were able to break the particle drift symmetry across the channel and induce bulk depletion of the particles. Further, by swapping the active and grounded electrode leads, they were able to reverse the direction of the asymmetric particle drift. Their study provides experimental evidence demonstrating the feasibility of particle manipulation via temporal asymmetry alone. Separate numerical studies by Hashemi et al. provide theoretical predictions for the asymmetric electric field distribution, but further experimental studies to optimize and tune the particle drift rate and direction are lacking[16].

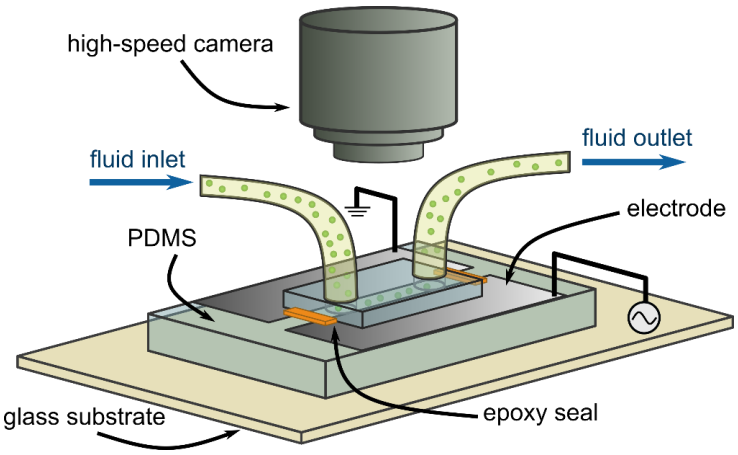

Figure 4.1. *Experimental apparatus schematic. Electrode spacing is 380 µm wide, with a channel height of 25 µm. The left electrode is grounded, while the right electrode has a multimodal voltage applied.*

Here in this chapter we investigate the effects of a phase lag ϕ between the two modes. The theory suggests that implementing a phase lag ϕ provides further control over the ratchet effect beyond simply swapping the placement of the polarized electrode. Under either NaBr or NaOH solutions, the ratchet effect was found to depend sensitively on ϕ. These findings indicate versatile alternative method to manipulate macroscopic objects in spatially uniform systems.

4.2 Materials and methods

The methods employed here are similar to that described by Hashemi et al. for their colloidal studies[15]. Such a setup is shown in Fig. 4.1., where a microchannel is formed using two thin sheets of stainless steel, 25 µm thick confined between two slabs of polydimethylsiloxane (PDMS). The channel is then sealed using epoxy, and two 1 mm diameter holes are punched into the top PDMS layer. Two polyethylene tubes with inner diameters of 0.58 mm are then attached to the top PDMS to introduce and remove fluid suspensions via a syringe pump (Harvard Apparatus PHD 2000).

A function generator (Agilent 33521A) supplies the dual mode electric polarization, which is monitored by an oscilloscope. The applied waveforms studied here are of the form

$$V(t) = V_0[\sin(\omega t + \phi) + \sin(2\omega t)], \tag{4.2}$$

for a base voltage of V_0, angular frequency ω. $V(t)$, for time t is the applied potential on one of the planar electrodes, while the other electrode is grounded. For the experiments conducted, the polarized electrode was consistently placed on the right side of the apparatus, with the grounded electrode on the left. Colloidal suspensions were made of 2 μm diameter sulfonated particles (Invitrogen) suspended in 1 mM solutions of either NaBr or NaOH to volume fractions of $1x10^{-4}$. A high-speed camera (Phantom V7.3) records the particle motion on a standard optical microscope at 100 frames per second. In between trials, the channel is flushed out for 5 minutes. Custom particle tracking code, written using Python and OpenCV package, was used to assess the ostensible particle motion.

4.3 Results and discussion

The particle ratchet response to a multimodal electric field is readily observed in time-lapse images, shown in Fig. 4.2., of a colloidal suspension under a V_0 = 1.5 V, frequency f = 2 Hz, and $\phi = \frac{3\pi}{8}$ dual-mode waveform. Initially, depletion zones rapidly form symmetrically on other side of the channel; however, the 2 μm diameter particles quickly begin drifting to the left and depleting from the channel center. This effect occurs within seconds. A tight band of particles forms on the left side, at roughly 80 μm. Estimates from the AREF length scale, defined as $\mathcal{L}_d = \sqrt{\sqrt{D_+ D_-}/f}$ for cation and anion diffusivities of D_+ and D_- respectively, for the

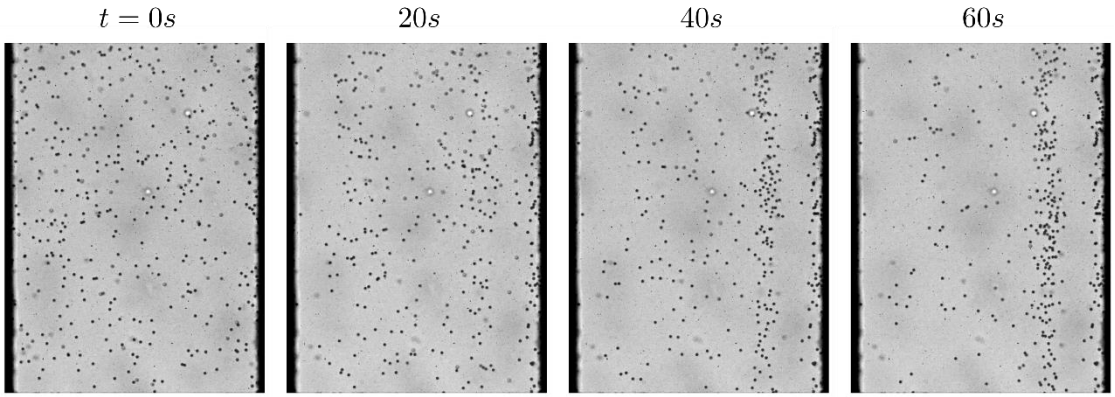

Figure 4.2. *Time lapse images of particle ratchet effect under $\phi = \frac{3\pi}{8}$, $f = 2\ Hz$, $V_0 = 1.5\ V$ waveform. Solution suspension was 1 mM NaOH, comprised of 2 μm diameter sulfonated particles. Channel width was 380 μm.*

primary frequency 2 Hz yields a similar value of , suggesting that the band position may be caused by the AREF distributions of the primary mode as discussed in the Chapter 3.

A series of optical images taken from a 1 mM NaOH suspension after dual-mode polarization for a minute at various applied phase angle ϕ under V_0 = 1.5 V_{pp} are shown in Fig. 4.3. Note that at $\phi = \pi$, the applied waveform is identical to $\phi = 0$. At $\phi = 0$ or π, two distinct bands of particles form in the bulk. Asymmetric distribution of particles become apparent at increasing ϕ, with the ratchet direction changing at around $\phi = \frac{\pi}{2}$. In the case of $\phi = \frac{\pi}{4}$ and $\frac{3\pi}{4}$, particles were completely depleted in the bulk, accumulating at the electrode wall. These results clearly indicate a variety of both drift velocities and bulk patterns, simply by tuning the phase angle. Similar results were found for a 1 mM NaBr solution, indicating that the effect is not just limited to basic pH solutions.

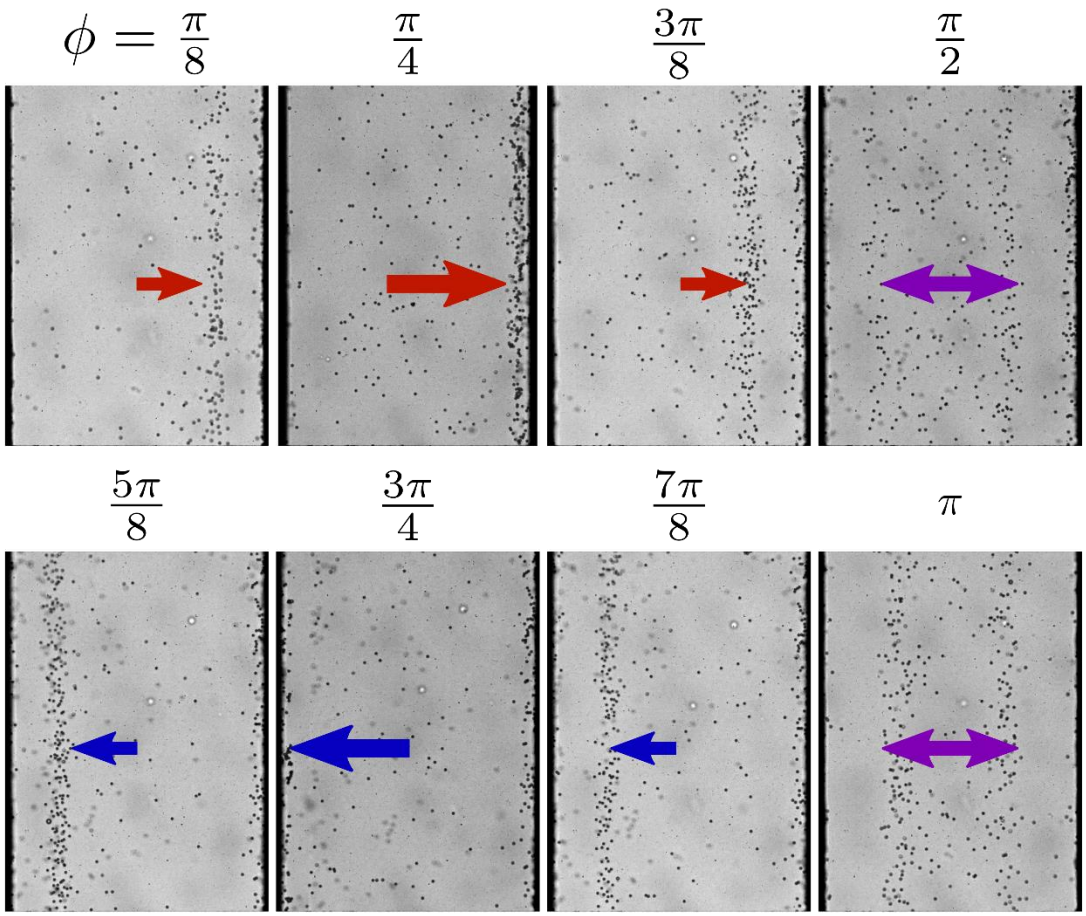

Figure 4.3. *Particle distribution at various applied ϕ in a 1 mM NaOH solution. Channel width was 380 μm.*

Given that the experiments were conducted in a thin microchannel, a background electroosmotic flow (EOF) may be relevant. Two experimental observations point towards its impact on this system. The first observation was found for a 1 mM NaOH suspension under a larger polarization of V_0 = 2 V_{pp} at $\phi = \frac{\pi}{4}$ and $\frac{3\pi}{4}$, shown in Fig. 4.4. Under these cases, asymmetric "sticking" occurs, where the particles aggregate and irreversibly stay on the PDMS surface. Fig. 4.4a shows this sticking pattern on the right side with $\phi = \frac{\pi}{4}$, while Fig. 4.4b shows the same field of view after the channel was flushed and then applied with a $\phi = \frac{3\pi}{4}$ waveform; particles then stuck onto the left side. Since the focal plane of the microscope is near the bottom

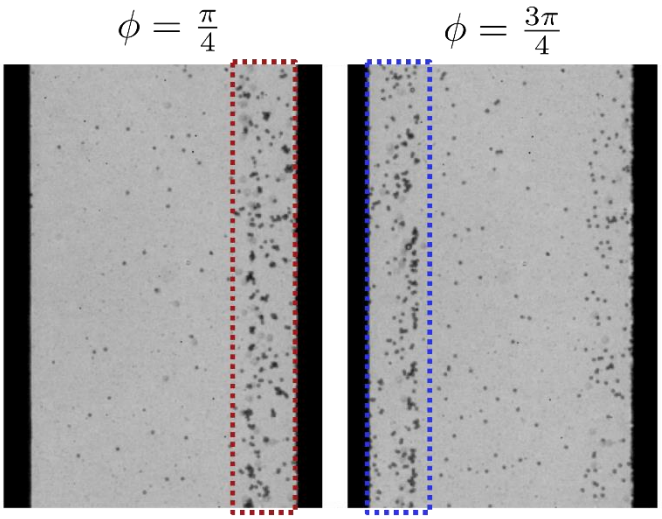

Figure. 4.4. *Evidence of particle aggregation and sticking upon application of a $V_0 = 2\ V$ field. Images were taken 15 seconds after the field was turned on. Dashed region indicates sticking locations where particles persisted after the field was turned off.*

PDMS layer, the sticking patterns suggests a downwards force that overwhelms the static repulsion from the charged layers. We surmise that this sticking pattern is due to an EOF that occurs upon application of the electric field; the asymmetry of the sticking is indicative of an asymmetric flow pattern.

A qualitative height-dependent particle motion provides the second piece of evidence. Velocity trajectories are plotted in Fig. 4.5 for two particles under a $V_0 = 1.5$ V_{pp}, $\phi = \frac{\pi}{4}$ applied field. The particle slightly out of focus oscillates in the opposite direction of the in-focus particle, both with waveforms significantly different from one another despite occupying approximately the same lateral position x in the channel. These position profiles hark back to EOF backflow in a closed channel, where the EOF from the charged walls can influence a particle's ostensible

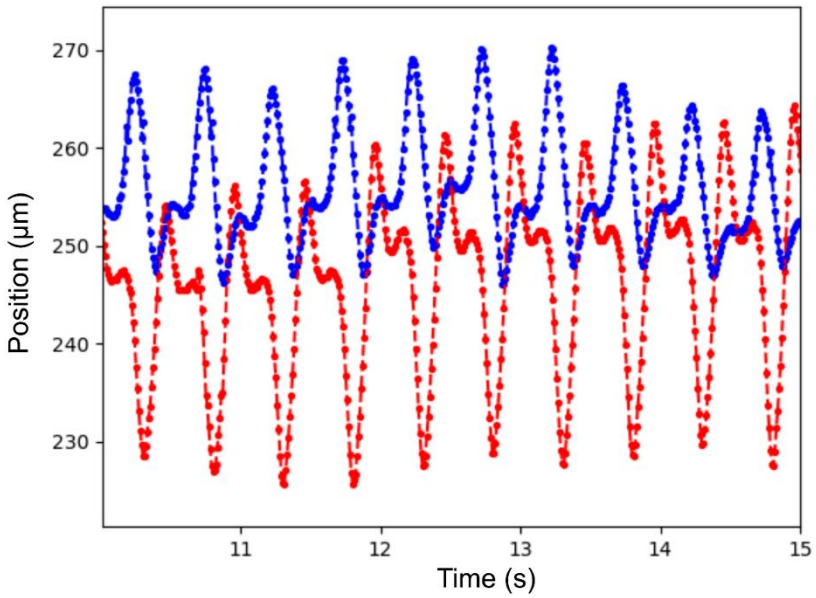

Figure 4.5. *Particle centroids over a 5 second window upon $\phi = \pi$ field.*

mobility depending on the particle height. Consequently, the observed profiles in Fig. 4.2 and 4.3 are likely results of a multimodal electrophoresis and multimodal EOFs.

These findings qualitatively indicate tunable electrokinetic ratchet via inputting a phase lag between the two modes. A caveat, however, is the possibility of complete particle depletion to the electrode edges or channel walls from an applied potential that is too large or a phase angle that yields significant depletion. Determining conditions where particles can remain pseudo-steady is necessary. Such calculations would likely involve both electrophoretic and EOF considerations. The asymmetry of this system will further complication full expressions for these terms.

An inputted phase lag between the two modes is one of many multimodal waveforms. Similarly shaped, but fundamentally different waveforms can be formed using pulsed, triangle, or square waves. The electrokinetic responses of such systems are also not known and may yield

promising alternatives as well. Nonetheless, the rapid ratchet response from a dual-mode, phase modulated waveform strongly suggests applications towards controlled particle manipulation. One proposed method would be to tune the primary frequency mode for the steady band position, and then alter the applied voltage and phase angle for the corresponding drift velocity depending on the application.

4.4 References

1. Liljeström, V., Chen, C., Dommersnes, P., Fossum, J. O. & Gröschel, A. H. Active structuring of colloids through field-driven self-assembly. *Curr. Opin. Colloid Interface Sci.* **40**, 25–41 (2019).
2. Diwakar, N. M., Kunti, G., Miloh, T., Yossifon, G. & Velev, O. D. AC electrohydrodynamic propulsion and rotation of active particles of engineered shape and asymmetry. *Curr. Opin. Colloid Interface Sci.* **59**, 101586 (2022).
3. Cubero, D. & Renzoni, F. Hidden symmetries, instabilities, and current suppression in Brownian ratchets. *Phys. Rev. Lett.* **116**, 010602 (2016).
4. Chen, H., Wang, Q. & Zheng, Z. Deterministic directed transport of inertial particles in a flashing ratchet potential. *Phys. Rev. E* **71**, 031102 (2005).
5. Ethier, S. N. & Lee, J. The flashing Brownian ratchet and Parrondo's paradox. *R. Soc. Open Sci.* **5**, 171685 (2018).
6. Wu, S.-H., Huang, N., Jaquay, E. & Povinelli, M. L. Near-field, on-chip optical Brownian ratchets. *Nano Lett.* **16**, 5261–5266 (2016).
7. Huidobro, P. A., Ota, S., Yang, X., Yin, X., Garcia-Vidal, F. J. & Zhang, X. Plasmonic Brownian ratchet. *Phys. Rev. B* **88**, 201401 (2013).
8. Germs, W. C., Roeling, E. M., van Ijzendoorn, L., Smalbrugge, B., de Vries, T., Geluk, E. J., Janssen, R. A. & Kemerink, M. High-efficiency dielectrophoretic ratchet. *Phys. Rev. E* **86**, 041106 (2012).
9. Dukhin, A. S. & Dukhin, S. S. Aperiodic capillary electrophoresis method using an alternating current electric field for separation of macromolecules. *Electrophoresis* **26**, 2149–2153 (2005).

10. Shibata, A., Komiya, K., Watanabe, K., Sato, T., Shiomi, T., Kotaki, H., Schuele, P. J., Crowder, M. A., Zhan, C. & Hartzell, J. W. Bidirectional migration of Au colloids and silicon microrods in liquid using asymmetrical alternating current electric field with insulated electrodes. *Jpn. J. Appl. Phys.* **53**, 027301 (2014).
11. Hashemi, A., Bukosky, S. C., Rader, S. P., Ristenpart, W. D. & Miller, G. H. Oscillating electric fields in liquids create a long-range steady field. *Phys. Rev. Lett.* **121**, 185504 (2018).
12. Hashemi, A., Miller, G. H. & Ristenpart, W. D. Asymmetric rectified electric fields between parallel electrodes: numerical and scaling analyses. *Phys. Rev. E* **99**, 062603 (2019).
13. Bukosky, S. C., Hashemi, A., Rader, S. P., Mora, J., Miller, G. H. & Ristenpart, W. D. Extreme levitation of colloidal particles in response to oscillatory electric fields. *Langmuir* **35**, 6971–6980 (2019).
14. Prieve, D. C., Sides, P. J. & Wirth, C. L. 2-D assembly of colloidal particles on a planar electrode. *Curr. Opin. Colloid Interface Sci.* **15**, 160–174 (2010).
15. Hashemi, A., Tahernia, M., Hui, T. C., Ristenpart, W. D. & Miller, G. H. Net motion induced by nonantiperiodic vibratory or electrophoretic excitations with zero time average. *Phys. Rev. E* **105**, 065001 (2022).
16. Hashemi, A., Tahernia, M., Ristenpart, W. D. & Miller, G. H. Controlling the direction of steady electric fields in liquid using nonantiperiodic potentials. *Phys. Rev. E* **107**, 054608 (2023).

Chapter 5: Manipulation of dry granular materials using multimodal vibrations

This chapter shifts gears towards a different paradigm by studying multimodal vibratory forces on dry granular powders. The contents of this chapter are co-first authored with Xiaolin Zhang.

We present vibrational techniques to pump, mix, and separate dry granular materials using multifrequency vibrations applied to a solid substrate with a standard audio system. The direction and velocity of the granular flow are tuned by modulating the sign and amplitude, respectively, of the vibratory waveform, with typical pumping velocities of centimeters per second. This technique is amenable to handling multiple powders, where granular materials are mixed by combining them at Y-shaped junctions, and mixtures of granules with different friction coefficients are separated by judicious choice of the vibratory waveform. We demonstrate that the observed velocities accord with a theory valid for sufficiently large or fast vibrations, and we discuss the implications for using vibrational manipulation in conjunction with established microfluidic technologies to combine liquid and dry solid handling operations at submillimeter length scales.

5.1. Introduction

A variety of different microfluidic techniques[1–4] for precise handling of liquids currently exists for various analytic[5–7], synthetic[8–10], and diagnostic[11–15] laboratory tasks. Manipulation of dry solid powders, however, remain challenging for sub-millimeter scale devices, where applications in additive manufacturing and pharmaceutical dosing require precise handling[16]. For agglomeration-prone powders, a combination of electrostatic, cohesive, and packing properties can severely hamper consistent granular flowrates[17]. A pneumatic-assisted approach[18,19], achieved by temporarily fluidizing a bed of powder via pressurized gas flow, induces fluid-like properties to the solid bed to induce granular dispensing. Ultrasound mechanisms[20] are also widely employed in various configurations, serving a dual purpose of disrupting adhesive forces and releasing particles confined in a capillary tube by reducing frictional forces along the walls. Pipe vibrations using low frequency, axial vibration can induce net motion by pulsing a high frequency, radial vibration during backflow[21]. This method however is highly sensitive to the resonance frequency of the device, a common challenge for ultrasound-modulated methods. Critically, none of these processes provide the level of manipulation necessary for integration to lab-on-a-chip operations; gravity-assisted flow in vertically oriented tubes is not reversible, and continuous pumping around curved or otherwise complex geometries remains untested. Thus, to date no facile technology exists to manipulate dry granular materials with the precision or versatility expected of a lab-on-a-chip device.

In this chapter, we instead consider the effects of a dual-mode vibratory force, generally of the form

$$x(t) = A\sin(\omega t) + B\sin(\gamma\omega t + \phi). \tag{5.1}$$

Certain types of periodic functions are shift symmetric[22], also known as antiperiodic[23], which in simple terms means that the first half of the periodic waveform equals the negative of the second half. All single frequency sinusoidal waveforms have shift symmetry, because $\sin\left(\omega t + \frac{\pi}{2}\right) = -\sin(\omega t)$, but dual-frequency waveforms lack shift symmetry if the frequency mode ratio γ is not the ratio of two odd numbers[24]. For example, if $\gamma = 2$, then no choice of phase shift $t + \Delta t$ for the waveform in Eq. (5.1) recovers the negative of the waveform. This type of temporal symmetry breaking has long been recognized in the context of condensed matter physics[25–27], quantum mechanics[28,29], and nonlinear optics[30–32], where it is well established that driving forces that lack shift symmetry can induce a net current in one direction. Temporal symmetry breaking has also been recognized as a potential means of moving objects via frictional interactions on vibrating surfaces[33–36], with prior experimental demonstrations involving isolated objects like coins[37–39] or centimeter scale plastic rods[24]. Surprisingly, to date no literature exploits such temporal symmetry breaking to bulk granular media; the net response of a granular ensemble experiencing a multimodal vibrational force remains unknown.

Using a subwoofer device to drive a dual-mode vibration, we report sustained pumping of dry granular materials even around curves or junctions. Pumping was reversable by tuning the parameters in Eq. (5.1) and can reach velocities of centimeters per second. In the limit of large vibratory excitations, the direction and pump velocity were found to accord with analytic predictions. At lower excitation amplitudes, numerical predictions indicate that friction coefficients affect pumping velocities, which manifests as granular separation of mixtures. We also illustrate the versatility of this methodology via controlled mixing using geometries familiar to the lab-on-a-chip community. These findings provide methods to integrate dry material feeds into liquid streams for various lab-on-a-chip applications.

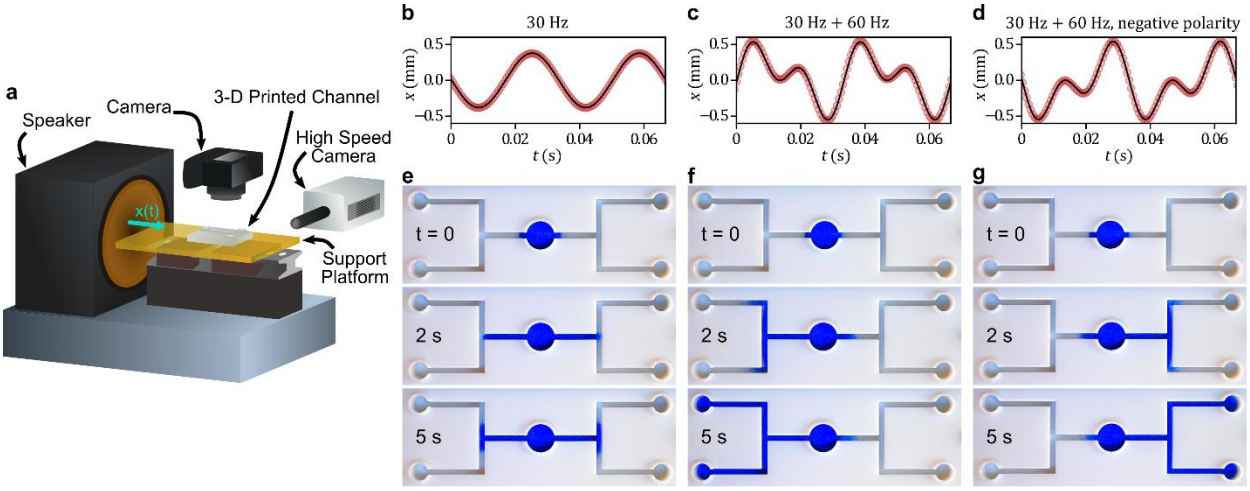

Figure 5.1. Vibrationally driven pumping of dry granular material. (a) *Schematic of the experimental apparatus. A 3-D printed lab-on-a-chip device is placed on a platform connected to a subwoofer.* ***(b – d)*** *Representative measurements of the vibratory motion of the lab-on-a chip device in response to various applied electrical signals to the subwoofer: (a), 30 Hz, (b) 30 Hz and 60 Hz, and (c) 30 Hz and 60 Hz with negative polarity. Red markers are experimental measurements acquired via high speed video of the horizontal substrate location relative to its original position, and the black curve is the best fit to Eq. (1) found via nonlinear regression.* ***(e – g)*** *Photographs of dry, blue-colored glass sand moving in response to the respective waveforms indicated above in (b – d), shown before application of the vibration (t =0, top row), after 2 s of vibration (middle row), and after 5 s of vibration (bottom row). Rectangular channels have width of 2 mm.*

5.2. Materials and methods

5.2.1 Speaker apparatus

Figure 5.1a depicts the experimental setup. The speaker was a Klipsch R-12SW subwoofer (400 watts, 41 cm x 10 cm x 47 cm), purchased commercially and used as received except that a circular piece of plywood was epoxied to the front diaphragm (12-cm diameter, 0.5 cm thick, depicted in Fig. 5.1a as light brown). A support platform was 3-D-printed using a Raise3D N2 printer, yielding a rectangular slab composed of polylactic acid (PLA) and with dimensions of 20 cm x 12 cm x 0.8 cm. This platform (depicted in yellow in Fig. 5.1a) was connected to the circular plywood surface using a 4 cm by 1.6 cm L-shaped metallic bracket. A stock 0.8 cm x 1.2 cm x 40

cm linear rail and two MGN12H steel carriages (Iverntech), typically used in 3-D printing equipment, were positioned underneath the platform to facilitate unidirectional motion (gray beam under the yellow platform in Fig. 5.1a). The entire apparatus was mounted on a 2.4 m by 1.2 m Newport optical breadboard table, with stacked 10 cm x 10 cm x 2.2 cm rubber/cork anti-vibration isolation pads (PneumaticPlus) placed underneath the subwoofer to minimize parasitic vibrations.

5.2.2 Lab-on-a-chip devices

All devices were fabricated using a Stratasys Polyjet printer (Objet 260 Connex) with Vero+ resin. Each device had overall dimensions of 12 cm x 3.8 cm x 0.8 cm, with two screw holes at either end to rigidly fasten the device to the support platform. Channels within the device were typically 2-mm in width and 5 mm deep. Circular entry or exit reservoirs typically had a raised edge that protruded 2 mm above the nominal top surface of the device to help prevent spillage. For some experiments, it was convenient to use a black device to maximize visual contrast with a white powder. These black devices were printed using a Formlabs Form 2 SLA printer with BioMed Black Formlabs resin, using identical geometry as the white devices.

5.2.3 Granular materials and test objects

The properties of the granular materials and test objects are summarized in the appendix supplementary table. The yeast was active dry baker's yeast (Red Star), purchased from a local grocery, and used as provided. The ibuprofen was generic 200-mg capsules purchased from a local vendor, which were ground into a fine powder using a pestle and mortar; the dark red capsule coating, once pulverized into the powder, provided convenient tracers within the otherwise uniformly white powder to help visualize the motion. The blue-colored silica sand was a recreational sand of the kind typically used decoratively in art projects, purchased from a local art supply store. The sand was filtered using a #140 wire cloth stainless steel mesh sieve to remove

larger agglomerates. Boron carbide powder (240 grit) was purchased from Advanced Abrasives and used as provided. Particle sizes were measured via optical microscopy and reported in the appendix. For the single object experiments (cf. Fig. 5.2b), 16-mm diameter annular stainless steel disks (Z9181-BEV type, plain steel) were purchased from McMaster Carr, and the lab-on-a-chip device was replaced with a 120 mm x 38 mm x 3.2 mm flat slab of aluminum (5052 aluminum bar).

5.2.4 Determination of friction coefficients

Granular media static friction coefficients were determined using two methods: angle of repose, and onset of sliding. We used a standard angle of repose method[40] in which a glass funnel was placed 10 cm over a 3.5 cm diameter metal cylinder. The granular material was poured through the funnel onto the metal surface to form a mound, and images of the side profile were taken using a DSLR camera. The static friction coefficient was calculated as the tangent of the angle of repose. For the sliding method, roughly 15 mg of the granular material was placed in the center of a 3-D printed channel. A manual micrometer was used to adjust the tilt of the channel until the powder exhibited downward sliding motion. The DSLR was then used to capture an image of the tilted channel to determine the static coefficient value from the tangent of the tilt angle. To gauge the friction coefficients of the stainless-steel disk on an aluminum substrate, a steel disk was placed on a horizontal aluminum slab and then covered with an extra 360 grams of weights to increase the normal force. A steel wire fastened to the weights was pulled horizontally by a linear actuator at a constant speed of 0.5 cm/s. A force meter (Vernier) with an accuracy of ±0.1 N recorded the force versus time. Following the standard analysis procedure[41], the static coefficient of friction was extracted from the peak force observed prior to onset of motion, and the kinetic coefficient of friction was extracted from the average pulling force after the disk overcame the static friction and

started sliding. The resulting static and kinetic coefficients for the steel disk on aluminum were 0.25 ± 0.03 and 0.17 ± 0.05 respectively, reflecting the mean and standard deviation of 3 replicate measurements.

5.2.5 Cleaning, leveling, and loading

All lab-on-a-chip devices were cleaned with isopropanol (IPA), rinsed with deionized water, and then air dried prior to each experiment. After attaching the lab-on-a-chip device to the platform, a bubble leveler was used to adjust the horizontal alignment. To further ensure the apparatus was level, prior to each round of experimentation a 16-mm steel disk was placed on top of the lab-on-a-chip device and a unimodal 30 Hz soundwave was applied; if the disk exhibited net drift in one direction, the tilt of the apparatus was corrected until no net drift was observed. To place a granular material into the device, a stopper (or two stoppers) made from transfer pipet tips were placed at the outlet(s) of the desired lab-on-a-chip reservoir to minimize premature spillage. A specified mass of a granular material (typically 50 mg) was then carefully poured into the reservoir, and the stoppers were then gently removed.

5.2.6 Sound files

A digital sound file controlling the electrical signal driving the motion of the diaphragm within the subwoofer was fed into the speaker to initiate each experiment. This sound file was created using custom python code from the scipy wavfile package, to yield waveforms of the kind described by Eq. (5.1). To minimize transient effects of the speaker upon application of the sound file, the amplitude of the waveform was increased linearly over 0.25 seconds up to the maximum prescribed amplitude; omitting this ramp-up typically caused the diaphragm and lab-on-a-chip device to “jerk” and fling granular materials into the air. Because the platform and lab-on-a-chip device put additional load and corresponding resistance to motion on the dynamic speaker, the

sound file waveform typically had a different ratio of amplitudes B/A and phase difference ϕ than was observed in the actual vibratory waveform (cf. Fig. 5.1b-d). All vibratory waveforms reported here are those observed experimentally by the high-speed camera.

5.2.7 Image capture

Two Genaray Spectro LED lights were placed over and behind the device, respectively, to provide lighting for two orthogonal cameras (cf. Fig. 5.1a). A Nikon Z 50 DSLR camera was positioned directly over the lab-on-a-chip device to image the granular motion. The image capture rate was chosen to precisely match the imposed vibrational frequency, so that the lab-on-a-chip device was imaged in the same location during its periodic motion (i.e., the substrate would appear stationary despite its vibratory motion). For the experiments reported here, the image capture rate was typically 30 or 50 frames per second (fps) to accord with the 30 Hz or 50 Hz vibratory waveforms imposed on the device. A Phantom V311 high speed camera acquiring images at 1600 fps was positioned orthogonally to the platform, to track the horizontal motion $x(t)$ of a small vertical post attached to the lab-on-a-chip device to serve as a fiducial. The DSLR camera recorded the granular motion from above over the duration of each experiment. The high-speed camera recorded up to 2 seconds of the fiducial motion, corresponding to 60 or 100 cycles of the oscillatory motion for 30 or 50 Hz respectively. The early ramp-up period (cf. Sound File, above) was excluded from the high-speed video measurements.

5.2.8 Image and data analysis

All image analysis was performed using standard techniques with the OpenCV package in python. A global threshold was applied to each image to convert it to binary and detect the extent of the granular material. The front location $p(t)$ was defined as the leading edge of the largest contiguous detected object within the channel. Accordingly, individual outlier granules moving

slightly faster than average but not in apparent contact with the bulk of the granular fluid did not affect $p(t)$. A recurring feature of the data is that the granular materials exhibited a transient acceleration before reaching a steady velocity (see representative trajectory in Appendix Fig. S2). To exclude the transient, the acceleration profile d^2p/dt^2 was determined by central finite approximation of the position data and then smoothed using a uniform 10-point running average as a smoothing filter. The onset of the steady velocity dp/dt was assessed using linear regression starting at the time point when the granular fluid front acceleration reached zero, i.e., $d^2p/dt^2 = 0$. In the case of single object motion, the centroid of the disk was tracked instead; all subsequent data analysis was performed in a similar fashion. The high-speed videos of the fiducial motion were also analyzed using OpenCV to track the fiducial centroid $x(t)$ vs. time. The vertical displacement of the fiducial was less than one pixel, indicating that the maximum vertical component of the vibration conservatively was less than 29 microns. The parameters A, B, ϕ for the horizontal vibratory waveform (cf. Eq. (5.1)) were found via nonlinear regression using minimized least squares. The parameters γ and ω were verified via Fourier analysis to confirm that the peak amplitudes were at the desired ω and $\gamma\omega$ modes. Experiments were performed in triplicate for each material type and each applied waveform, with all three measured velocities for each condition presented in Figure 5.2b.

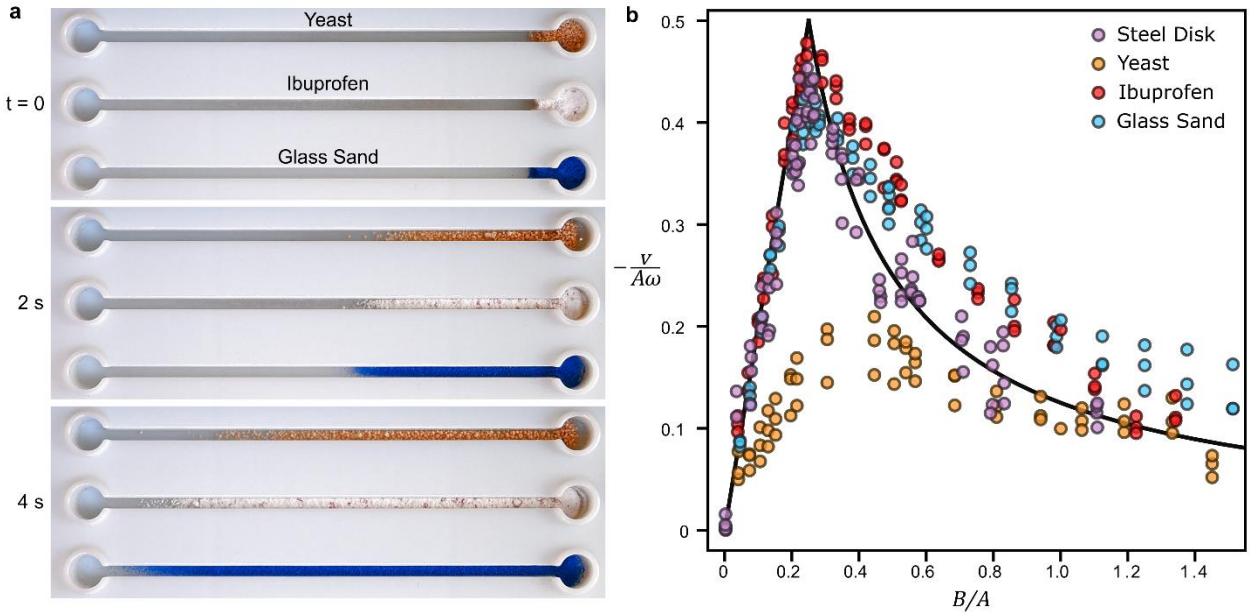

Figure 5.2. Velocity of different materials versus vibration amplitude. (a) *Representative images of dry granular materials (yeast agglomerates, crushed ibuprofen powder, and blue-colored silica sand) moving in separate parallel channels in response to a 30 Hz and 60 Hz vibration, shown before application of the vibration (t =0, top image), after 2 s of vibration (middle image), and after 4 s of vibration (bottom image). Each channel is 2 mm wide; amplitude ratio is* $B/A = 1$. *See also Supplementary Video 4.* ***(b)*** *The dimensionless velocity versus the amplitude ratio* B/A. *Markers represent experimental measurements for granular materials (yeast, ibuprofen, and sand are yellow, red, and cyan markers, respectively) moving in channels as shown in (a). Purple markers denote the velocity of individual 16-mm steel disks moving on a flat aluminum substrate. Black curve is the high-Friction number theoretical prediction given by Eq. (5.6) with* $\phi = 0$*; see Supplementary Fig. S1 for velocity measurements versus* ϕ.

5.3. Results and discussion

5.3.1 Tunable pumping

The controlled motion of granular materials in millimeter-scale channels is readily demonstrated with a consumer-grade audio system (Fig. 5.1a). A 3-D-printed lab-on-a-chip device is fastened to a platform that is directly connected to the front diaphragm of a standard subwoofer, the type of dynamic loudspeaker typically used to create bass soundwaves between 20 to 200 Hz. When activated the subwoofer emits an audible noise, but more importantly the movement of the

diaphragm causes the platform and attached lab-on-a-chip device to vibrate back and forth horizontally, with frequency and amplitude defined by the electrical audio signal sent to the subwoofer.

The resulting motion of granular materials placed in the lab-on-a-chip device depends sensitively on the properties of the electrical audio signal (Fig. 5.1b-g). Application of a single frequency waveform at 30 Hz (Fig. 5.1b) causes the particles to slowly drift in both directions away from their initial position in a central loading port (Fig. 5.1e). This slow and symmetric drift is consistent with prior work examining the behavior of granular materials in response to horizontal vibrations[42,43]; the particles are fluidized by the vibration and migrate along the direction of the vibration with zero net displacement of the center of mass. Qualitatively different behavior occurs, however, when certain types of dual-frequency waveforms are applied to the device. Here, application of a vibratory waveform with both 30 Hz and 60 Hz frequencies (Fig. 5.1c) causes the particles to rapidly pump to the left with a velocity of about – 2 cm/s (Fig. 5.1f). Almost no rightward drift out of the central port is observed, and the particles readily flow past a T-junction obstacle. The pumping continues until the central port empties and the particulates accumulate in the two separate exit ports. Importantly, the direction of the flow is reversed simply by applying the negative of the electrical dual-frequency audio signal (Fig. 5.1d). We emphasize that all other conditions here are identical, with the same type of particles placed in the same starting point in the same device. Application of the negative waveform causes the particles to immediately pump to the right, with little evident leftward drift, and with equal but opposite velocity of +2 cm/s (Fig. 5.2g). Repeated trials show that the direction of motion is always the same for a given polarity of the dual-frequency waveform, i.e., the direction is deterministic, not stochastic. Experiments with a variety of other dry granular materials – including brewer's yeast, crushed ibuprofen powder,

boron carbide granules, sodium chloride, baking soda, and soluble coffee grounds – all show that the reversible-direction pumping behavior is quite general (cf. Fig. 5.2a).

5.3.2 Theoretical asymptotic velocity

Why would a dual-frequency vibration cause the particles to pump in one direction? We interpret the observations in terms of a temporal symmetry breaking in the frictional driving force, and we also derive a concise analytical prediction for the velocity. In brief, by application of Newton's second law, the velocity $v(t)$ of an individual granule of mass m experiencing a frictional force with a substrate vibrating with a waveform specified by Eq. (5.1) must satisfy

$$m\frac{dv}{dt} = \mu mg \,\text{sign}[x'(t) - v(t)]. \tag{5.2}$$

Here μ is the coefficient of friction, g is the gravitational acceleration, and $x'(t)$ is the velocity of the vibrating substrate (i.e., the time derivative of Eq. (5.1)). The sign function is $+1$ if the velocity difference is positive, -1 if it is negative, and 0 if they are the same; physically this function describes how the frictional force causes the object to speed up (slow down) if the substrate is moving faster (slower) than the object. Because of the sign function, Eq. (5.2) is nonlinear and difficult to solve in general. To simplify the problem, we ignore the complicated particle-particle interactions in a moving granular fluid and focus instead on the behavior of an isolated particle placed on a substrate vibrating with waveform given by Eq. (5.1). We also assume that the only force acting on the particle is the frictional interaction with the substrate, and we specify the dimensionless quantities $\hat{v} = v/(A\omega)$, $\hat{t} = t\omega$, and $\hat{x} = x/A$. Rearrangement of Newton's second law (cf. Eq. (5.2)) yields[24,37]

$$\frac{d\hat{v}}{d\hat{t}} = \begin{cases} \hat{x}''(\hat{t}), & \text{if } \hat{v} = \hat{x}'(\hat{t}) \text{ and } |\hat{x}''(\hat{t})| \le \text{Fr}^{-1} \\ \frac{\mu_k}{\mu_s \text{Fr}} \,\text{sign}[\hat{x}'(\hat{t}) - \hat{v}(\hat{t})], & \text{otherwise.} \end{cases} \tag{5.3}$$

Here $\frac{\mu_k}{\mu_s}$ is the ratio of kinetic and static coefficients of friction, respectively, and the Friction number $\mathrm{Fr} = \frac{A\omega^2}{\mu_s g}$ represents the relative magnitudes of the driving and frictional forces acting on the particle. We initially restrict attention to fast and large vibrations such that the acceleration of the substrate always exceeds the static coefficient of friction necessary for slip between the particle and substrate, i.e., $|\hat{x}''(\hat{t})| > \mathrm{Fr}^{-1}$ for all $\hat{t}$. If this condition is satisfied, then we avoid situations where the particle becomes "stuck" to the substrate during some part of the vibratory waveform.

We separate $\hat{v}$ into its steady component and oscillatory component, $\hat{v}(\hat{t}) = \hat{v}_{st} + \hat{v}_{osc}(\hat{t})$, yielding

$$\frac{d\hat{v}_{osc}}{d\hat{t}} = \frac{1}{\mathrm{Fr}} \operatorname{sign}[\hat{x}'(\hat{t}) - \hat{v}_{st} - \hat{v}_{osc}(\hat{t})]. \tag{5.4}$$

The oscillatory component of the dimensionless velocity therefore varies linearly with time and has slope equal to $\pm\mathrm{Fr}^{-1}$, with the sign function determining whether the slope is positive or negative at any particular time. Integration of Eq. (5.4) with respect to time over the vibratory waveform period T yields zero on the left-hand-side, and in the limit of asymptotically large Friction numbers the oscillatory component $\hat{v}_{osc} \sim \mathrm{Fr}^{-1}$ must also vanish, yielding the expression

$$0 = \int_0^T \operatorname{sign}[\hat{x}'(t) - \hat{v}_{st}]d\hat{t}, \tag{5.5}$$

which has the desired steady velocity $\hat{v}_{st}$ as the only unknown. Notably, in this limit all dependence on Fr has been removed, meaning that the friction coefficient does not affect the velocity in the limit of sufficiently large and fast vibrations. Solving for $\hat{v}_{st}$ thus becomes an exercise in finding the roots of $\hat{x}'(t) - \hat{v}_{st}$ such that the time integral is satisfied; in simpler terms, over one period the quantity $\hat{x}'(t) - \hat{v}_{st}$ must be cumulatively positive over half of the period and

cumulatively negative over the other half, such that the signed sum of the durations of each vibratory period spent at positive or negative values is identically zero. Reznik and Canny[37] used analogous arguments to hypothesize a similar result to Eq. (5.6) for $\phi = 0$. Thus, in the limit $\mathrm{Fr} \gg 1$ and for the specific case $\gamma = 2$, the predicted steady velocity is

$$\frac{v}{A\omega} = \begin{cases} -\frac{2B}{A}\cos\phi, & \left|\frac{B}{A}\right| \leq \frac{1}{4} \\ -\frac{A}{8B}\cos\phi, & \left|\frac{B}{A}\right| > \frac{1}{4} \end{cases} \tag{5.6}$$

where A and B are the amplitudes of the two frequency components, respectively, and ϕ is the relative phase lag between the two frequency modes (cf. Eq. (5.1)). A more detailed analysis of Eq. (5.5) and mathematical proofs of Eq. (5.6) are provided elsewhere (X.Z., T.H., W.R., & G.M., unpublished work).

A surprising aspect of this prediction is that the velocity is completely independent of the frictional properties of the granule and the substrate, at least in the limit of sufficiently large or fast vibrations, despite the motion being driven entirely by that frictional interaction. Our experimental observations nonetheless strongly accord with this prediction (Fig. 5.2b). The velocity of individual centimeter-scale steel disks follows the theoretical prediction almost exactly (purple circles) with peak velocities near $\frac{B}{A} = 0.25$. Additional experiments with steel disks further show that the velocity varies as $\cos\phi$, in accord with the prediction. Representative granular media, including sand and crushed ibuprofen powder (blue and red circles in Fig. 5.2b) likewise follow the theoretical prediction closely. Yeast particles (yellow circles) also generally follow the

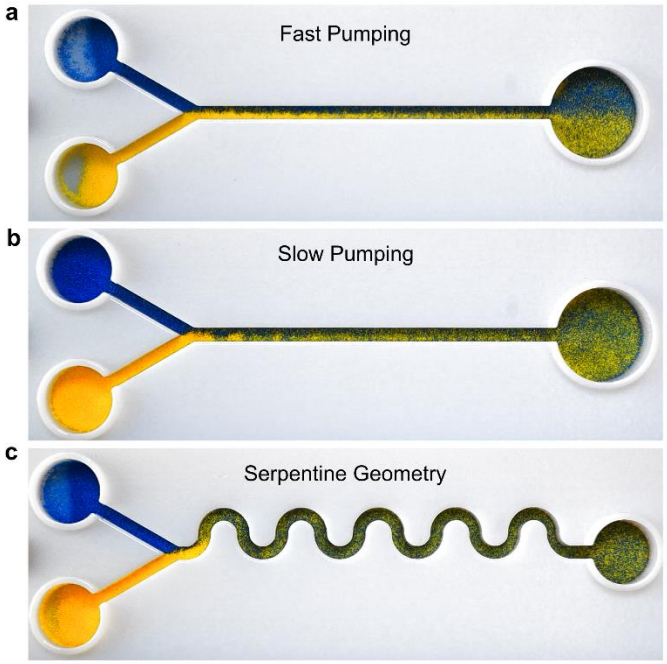

Figure 5.3. Vibrationally driven mixing of dry granular materials. *Representative images of blue- and yellow- colored silica sands, initially placed in separate circular ports at left, after several seconds of vibrational pumping from left to right through a Y-junction.* ***(a)*** *Relatively fast pumping using* $B/A = 0.23$. ***(b)*** *Relatively slow pumping using* $B/A = 0.06$. ***(c)*** *Fast pumping using same vibration as in (a) but in a channel with serpentine geometry. Channel width in each is 2 mm; applied frequencies are 30 and 60 Hz in (a) and (c), and 50 and 100 Hz in (b), all negative polarity.*

predicted trend, albeit with maximum values approximately half as large as predicted. This overprediction of the observed velocity for the yeast likely stems from the neglect of vertical motion due to particle collisions; the yeast particles are less dense and tend to bounce off the substrate or other particles and travel momentarily through the air, thus violating the assumption of continuous frictional interaction with the vibrating substrate. Despite this complication, net motion of the predicted magnitude is observed, and the denser granular materials exhibit similar velocities despite differences in their frictional properties (cf. Appendix Table).

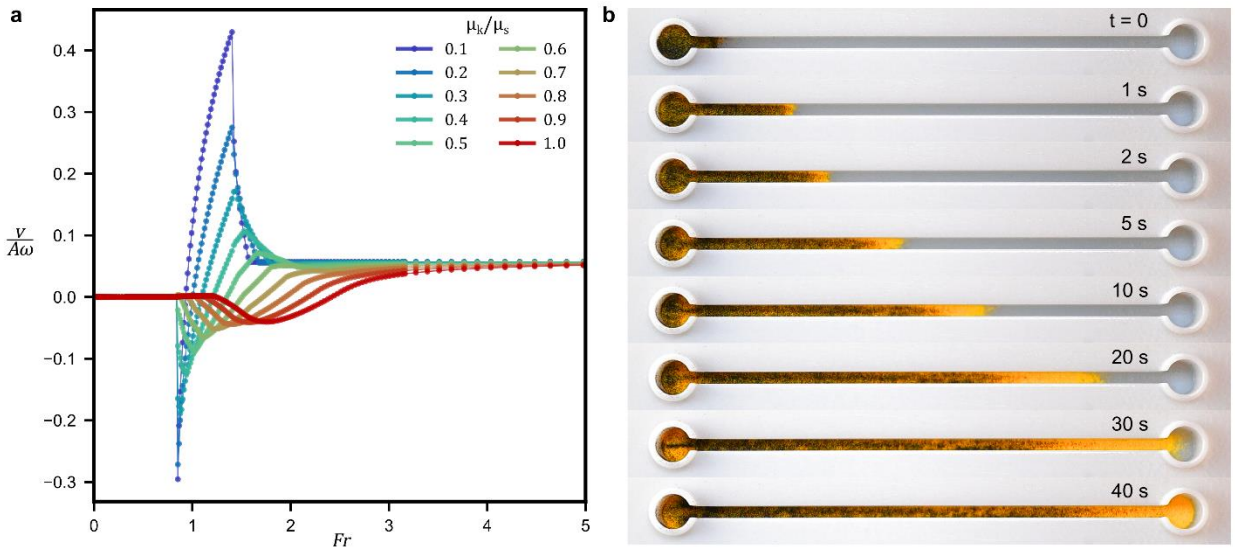

Figure 5.4. Vibrational separation of a dry granular mixture. (a) *Numerical simulations of the dimensionless velocity in response to a vibration with $\gamma = 3/2$ and $B/A = 1$ for various ratios of the kinetic and static coefficient of friction, μ_k/μ_s.* ***(b)*** *Time lapse images of a mixture of silica glass sand (yellow) and boron carbide powder (black), moving in response to a vibration with 50 Hz and 75 Hz frequency modes ($\gamma = 3/2$) and $B/A = 0.13$. Channel width is 2 mm.*

5.3.3 Mixing and separation granular materials

The ability to pump granular materials in a desired speed and direction enables a variety of "vibrofluidic" operations for lab-on-a-chip devices. For example, different granular materials are readily brought together at Y-junctions for mixing operations (Fig. 5.3). At higher velocities (Fig. 5.3a), powders that converge into a straight channel exhibit little cross-stream mixing as they move downstream, remaining mostly segregated as they flow into the exit port; the behavior is qualitatively similar to the behavior of liquids at Y-junctions in microfluidic devices, where cross-stream mixing is governed by a balance between convective and diffusive forces[1]. At lower velocities, the powders exhibit more cross-stream mixing (Fig. 5.3b) and are more mixed at the exit port, reflecting the increased amount of time available for cross-stream diffusion at a lower downstream velocity. To achieve both high speed and high mixing, the device geometry can be

modified to include a serpentine geometry following the Y-junction (Fig. 5.3c). The powders are well-mixed after only a couple S-turns, and appear perfectly mixed when they reach the exit port. Similar serpentine geometries have been heavily explored in the context of microfluidic mixing[44], where it was shown that small but non-zero amounts of transverse momentum within the fluid contribute to chaotic advection and consequent mixing[1]. The behavior illustrated in Fig. 5.3c indicates that analogous effects also occur with granular fluids, and further establishes that powders can be readily mixed on demand at small length scales.

Another important operation for granular mixtures is separation. The pumping and mixing demonstrated in Figs. 5.1 through 5.3 all pertained in the high Friction number limit, where the vibratory driving force dominates over frictional effects and the velocity is predicted to be independent of the frictional properties of the granules and substrate. Our numerical calculations indicate that the granule velocity is much more sensitive to the frictional properties for vibrations near Fr ≈ 1 (Fig. 5.4a). At very low Friction numbers the average velocity is zero, since the vibration is too weak to cause the granules to displace with respect to the substrate, while at high Friction numbers the velocity asymptotically approaches a constant value independent of the Friction number, qualitatively consistent with Eq. (5.6). At intermediate Friction numbers, the steady velocity is predicted to be highly sensitive to the ratio of the kinetic and static friction coefficients, $\mu_R = \frac{\mu_k}{\mu_s}$. For vibratory waveforms with $\gamma = \frac{3}{2}$, there are rapid changes in both the amplitude and the direction of the predicted velocity over a very small range in Fr, which means that granules with different frictional properties will move at different velocities in response to the same applied waveform. A key practical consequence of this friction coefficient dependence is that mixtures of granules in theory can be separated using an appropriate vibratory waveform. Indeed, our experimental tests confirm that a vibratory waveform with $\gamma = \frac{3}{2}$ causes mixtures of

granules to separate when they are vibrationally pumped along a straight channel (Fig. 5.4b). Here, two different granular powders (yellow and black) with similar granular sizes are well mixed and placed in an entry port. Application of the vibratory waveform causes them to move rightward and to clearly separate into yellow-rich powder at the leading edge and black-rich powder at the rear. There are well-established methods for separating granular materials based on their size or density[45], but to our knowledge there are no techniques to separate granules based on their frictional properties, nor any techniques to separate them using devices measured in millimeters. More detailed theoretical analyses that account for particle-particle interactions are needed to predict the frictional separation efficiency, but the results in Fig. 5.4 provide a clear proof of principle that mixtures of granular materials can be separated at the small lengths scales needed for lab-on-a-chip applications.

5.4. Conclusions

The above results suggest how liquid and dry handling operations may be combined within one device to achieve the vision of a truly miniaturized laboratory. For example, a ubiquitous laboratory operation involves scooping out a specific mass of a dry powder and placing it into a known mass of liquid to yield a desired solute concentration. To date, such solutions must be prepared by hand prior to insertion into a lab-on-a-chip device, but the vibrational technique established here provides the opportunity to pump desired quantities of a dry granular material into a specific reservoir on a chip, followed by insertion of liquid and dissolution of the granules. Likewise, liquids with mixtures of solutes could potentially be evaporated to leave behind precipitates or crystallized dry materials, which could then be vibrationally pumped out and possibly separated into different material streams. Potential challenges to this vision involve compaction[46] and cohesive interactions[47], which are both known to strongly impact the behavior

of granular fluids. These complicating effects have not yet been studied in the context of fluidization by horizontal and temporally asymmetric vibrations, so much remains to be investigated regarding how best to control different types of granular motion in lab-on-chip devices.

As a final comment, we note that the underlying physics established here pertain to a large range of length scales and orientations. The predicted velocity of an individual object on the vibrating surface is independent of its mass because both terms in the force balance are proportional to it (cf. Eq. (5.2)). A significant implication is that arbitrarily large collections of objects can be manipulated simply by vibrating the underlying substrate, provided that enough power is available to move both the substrate and the mass resting on it. The pumping, mixing, and separating demonstrated here at small length scales potentially could be applied to larger collections of objects, including agricultural products like fruits or grains[48], mining products like ores or minerals[49], and recyclable materials like scrap metals or plastics[50]. Similarly, the underlying physics do not mandate that the bottom surface must vibrate while an object on top moves passively in response; our theory suggests that an active object made to vibrate with two non-antiperiodic frequency modes will translate along a stationary substrate, raising the possibility of autonomous robots and other devices using vibrations as a source of locomotion. The results presented here provide a foundation for considering these more complicated applications.

5.5 References

1. Stone, H. A., Stroock, A. D. & Ajdari, A. Engineering flows in small devices: microfluidics toward a Lab-on-a-Chip. *Annu. Rev. Fluid Mech.* **36**, 381–411 (2004).

2. Whitesides, G. M. The origins and the future of microfluidics. *Nature* **442**, 368–373 (2006).

3. Teh, S.-Y., Lin, R., Hung, L.-H. & Lee, A. P. Droplet microfluidics. *Lab. Chip* **8**, 198–220 (2008).

4. Convery, N. & Gadegaard, N. 30 years of microfluidics. *Micro Nano Eng.* **2**, 76–91 (2019).

5. Dalili, A., Samiei, E. & Hoorfar, M. A review of sorting, separation and isolation of cells and microbeads for biomedical applications: microfluidic approaches. *Analyst* **144**, 87–113 (2018).

6. Cui, P. & Wang, S. Application of microfluidic chip technology in pharmaceutical analysis: a review. *J. Pharm. Anal.* **9**, 238–247 (2019).

7. Wongkaew, N., Simsek, M., Griesche, C. & Baeumner, A. J. Functional nanomaterials and nanostructures enhancing electrochemical biosensors and Lab-on-a-Chip performances: recent progress, applications, and future perspective. *Chem. Rev.* **119**, 120–194 (2019).

8. Günther, A. & Jensen, K. F. Multiphase microfluidics: from flow characteristics to chemical and materials synthesis. *Lab. Chip* **6**, 1487–1503 (2006).

9. Hartman, R. L. & Jensen, K. F. Microchemical systems for continuous-flow synthesis. *Lab. Chip* **9**, 2495–2507 (2009).

10. Shestopalov, I., Tice, J. D. & Ismagilov, R. F. Multi-step synthesis of nanoparticles performed on millisecond time scale in a microfluidic droplet-based system. *Lab. Chip* **4**, 316–321 (2004).

11. Yager, P. *et al.* Microfluidic diagnostic technologies for global public health. *Nature* **442**, 412–418 (2006).

12. Sackmann, E. K., Fulton, A. L. & Beebe, D. J. The present and future role of microfluidics in biomedical research. *Nature* **507**, 181–189 (2014).

13. Chin, C. D., Linder, V. & Sia, S. K. Commercialization of microfluidic point-of-care diagnostic devices. *Lab. Chip* **12**, 2118–2134 (2012).

14. Yetisen, A. K., Akram, M. S. & Lowe, C. R. Paper-based microfluidic point-of-care diagnostic devices. *Lab. Chip* **13**, 2210–2251 (2013).

15. Wang, C. *et al.* Point-of-care diagnostics for infectious diseases: from methods to devices. *Nano Today* **37**, 101092 (2021).

16. Yang, S. & Evans, J. R. G. Metering and dispensing of powder; the quest for new solid freeforming techniques. *Powder Technol.* **178**, 56–72 (2007).

17. Fathollahi, S., Sacher, S., Escotet-Espinoza, M. S., DiNunzio, J. & Khinast, J. G. Performance Evaluation of a High-Precision Low-Dose Powder Feeder. *AAPS PharmSciTech* **21**, 301 (2020).

18. Vilkner, T., Shivji, A. & Manz, A. Dry powder injection on chip. *Lab. Chip* **5**, 140–145 (2005).

19. Yuan, Y., Yu, K., Zhu, H. & Ehmann, K. F. Continuous feeding of powders with vibration and pneumatic pressure assistance for laser-based additive manufacturing processes. *J. Manuf. Process.* **82**, 336–346 (2022).

20. Lu, X., Yang, S. & Evans, J. R. G. Ultrasound-assisted microfeeding of fine powders. *Particuology* **6**, 2–8 (2008).

21. Dunst, P., Hemsel, T. & Sextro, W. Analysis of pipe vibration in an ultrasonic powder transportation system. *Sens. Actuators Phys.* **263**, 733–736 (2017).

22. Denisov, S., Flach, S. & Hänggi, P. Tunable transport with broken space–time symmetries. *Phys. Rep.* **538**, 77–120 (2014).

23. Freire, J. G., Cabeza, C., Marti, A., Pöschel, T. & Gallas, J. A. C. Antiperiodic oscillations. *Sci. Rep.* **3**, 1958 (2013).

24. Hashemi, A., Tahernia, M., Hui, T. C., Ristenpart, W. D. & Miller, G. H. Net motion induced by nonantiperiodic vibratory or electrophoretic excitations with zero time average. *Phys. Rev. E* **105**, 065001 (2022).

25. Flach, S., Yevtushenko, O. & Zolotaryuk, Y. Directed Current due to Broken Time-Space Symmetry. *Phys. Rev. Lett.* **84**, 2358–2361 (2000).

26. Denisov, S., Flach, S., Ovchinnikov, A. A., Yevtushenko, O. & Zolotaryuk, Y. Broken space-time symmetries and mechanisms of rectification of ac fields by nonlinear (non)adiabatic response. *Phys. Rev. E* **66**, 041104 (2002).

27. Ustinov, A. V., Coqui, C., Kemp, A., Zolotaryuk, Y. & Salerno, M. Ratchetlike dynamics of fluxons in annular Josephson junctions driven by biharmonic microwave fields. *Phys. Rev. Lett.* **93**, 087001 (2004).

28. Denisov, S., Morales-Molina, L., Flach, S. & Hänggi, P. Periodically driven quantum ratchets: symmetries and resonances. *Phys. Rev. A* **75**, 063424 (2007).

29. Denisov, S., Morales-Molina, L. & Flach, S. Quantum resonances and rectification in ac-driven ratchets. *Europhys. Lett.* **79**, 10007 (2007).

30. Schiavoni, M., Sanchez-Palencia, L., Renzoni, F. & Grynberg, G. Phase Control of Directed Diffusion in a Symmetric Optical Lattice. *Phys. Rev. Lett.* **90**, 094101 (2003).

31. Gommers, R., Denisov, S. & Renzoni, F. Quasiperiodically Driven Ratchets for Cold Atoms. *Phys. Rev. Lett.* **96**, 240604 (2006).

32. Eckardt, A. Colloquium: atomic quantum gases in periodically driven optical lattices. *Rev. Mod. Phys.* **89**, 011004 (2017).

33. Reznik, D. & Canny, J. A flat rigid plate is a universal planar manipulator. in *Proceedings. 1998 IEEE International Conference on Robotics and Automation (Cat. No.98CH36146)* vol. 2 1471–1477 vol.2 (1998).

34. Fleishman, D., Asscher, Y. & Urbakh, M. Directed transport induced by asymmetric surface vibrations: making use of friction. *J. Phys. Condens. Matter* **19**, 096004 (2007).

35. Viswarupachari, Ch., DasGupta, A. & Pratik Khastgir, S. Vibration Induced Directed Transport of Particles. *J. Vib. Acoust.* **134**, (2012).

36. Nath, J., Das, S., Vishwakarma, A. & DasGupta, A. Directed transport of a particle on a horizontal surface under asymmetric vibrations. *Phys. Nonlinear Phenom.* **440**, 133452 (2022).

37. Reznik, D. & Canny, J. The Coulomb pump: a novel parts feeding method using a horizontally-vibrating surface. in *Proceedings. 1998 IEEE International Conference on Robotics and Automation (Cat. No.98CH36146)* vol. 1 869–874 vol.1 (1998).

38. Buguin, A., Brochard, F. & de Gennes, P.-G. Motions induced by asymmetric vibrations. *Eur. Phys. J. E* **19**, 31–36 (2006).

39. Umbanhowar, P. & Lynch, K. M. Optimal vibratory stick-slip transport. *IEEE Trans. Autom. Sci. Eng.* **5**, 537–544 (2008).

40. Beakawi Al-Hashemi, H. M. & Baghabra Al-Amoudi, O. S. A review on the angle of repose of granular materials. *Powder Technol.* **330**, 397–417 (2018).

41. Persson, B. N. J. *Sliding Friction*. (Springer, 2000).

42. Sánchez, I. *et al.* Spreading of a granular droplet. *Phys. Rev. E* **76**, 060301 (2007).

43. Khefif, S. M., Valance, A. & Ould-Kaddour, F. Spreading of a granular droplet under horizontal vibrations. *Phys. Rev. E* **97**, 062903 (2018).

44. Raza, W., Hossain, S. & Kim, K.-Y. A review of passive micromixers with a comparative analysis. *Micromachines* **11**, 455 (2020).

45. Kudrolli, A. Size separation in vibrated granular matter. *Rep. Prog. Phys.* **67**, 209 (2004).

46. Richard, P., Nicodemi, M., Delannay, R., Ribière, P. & Bideau, D. Slow relaxation and compaction of granular systems. *Nat. Mater.* **4**, 121–128 (2005).

47. Castellanos, A. The relationship between attractive interparticle forces and bulk behaviour in dry and uncharged fine powders. *Adv. Phys.* **54**, 263–376 (2005).

48. Pearson, T. C. High-speed sorting of grains by color and surface texture. *Appl. Eng. Agric.* **26**, (2010).

49. Luo, X., He, K., Zhang, Y., He, P. & Zhang, Y. A review of intelligent ore sorting technology and equipment development. *Int. J. Miner. Metall. Mater.* **29**, 1647–1655 (2022).

50. Wu, G., Li, J. & Xu, Z. Triboelectrostatic separation for granular plastic waste recycling: a review. *Waste Manag.* **33**, 585–597 (2013).

Chapter 6: Summary and outlook

6.1 Summary of main conclusions

This dissertation studies nonlinear dynamics of sinusoidal forces via an electrokinetic system and a dry solid-solid friction "vibrofluidic" system. These studies illustrate symmetry-breaking effects that suggest new avenues of particle transport from time-averaged zero forces.

In a colloidal suspension, a unimodal potential causes particles near an electrode to either separation or aggregate, depending on the electrolyte. A scaling analysis comparing AREF to EHD forces indicates that AREF can yield comparable hydrodynamic flows to EHD flow. Competition between an AREF-induced flow on the particle surface and an EHD flow on the electrode surface provide new insight on how the electrolyte mobility mismatch can either enhance or diminish the aggregation rate.

Between two planar electrodes, AREF predictions indicate a long-range steady field. Partial visualization of this field distribution was performed by a microchannel constructed with two thin conductive metal sheets. Under unimodal polarization, depletion zones form away from the electrodes. These depletion zones were found to match predictions due to an AREF electrophoresis and an AREF-induced background flow along the channel walls. For a multimodal potential, the resulting field becomes more complex; however, the experiments performed illustrate bulk particle depletion which was reversible by inverting the polarization.

In a friction-based system, where dry materials experience multimodal friction excitation from a vibrating platform, powders were found to pump at steady velocities at rates of centimeters per second. Further, powders can be mixed by using conventional channel geometries typical of a lab-on-a-chip device, or separated by operating at a low to moderate

excitation strength. Importantly, the friction number Fr and amplitude ratio β were found to be key parameters in tuning and modulating granular behaviors, with an asymptotic velocity at high Fr similar to predictions found for an isolated object undergoing nonantiperiodic multimodal vibration. The following sub-sections detail theoretical and experimental concepts that will be of relevance towards future studies.

6.2 Flow field around a particle near an electrode under oscillatory polarization

Hashemi et al. constructed representative flow fields around a particle due to an EHD flow induced along the electrode surface and a steady AREF electroosmotic flow along the particle surface. For simplicity, they assume a constant AREF strength, evaluated at the particle center, and use a biharmonic solution employed by Solomentsev for the electroosmotic flow field. For practical particles of roughly 0.1-10 μm, however, AREF will vary tremendously and possibly change signs across the particle surface. A new approach is necessary to account for the spatial dependency of AREF (cf. Fig. 6.1). One method is to modify the electroosmotic flow field prediction by directly implementing either the semi-analytic AREF distribution from Hashemi et al. or the analytic expression by Balu and Khair at the low potential limit into the boundary conditions. Superposition of the proposed flow field with the EHD flow field would result in new predictions that have not been reported. Resolving a reasonable quantity of coefficients for the biharmonic expression may be challenging; other numerical schemes may be necessary.

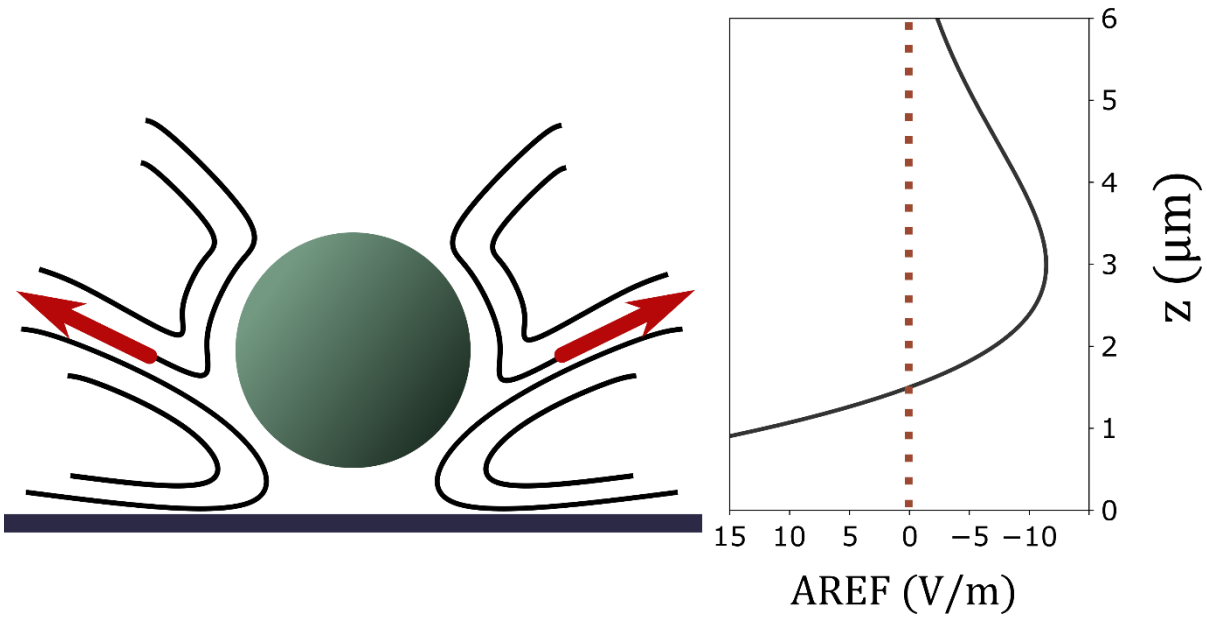

Figure 6.1. *Cartoon streamlines around a particle solely due to electroosmosis caused by an example AREF distribution shown on the right.*

Another puzzling aspect is the location of the particle. The aforementioned model only considers the rectified components of the flow; no time-dependent or oscillatory components are considered. Nonetheless, a whole suite of studies was conducted comparing the phase lag of the electric field and the particle vertical oscillations. A starting point for validating theoretical predictions while circumventing time-dependent effects is to fix a dielectric cylinder over a polarized electrode, which eliminates the oscillatory motion of the "particle". Tracer particles and particle image velocimetry can then be used to estimate flow fields around the cylinder, which may provide reasonable comparisons to predictions from a 2-D theoretical construct. Details of such an experimental apparatus is provided in the following section. Varying the position of the dielectric cylinder thus serves as a direct probe towards the AREF spatial influence on the flow field.

6.3 Fabrication of microfluidic device with vertical conducting walls

Previous work on the microchannel in chapter 3 provides experimental visualization of the colloidal suspension behavior under AC polarization. Although the fabrication is cheap and accessible, several parameters of the geometry are not easily controlled. The electrode gap can vary hundreds of microns between devices, and the devices tend to leak over time, partially due to poor sealing of the glass substrate and metal sheets. A natural choice would be to fabricate two vertical planar electrodes in a straight channel using photolithography methods from a cleanroom setting. Typical microfluidic devices layer conductive patterns using a mask, apply metal deposition, and etch; however, in this case the conductive material needs to be fully planar along the channel walls. Precise control over the photoresist mask depth and proper exposure time is necessary to prevent under or over etching of the metal. In collaboration with Dr. Jiandi Wan's research group, the following procedure was created.

1. Etch a 100 μm x 1 cm x 10 μm (W x L x H) straight channel into the silicon (Si) wafer.
2. Coat the Si wafer with SiO2, roughly 100 nm, which serves to insulate the wafer.
3. Deposit 50 nm titanium (Ti) followed by 200 nm (Au) using e-beam deposition. For uniform coating of the vertical walls, a planetary dome configuration (for a device such as the CHA E-Beam Evaporator in CNM2) may be necessary.
4. Spincoat roughly 10 μm of NR78-8000P (1200 rpm for 40s), then softbake at 120°C for 2.5 min. Expose, then postbake at 110°C for 3 min.
5. Develop the NR78 photoresist using Futurrex RD6 by immersion.
6. Etch the Au layer using gold etchant (typically KI solution). Then etch the Ti layer using 2 mL of 49% hydrofluoric acid diluted to 400 mL stock volume.

7. Remove the remaining NR-78 mask with Futurrex RR41 via immersion and rinse thoroughly prior to dicing.

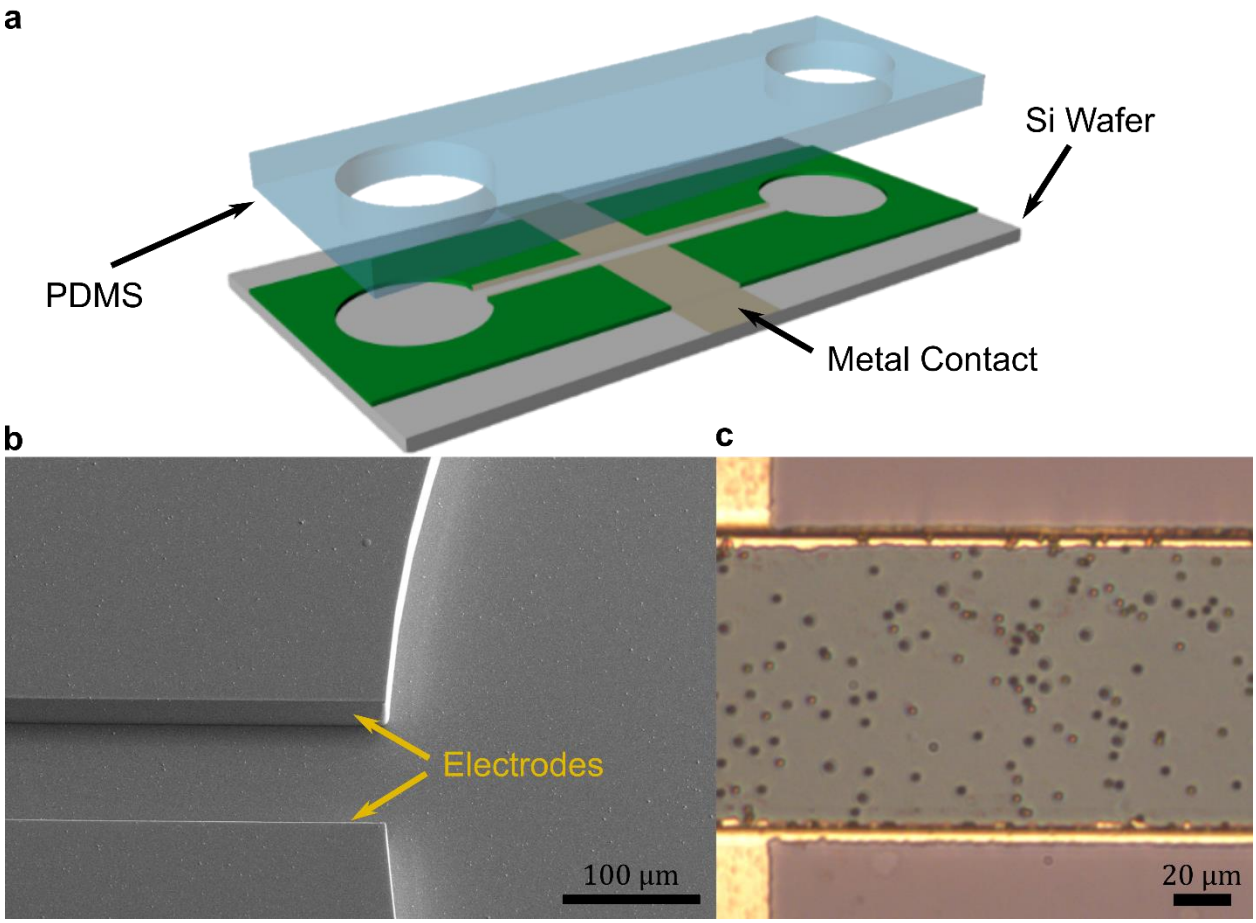

Figure 6.2. *a) Schematic of the whole microchannel device. b) SEM image of one of the fluid port junctions and c) optical image of a channel with 2 µm diameter particles suspended in 1 mM NaBr solution.*

Fig. 6.2 illustrates preliminary work on this fabrication process. Planar wall structures were successfully fabricated, with challenges depositing well-defined Au surfaces without significant delamination. In particular, it is important to maintain a contiguous connection between the vertical walls and surface metal contact points to apply the electric field properly. Proper alignment and mask width are also key to prevent breakage between the metal corners. Nonetheless, the system currently demonstrates potential towards future studies colloidal particle

behaviors. Following development of this system, a next step modification is insertion of dielectric or conducting cylinders at various positions between the two electrodes. For a dielectric cylinder near an electrode, EHD and AREF-induced electroosmosis may be observed with appropriately sized tracer particles. For a conducting cylinder, one would expect ICEK flows; however, to date there is no experimental work assessing AREF contributions to classical ICEK predictions. This device would provide direct experimental comparisons for such studies.

6.4 Sub-millimeter scale device for granular materials

Lab-on-a-chip devices typically operate at the sub-millimeter scale, while current developments reported in Chapter 4 present results on the millimeter scale. Bridging the length scale gap would be necessary to integrate vibrofluidics to current devices. A preliminary test would be to construct a simple channel by hand using two metal sheets, cut with a tapered entry port. These would be secured between two glass slides, then either clamped tight and/or epoxy sealed. Such a device can then be fastened onto the moving platform and observed visually using an appropriate optical setup.

A more robust fabrication process, with sophisticated geometries such as Y-channels, T-junctions, and serpentine channels could be acquired via glass or silicon wafer etching. Such equipment is readily available in a cleanroom fabrication facility and often used for glass-based microchannel designs in current fabrication techniques. A high-speed camera will be necessary to track the particulate motion, at least an order of magnitude larger in framerate than to the applied frequency. Standard image analysis can then be applied for temporal studies on the particle pumping speed.

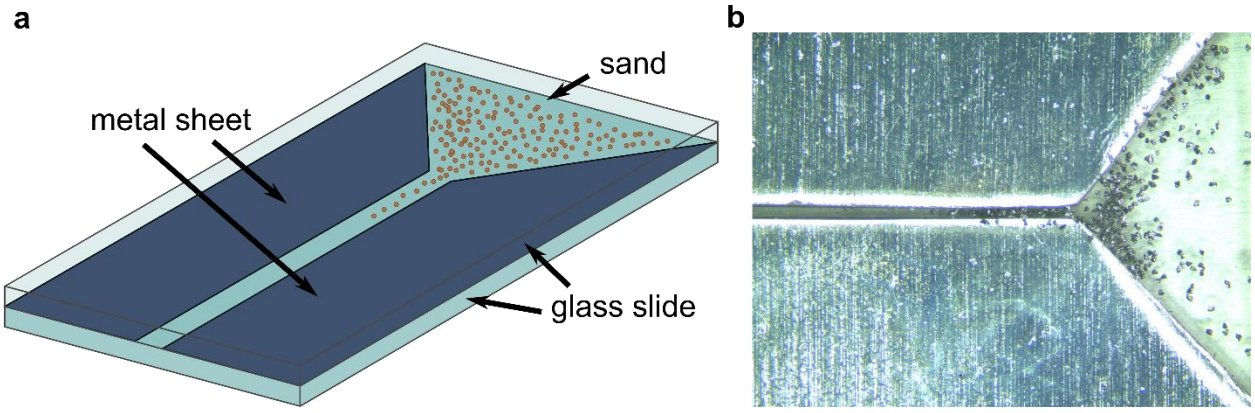

Figure 6.3. *a) Schematic of a dry powder pumping setup formed by two tapered metal sheets. b) Preliminary experiment pumping 70 grit black silicon carbide powder between two stainless steel sheets.*

6.5 Final comments

In unimodal electric field studies, AREF may play a significant role in other fields such as dielectrophoresis and ICEK, where there are several unresolved questions on velocity scaling, frequency dependency, and electrolyte dependency. Coupled oscillatory electric fields studies, such as with thermal gradients, solute concentration gradients, and magnetic fields, may also benefit from considering AREF contributions.

Current development on multimodal dynamics shows extreme promise in directed transport in a variety of systems, including the electrokinetic and dry-friction systems studied in this dissertation. Studies thus far focus on a dual-mode sinusoidal waveform; however, there is further potential in studying unique waveforms such as sawtooth, pulse, and other nonantiperiodic waveforms. On the micro to millimeter scale, these concepts may provide new means of separation and processing small scale reagents, particularly in point of care devices, pharmaceutical products, micromixers.

Appendix

Appendix A

The contents of this appendix section include supplementary derivations for the first order and second order electric field referenced in Chapter 2.

A1. First order approximation

The approximations used here are derived starting from the expressions derived by Hashemi et al. in their first order solution for arbitrary binary electrolyte diffusivities. Restricting to only univalent electrolytes (i.e. $z_+ = z_-$ = 1) and rewritten in context of the main script, the expression for the linear field and accompanying terms are

$$\tilde{E}(z) = \frac{\phi_0}{L}\left[A^* \frac{\cosh(\Omega^* \kappa z)}{\cosh(\Omega^* \kappa L)} + B^* \frac{\cosh(\gamma^* \kappa z)}{\cosh(\gamma^* \kappa L)} - C^*\right],$$

$$A^* = \frac{(s-1)^2}{2\Omega^{*2}\Gamma}, \qquad B^* = \frac{(s+1)^2}{2\gamma^{*2}\Gamma},$$

$$C^* = -1 + \frac{A^* \tanh(\Omega^* \kappa L)}{\Omega^* \kappa L} + \frac{B^* \tanh(\gamma^* \kappa L)}{\gamma^* \kappa L},$$

$$\Gamma = s^2 + 1 - \frac{1}{2\kappa L}\left[\frac{(s-1)^2(\Omega^* \kappa L - \tanh(\Omega^* \kappa L))}{\Omega^{*3}} + \frac{(s+1)^2(\gamma^* \kappa L - \tanh(\gamma^* \kappa L))}{\gamma^{*3}}\right],$$

$$\Delta = 1 - 4\beta^2 \nu^2, \qquad s = 2i\beta\nu + \sqrt{\Delta},$$

$$\Omega^* = \frac{1}{\sqrt{2}}\left(1 + 2i\nu - \sqrt{\Delta}\right)^{\frac{1}{2}}, \qquad \gamma^* = \frac{1}{\sqrt{2}}\left(1 + 2i\nu + \sqrt{\Delta}\right)^{\frac{1}{2}},$$

$$\nu = \frac{\omega}{\kappa^2 D}, \qquad \beta = \frac{D_+ - D_-}{D_+ + D_-}, \qquad D = \frac{2D_+ D_-}{D_+ + D_-}.$$

Consider the limit for when $\nu^2 \ll 1$ and when $\kappa L \gg 1$. Since β is bounded from $[-1, 1]$, then

$$\Delta \sim 1, \qquad s \sim 1 + 2i\beta\nu^2,$$

which simplifies Ω^* and γ^* to Ω and γ as written in the main text. For small ν, the expression for γ can be approximated as

$$\gamma \sim 1 + \frac{i\nu}{2} + O(\nu^2).$$

Finally at the low frequencies used in these experiments, we require $\nu^2\kappa L < 1$ such that $\tanh(\Omega\kappa L) \sim 1$. The same applies for $\tanh(\gamma\kappa L) \sim 1$ as well. Put together, Γ reduces to

$$\Gamma \sim 2 + 4\beta\Omega^2 - \frac{1}{2\kappa L}\left[\frac{(2\beta\Omega^2)^2(\Omega\kappa L - 1)}{\Omega^3} + \frac{4(1+\beta\Omega)^2(\gamma\kappa L - 1)}{\gamma^3}\right],$$

$$\sim \frac{2}{\kappa L} + 2\Omega^2(1-\beta^2),$$

in the limit of $O(\Omega^4)$ for the real part of Γ and $O\left(\frac{\Omega^2}{\kappa L}\right)$ for the imaginary part.

Expressions for A^*, B^*, and C^* in the same limit thus reduce to

$$A^* = \frac{\beta^2\Omega^2\kappa L}{\Omega^2\kappa L(1-\beta^2)+1}, \qquad B^* = \frac{\kappa L(1+2\beta\Omega^2)}{\gamma^2(\Omega^2\kappa L(1-\beta^2)+1)}, \qquad C^* = -1 + \frac{A^*}{\Omega\kappa L} + \frac{B^*}{\gamma\kappa L}.$$

The electric field is now

$$\tilde{E}(z) = \frac{\phi_0}{L}\left[A^*\frac{\cosh(\Omega\kappa z)}{\cosh(\Omega\kappa L)} + B^*\frac{\cosh(\gamma\kappa z)}{\cosh(\gamma\kappa L)} + 1 - \frac{A^*}{\Omega\kappa L} - \frac{B^*}{\gamma\kappa L}\right],$$

Which rearranges to Eq. (2.2) reproduced from the main text as

$$\tilde{E}(z) = \frac{\phi_0}{L}\left[1 + A\left(\Omega\kappa L e^{-\Omega\kappa(z+L)} - 1\right) + B\left(\gamma\kappa L e^{-\gamma\kappa(z+L)} - 1\right)\right],$$

where the expressions A and B used in the text are

$$A = \frac{A^*}{\Omega\kappa L}, \qquad B = \frac{B^*}{\gamma\kappa L}.$$

We now seek expressions for the electric field near the electrode and the field strength at the point particle height. First, for $z = -L$,

$$\tilde{E}_L = \frac{\phi_0}{L}\left[1 + \frac{\beta^2\Omega}{\Omega^2\kappa L(1-\beta^2)+1}(\Omega\kappa L - 1) + \frac{1+2\beta\Omega^2}{\Omega^2\kappa L(1-\beta^2)+1}(\gamma\kappa L - 1)\right].$$

Seeking terms in the bracket section to $O(\kappa L)$ reduces the expression to

$$\tilde{E}_L \sim \frac{\phi_0}{L}\left[\frac{\kappa L}{\Omega^2\kappa L(1-\beta^2)+1}\right],$$

by again noting that $\gamma \sim 1 + \frac{\Omega^2}{2}$ and neglecting terms in the numerator $O(\Omega^2)$ and smaller.

In the case of the particle center, the expression becomes more complex. Here we require $h \sim a$, such that $h \ll L$. Bounding z to the lower half domain $[0, -L]$ fixes the spatial position of the particle to $z = h - L$, such that

$$\tilde{E}_h = \frac{\phi_0}{L}\left[1 + \frac{\beta^2\Omega(\Omega\kappa L e^{-\Omega\kappa h} - 1)}{\Omega^2\kappa L(1-\beta^2)+1} + \frac{(1+2\beta\Omega^2)(\gamma\kappa L - 1)}{\gamma^3(\Omega^2\kappa L(1-\beta^2)+1)}\right].$$

Note that the hyperbolic functions are replaced by their exponential counterparts in the limit mentioned above. Furthermore,

$$\tilde{E}_h = \frac{\phi_0}{L}\left[\frac{\Omega^2\kappa L(1-\beta^2) + \beta^2\Omega(\Omega\kappa L e^{-\Omega\kappa h}) + (1+2\beta\Omega^2)(\gamma\kappa L)}{\Omega^2\kappa L(1-\beta^2)+1}\right].$$

Collecting terms in the numerator roughly $O(\kappa L)$ yield the expression

$$\tilde{E}_h \sim \frac{\phi_0}{L}\left[\frac{\Omega^2\kappa L(1-\beta^2)+\beta^2\Omega^2\kappa L e^{-\Omega\kappa h}}{\Omega^2\kappa L(1-\beta^2)+1}\right].$$

For particles that about 1 micron in radii, the exponential term becomes negligible. Thus in the bulk limit, the largely in-phase electric field can be more accurately described as

$$\tilde{E}_h \sim \frac{\phi_0}{L}\left[\frac{\Omega^2\kappa L(1-\beta^2)}{\Omega^2\kappa L(1-\beta^2)+1}\right].$$

A2. Second order approximation for AREF

The following approximation for AREF is based upon the analytic, low potential and small double layer limit derivation provided by Balu and Khair. Noting that the complex conjugate of Ω is $-\Omega i$ and written in the context of the main text, the expression is

$$\bar{E} = \frac{\phi_0^2}{\kappa^2 L^3 \phi_T}\begin{bmatrix} \beta\lambda\lambda^* m^* \sinh\left(\frac{mz}{L}\right)\cosh\left(\frac{m^* z}{L}\right) + \lambda\eta^* \sinh\left(\frac{mz}{L}\right) \\ +\beta\lambda\lambda^* m \sinh\left(\frac{m^* z}{L}\right)\cosh\left(\frac{mz}{L}\right) + \lambda^*\eta \sinh\left(\frac{m^* z}{L}\right)\end{bmatrix},$$

$$\lambda = \frac{\beta\Omega\kappa L}{2\cosh(\Omega\kappa L)}, \qquad \lambda^* = \frac{-\beta\Omega\kappa L\mathrm{i}}{2\cosh(\Omega\kappa L\mathrm{i})},$$

$$\eta = \frac{(\Omega\kappa L)^2(1-\beta^2)}{2}, \qquad \eta^* = -\eta,$$

$$m = \Omega\kappa L, \qquad m^* = -\mathrm{m}i.$$

Substituting asterisk conjugate terms and using trigonometric identities $\cos(x) = \cosh(ix)$ and $i\sin(x) = \sinh(ix)$, the expression expands to

$$\bar{E} = \frac{\kappa\phi_0^2}{\phi_T}\begin{bmatrix} \frac{\Omega^3(\beta^3-\beta)}{4}\left[\frac{\sin(\Omega\kappa z)}{\cos(\Omega\kappa L)} + \frac{\sinh(\Omega\kappa z)}{\cosh(\Omega\kappa L)}\right] \\ -\frac{(\beta\Omega)^3}{4}\left[\frac{\cosh(\Omega\kappa z)\sin(\Omega\kappa z)}{\cosh(\Omega\kappa L)\cos(\Omega\kappa L)} + \frac{\cos(\Omega\kappa z)\sinh(\Omega\kappa z)}{\cos(\Omega\kappa L)\cosh(\Omega\kappa L)}\right]\end{bmatrix}.$$

Limiting z to the lower domain of $[0, -L]$ and noting that $\Omega\kappa L \gg 1$ yields the exponential approximations of

$$\frac{\sin(\Omega\kappa z)}{\cos(\Omega\kappa L)} \sim -ie^{i\Omega\kappa(z+L)}, \qquad \frac{\sinh(\Omega\kappa z)}{\cosh(\Omega\kappa L)} \sim -e^{-\Omega\kappa(\mathrm{z}+\mathrm{L})},$$

$$\frac{\cosh(\Omega\kappa z)}{\cosh(\Omega\kappa L)} \sim e^{-\Omega\kappa(z+L)}, \qquad \frac{\cos(\Omega\kappa z)}{\cos(\Omega\kappa L)} \sim e^{i\Omega\kappa(z+L)}.$$

Substituting and simplifying yields

$$\bar{E} = \frac{\kappa\phi_0^2}{\phi_T}\left[\begin{array}{c}\frac{\Omega^3(\beta-\beta^3)}{4}\left[ie^{i\Omega\kappa(z+L)} + e^{-\Omega\kappa(z+L)}\right] \\ +\frac{(\beta\Omega)^3}{4}\left[ie^{i\Omega\kappa(z+L)}e^{-\Omega\kappa(z+L)} + e^{-\Omega\kappa(z+L)}e^{i\Omega\kappa(z+L)}\right]\end{array}\right],$$

Rewriting the complex Ω by its real and imaginary components such that

$$\Omega = \Omega'(1+i), \;\; \Omega' = \sqrt{\frac{\omega}{2\kappa^2 D}},$$

removes complex terms to

$$\bar{E} = \frac{\kappa{\Omega'}^3\phi_0^2}{\phi_T}\left[\frac{(\beta-\beta^3)\left[\sin\left(\Omega'\kappa(z+L)\right) - \cos\left(\Omega'\kappa(z+L)\right)\right]}{e^{\Omega'\kappa(z+L)}} - \frac{\beta^3}{e^{2\Omega'\kappa(z+L)}}\right].$$

For a particle at a distance h away from the electrode such that $z = h - L$, yields

$$\bar{E} = \frac{\kappa{\Omega'}^3\phi_0^2}{\phi_T}\left[\frac{(\beta-\beta^3)(\sin(\Omega'\kappa h) - \cos(\Omega'\kappa h))}{e^{\Omega'\kappa h}} - \frac{\beta^3}{e^{2\Omega'\kappa h}}\right].$$

Here we see that AREF scales as odd powers of β, with the complex shape due to the sine and cosine terms. Additionally, AREF scales as ϕ_0^2 and $\sim\omega^{\frac{3}{2}}$, which matches scaling predictions provided by Hashemi et al. in the low potential limit.

Appendix B

The contents of this appendix section include information to be submitted to the *Lab-on-a-chip* journal supplemental material.

B1. Numerical methods at low-moderate Fr range

When Fr is small or $\hat{v}_{osc}$ is not negligible, we solve Eq. (5.4) as a shooting method boundary value problem over one period T of the motion: the initial value $\hat{v}(0)$ is adjusted with Newton's method until the boundary condition $\hat{v}(0) = \hat{v}(T)$ is satisfied. If Newton's method fails to converge bisection is used as a fallback. The velocity $\hat{v}(T)$ is calculated from $\hat{v}(0)$ by numerical integration of Eq. (4) over the period. The $\hat{v}$ trajectory either traces $\hat{x}''$ until $|\hat{x}''(\hat{t})| \leq \mathrm{Fr}^{-1}$, or it follows a linear path with slope $\pm\mu_k/(\mu_s \mathrm{Fr})$ until the condition $\hat{v}(\hat{t}) = \hat{x}'(\hat{t})$ is satisfied. The trajectory is thus determined by finding the special points where $|\hat{x}''(\hat{t})| \leq \mathrm{Fr}^{-1}$ or where a line intersects the $\hat{x}(\hat{t})$ curve. The special points are determined by first bracketing then refinement. The velocity $\hat{v}_{st}$ is computed as the mean of the converged trajectory over the period. In the large-Fr, negligible $\hat{v}_{osc}$ limit we use Newton's method, with bisection as a fallback, to find the zero of $f(\hat{v}_{st}) = \int_0^T \mathrm{sign}[\hat{x}'(\hat{t}) - \hat{v}_{st}]d\hat{t}$. For each iteration, the intersections of the horizontal line $\hat{v}_{st}$ with curve $\hat{x}'(\hat{t})$ are determined by bracketing and refinement. These points of intersection partition the period into positive and negative values of the sign function, which are readily summed to compute f.

Table S1. *Properties of the granular media. Individual particle sizes were estimated from optical microscopy as the mean and standard deviation of 10 particles, except for the manufacturer-provided mean size of the boron carbide. The particle-particle static friction coefficient was measured via the angle of repose method, and is reported as the mean and standard deviation of 6 trials. The particle-substrate static friction coefficient was measured via the sliding tilt angle method, and is reported as the mean and standard deviation of 5 trials.*

	Particle Size (μm)	**Static Friction Coefficient, Particle-Particle**	**Static Friction Coefficient, Particle-Substrate**
Glass Sand (Yellow)	86 ± 30	0.84 ± 0.05	1.8 ± 0.4
Glass Sand (Blue)	88 ± 26	0.83 ± 0.06	2.1 ± 0.3
Boron Carbide	60 ± 18	0.82 ± 0.09	2.0 ± 0.5
Yeast	370 ± 140	0.79 ± 0.04	0.55 ± 0.06
Ibuprofen	66 ± 33	1.31 ± 0.14	2.3 ± 0.8

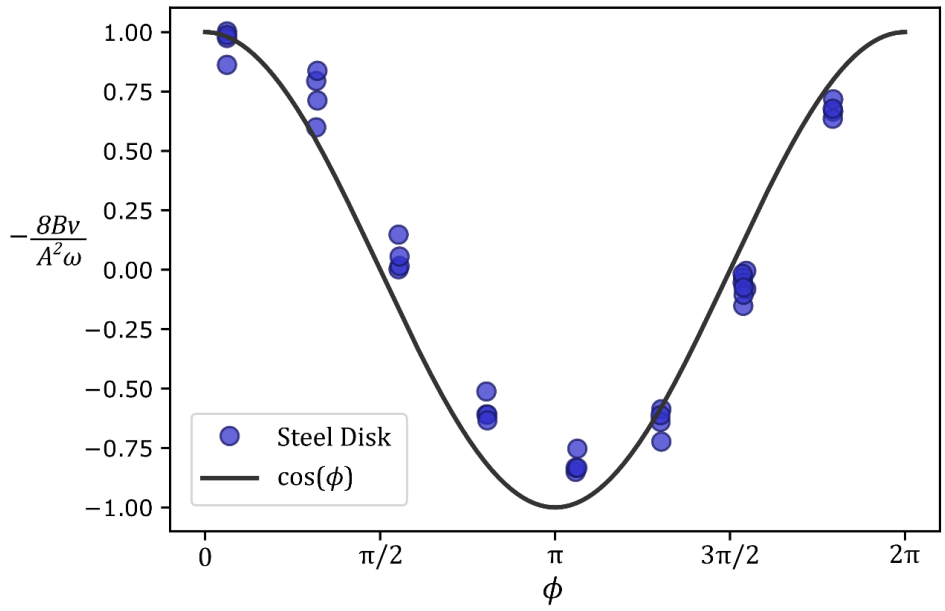

Figure S1. *Velocity versus imposed phase lag. The dimensionless velocity of steel disks moving on a vibrating aluminum surface, normalized on the predicted velocity magnitude (cf. Eq. 3 in the main manuscript for* $|B/A| > \frac{1}{4}$*), versus the imposed phase lag* ϕ*. Markers are individual experimental trials, and the black line is the theoretical prediction* $\cos\phi$*. The vibratory waveform is 30 and 60 Hz, with average vibratory amplitudes of* $A = 0.31$ *mm,* $B = 0.14$ *mm, and average Friction number* $Fr = 4.7$*.*

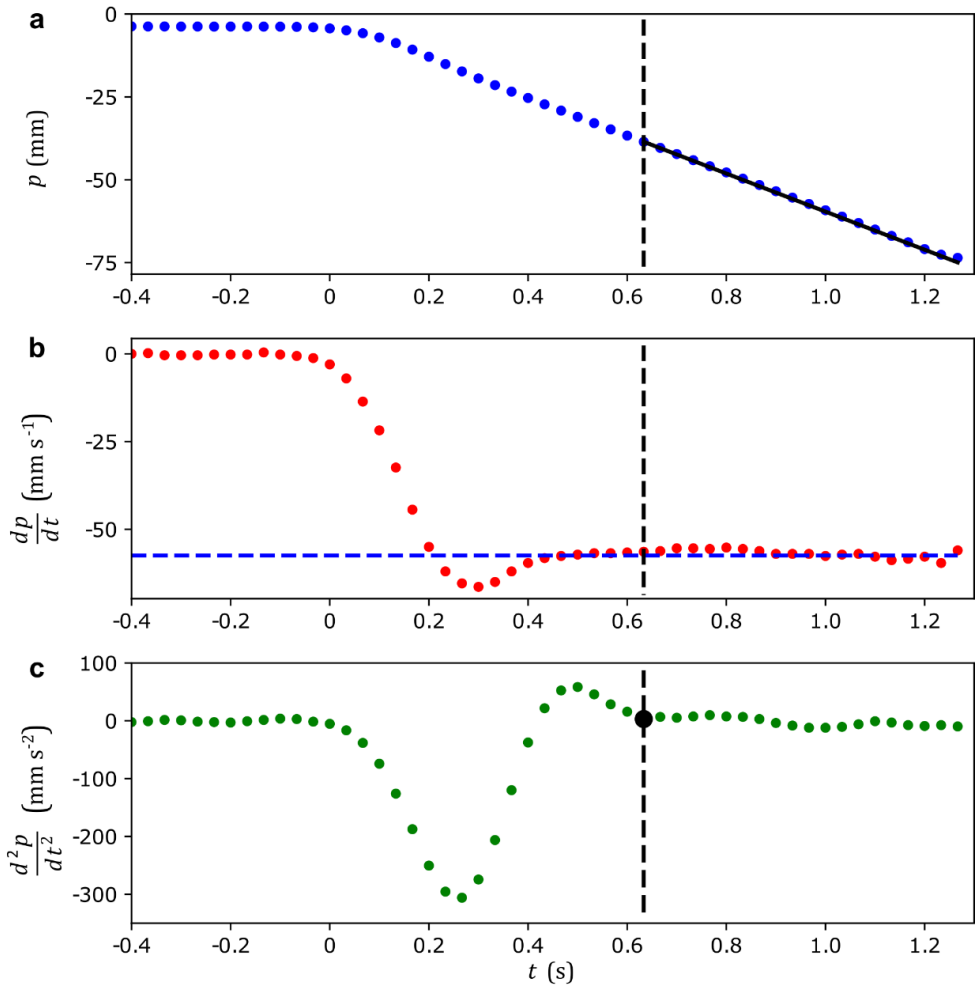

Figure S2. *Representative tracking of a granular front. The position (a), velocity (b), and acceleration (c) of the leading front of blue-colored glass sand moving in a straight channel (cf. Fig. 2a). The vibratory waveform is 30 and 60 Hz applied at* $t = 0$*, then ramped up to maximum applied amplitude at* $t = 0.25$ *s. The maximum vibratory amplitude was* $A = 0.83$ *mm,* $B = 0.32$ *mm. The vertical dashed line denotes the time at which the acceleration (c) returned to zero and denotes the beginning of the range over which linear regression was used to determine the steady velocity, shown as a solid black line in (a) and horizontal blue dashed line in (b).*